University of Bergen

A study of Silicon 3D sensors

Master Thesis in Experimental Particle Physics

by

Kristine Indahl Helle

Department of Physics and Technology

1st of June 2010

Acknowledgements

First of all I would like to thank my supervisors Bjarne Stugu and Heidi Sandaker:

Bjarne for guiding me through my whole master degree and all the aspects of my thesis. He has guided me through the analysis and always given answers to my questions. And has especially been a very strong support in the final stage before deadline.

Heidi for introducing me to the subject and including me in the environment and answering my questions along the way.

Secondly, I would like to thank Ole Røhne and Håvard Gjersdal for supplying me with data and the foundation of my code, to teach me how to assemble the setup at the lab and how to perform tests and calibrations of the sensors. They were a good support for me at the test beam in 2009, and they have also always been available for answering any questions I might have about analysis or the lab setup.

I would also like to thank Dominik Fehlker for helping me at the lab, for Guiding me through the instructions of the setup, always trying to help me when needed and arranging it so I got a space in the laboratory, with an environmental chamber, that the Space Physic's group was kind enough to lend me.

I would like to thank Michael Pennington for proof reading most of the thesis and helping me with the language.

There are several people in the particle physic's group I would like to thank: Thomas Burgess for helping me out whenever I'm stuck with an ”unsolvable” computer problem, for many good advises and guidance through my analysis. The PHD students Peter Rosendahl, Therese Sjursen and Arshak Tonyan for helping me resolving all kinds of obstacles along the way.

Jeg vil takke alle jeg deler kontor med for å svare på allslags små spørsmål,

gi meg mange gode tips, trøst og støtte under innspurten.Spesielt må jeg få takke Alette Aasvold som jeg har melket for tips innenfor Latex.

Så vil jeg takke Camilla Stokkevåg og Anja Heggen for all hjelp, oppmuntring og rådgivning jeg har fått under oppgaveskrivningen og for vennskapet vi har hatt de siste tre årene.

Jeg vil takke hele familien og slekten min som alltid stiller opp for meg for å gjøre det lettere å kombinere småbarns- familieliv med en master og som alltid har en overdrevet stor tro på meg.

Til slutt vil jeg takke mine tre elskede gutter Daniel, Loke Sebastian og Trym Jakob som har måttet tåle meg som temmelig åndsfraværende det siste halvåret uten å klage for mye og som gir meg all den kjærligheten og støtten jeg trenger.

Kristine Indahl Helle
May 31, 2010

Contents

Acknowledgement **i**

Abstract **1**

1 Introduction **3**

2 Detection of ionizing radiation **5**

2.1 Charged particle interaction with matter 5
2.1.1 Energy loss mechanisms of charged particles 5
2.1.2 Energy loss by heavy charged particles 6
2.1.3 Energy straggling -The energy loss distribution 7
2.2 Ionization detectors 9
2.2.1 Gaseous ionization detector 11
2.3 Semiconductors 11
2.3.1 Some properties of semiconductors 11
2.3.2 Energy Band model 11
2.3.3 Majority and minority carriers 13
2.3.4 Recombination and trapping 13
2.3.5 Doping 14
2.3.6 P-n junctions: 15
2.3.7 Application of voltage to a p-n junction 16
2.3.8 Junction capacitance 18
2.3.9 Energy deposition in a semiconductor 19
2.3.10 Damages done by radiation to a crystal 19
2.3.11 Effects of temperature 19
2.3.12 Detector efficiency 20
2.3.13 Leakage current 20
2.4 Planar semiconductor detectors 21
2.5 The 3D silicon sensor with active edge 23
2.5.1 Electrode configuration layouts 25
2.5.2 Readout of the 3D sensor 25
2.5.3 Time over Threshold 27

3 The Large Hadron Collider and The ATLAS experiment 29
3.1 The Large Hadron Collider 29
3.1.1 Cross section and luminosity 31
3.1.2 The LHC experiments 31
3.2 The (A Toroidal Lhc ApparatuS) ATLAS detector 32
3.2.1 Physics studied in the ATLAS detector 32
3.2.2 Layout off the Atlas detector 33
3.3 ATLAS upgrade activities 35
3.3.1 The plans for upgrading LHC 35
3.3.2 The scheduled ATLAS upgrade activities 35

4 Test beam activities 37
4.1 Testbeam 2008 37
4.1.1 The devices under test 37
4.1.2 Data collecting 37
4.1.3 Track reconstruction and alignment 39

5 Analysis 41
5.1 Parameters used in the analysis 41
5.2 Alignment studies 43
5.3 Time over Threshold 47
5.3.1 Time over threshold results 49
5.4 Efficiency 55
5.5 Study of the ”active edge” 58
5.5.1 Box-convolution of the efficiency in the edge pixel . . 59
5.6 Study of the loss of detection efficiency in volume occupied by the electrode cylinders 63
5.7 Efficiency and ToT as function of bias voltage 64
5.7.1 Analysis of the 4E-C sensor 66
5.8 Summary of the analysis 72

6 Test and calibrations of Silicon 3D detectors in Bergen 75
6.1 Motivation for a test set up in Bergen 75
6.2 Setup and equipment 77
6.2.1 Front End electronic card (FEI3) 77
6.2.2 The TPCC board 78
6.2.3 The Turbo pixel low level card (TPLL board) and the VME system 78
6.2.4 The environment chamber 80
6.3 Measurements and scans of the Si-106 sensor 82
6.4 Summary of the laboratory tests 92

7 Conclusion and outlook 95

Bibliography 98

Abstract

The 3D Silicon Detector is a semiconductor tracking detector, that unlike the conventional planar semiconductor tracking detectors, have the electrodes penetrating the wafer in cylinders. The shorter electrode distances gives advantages such as faster collection time, lower bias voltage and more radiation tolerance. The 3D detectors are also equipped with an active edge electrode that makes the sensor sensitive all the way to the edge and thus leaving less dead area of the sensor. The 3D detector is considered as a candidate for upgrading the inner tracking detector of the ATLAS detector when the LHC is upgraded to higher luminosity. Investigation of the 3D detector's properties is ongoing at laboratories and at test beams to evaluate its prospects in the ATLAS detector and other applications such as medical imaging.

For this thesis analyses were done from test beam data taken at CERN in June 2008. The analysis showed that the sensor is fully operable at 10V and had fully efficiency in the sensors edge pixel.

A test and calibration system for 3D sensors was set up at the laboratory and taken into use. Threshold and noise scans were performed to a contaminated 3D sensor, the SI-106 sensor. These showed that the sensor was fully depleted at 10V.

Chapter 1

Introduction

Silicon detectors are a type of semiconductor detector used to detect and reconstruct tracks of ionizing particles. These were first made and used by Pieter Jacobus Van Heerden, a graduate student in the occupied Netherlands during World War II, and have been in use for over 50 years [1]. The semiconductor detectors are very popular due to a high time-, energy- and position resolution. These sensors are however sensitive to radiation damage and will have decreased performance after a certain dose.

Planar silicon detectors are used in the inner layers of the (A Toroidal Lhc ApparatuS) ATLAS detector at The European Organization for Nuclear Research (CERN), where they reconstruct tracks of short lived particles with high precision. Their location in the detector exposes them to very strong radiation, so they start to deteriorate after only 3 years of design luminosity.

In a planned upgrade of the Large Hadron Collider (LHC), one expects that the radiation exposure to the planar sensors will be so great that it is necessary to look for a better replacement in an ATLAS upgrade. Several groups are working with development and testing of new sensor candidates. Among the candidates are new and improved versions of the planar silicon detector, the Chemical Vapor Deposition (CVD)-diamond detector and the 3D-Silicon sensor.

The 3D silicon sensor is a new type of semiconductor detector made possible by recent developments in sensor fabrication. These sensors have several advantages over the traditional planar semiconductor detectors; such as faster collection time, lower bias voltage, less dead material and excellent radiation hardness. Among these properties the radiation hardness is a key factor for the ATLAS upgrade. There are also other applications for the sensors such as in medical imaging devices.

At present, continuous testing and evaluation of the 3D sensors are taking place to decide if they will be used by the ATLAS detector. This is done during test beam activities and at laboratories spread among several universities and institutions.

In this thesis, I analyze data taken at test beam 2008. The analyses include an alignment study, an efficiency study of the detector and its edge. Also the efficiency and signal have been studied as a function of bias voltage for a sensor with three electrodes in each pixel and one with four electrodes in each pixel.

Another part of this thesis work was to use a laboratory setup. This setups main purpose is to perform quality assurance tests of 3D sensors, but it is also the first step in a setup that aims to explore the possibilities of other applications for the 3D sensors.

In the background, **Chapter 2**, the basics of ionizing radiation detection physics and terminology important in this work are presented. Initially interactions of charged particles will be described. Further the principles and properties of semiconductor detectors are presented, including the conventional silicon planar sensor and the new silicon 3D sensor.

In **Chapter 3**, a brief introduction to the LHC and the ATLAS detector will be given, as well as the plans for upgrading the LHC and ATLAS detector, in which the 3D sensor plays an important role as candidate for the inner B-layer.

Chapter 4 describes the test beam 2008, from which the data for the analysis is taken. This includes a description of equipment, setup and the details of the sensors that are being tested. The principles of data taking and reconstruction are also included.

Chapter 5 contains an analysis of the data from the test beam described in the previous chapter. This includes an alignment study, a study of signal and efficiency as a function of bias voltage, a study of the edge- efficiency and resolution, and comparing two sensor designs.

In **Chapter 6**, a setup for quality assurance of the 3D sensors is assembled, and tests performed on a 3D sensor. Conclusion and Outlook is summed up in **Chapter 7**.

Chapter 2

Detection of ionizing radiation

2.1 Charged particle interaction with matter

The ionization processes occurring when radiation passes through matter is the basis for all particle detection, and thus knowledge of these effects is very important for understanding detectors.In the following section an introduction to some of the relevant concepts for the Semiconductor Sensors will be given.

2.1.1 Energy loss mechanisms of charged particles

Reactions between charged particles and matter can occur through several channels, depending on the radiation type, the energy of the particle and the material that the particle traverses. The reactions can take place with the atoms as a whole or with the constituents of the atoms. The most common type of interaction for charged particles are electromagnetic.

When a heavy charged particle i.e. much heavier than an electron (for example a charged pion) passes through matter, it experiences two main features, energy loss and deflection from its incident path. This is primarily due to the two processes:

1)inelastic collisions with the electrons of the material.
2)elastic scattering from nuclei

In addition other processes occur with smaller probability:

3)emission of Cerenkov radiation (effect occurring when a heavy charged particle pass through a material with a velocity greater than the speed of

light in that material)
4)nuclear reactions
5)bremsstrahlung (important for electrons and positrons)

2.1.2 Energy loss by heavy charged particles

For the heavy particles the energy loss is mainly due to the inelastic collisions with the materials' atomic electrons. In these collisions, energy is transferred to the atom and causes excitations, when the electron is lifted to a higher discrete energy level, or ionization, where the electron is ejected from the atom. The amount of energy transferred in each collision is only a small fraction of the particles initial kinetic energy, but for solids the number of collisions is very large and this causes the charged particle to loose a measurable amount of energy within a very thin absorber.

The large number of collisions per macroscopic path length gives relatively small fluctuations in the total energy loss. One can therefore work with the average energy loss per unit path length called the stopping power dE/dx. This has been calculated classically by Bohr and quantum mechanically by Bethe, Bloch and other authors:

$$-\frac{dE}{dx} = 2\pi N_a r_e^2 m_e c^2 \rho \frac{Z}{A}\frac{z^2}{\beta^2}\left[ln\frac{2m_e\gamma^2 v^2 W_{max}}{I^2} - 2\beta^2 - \delta - 2\frac{C}{N}\right] \tag{2.1}$$

with

Symbol	Definition
r_e	Classical electron radius = $2.818 fm$
m_e	Electron rest mass = $0.511 MeV/c^2$
N_a	Avogadro's number = $6.022 \times 10^{23}/mol$
I	Mean excitation energy (eV)
Z	Atomic number of absorber
A	Atomic weight of absorber (g/mol)
ρ	Density of absorber
z	Charge of incident particle in units of e
β	= v/c of incident particle
γ	$= 1/\sqrt{1-\beta^2}$
W_{max}	Maximum energy transfer in a single collision
δ	Density correction
C	Shell correction

The Bethe Bloch Formula (Eq: 2.1) expresses the average energy loss per unit path length in terms of the momentum transfer. It is proportional

to the number of electrons in the absorber and to the square of the particle charge [2]. Figure 2.1 show the energy loss as a function of $\beta\gamma = p/Mc$ for different materials. As can be seen from the curve, the stopping power increases strongly towards lower energies.

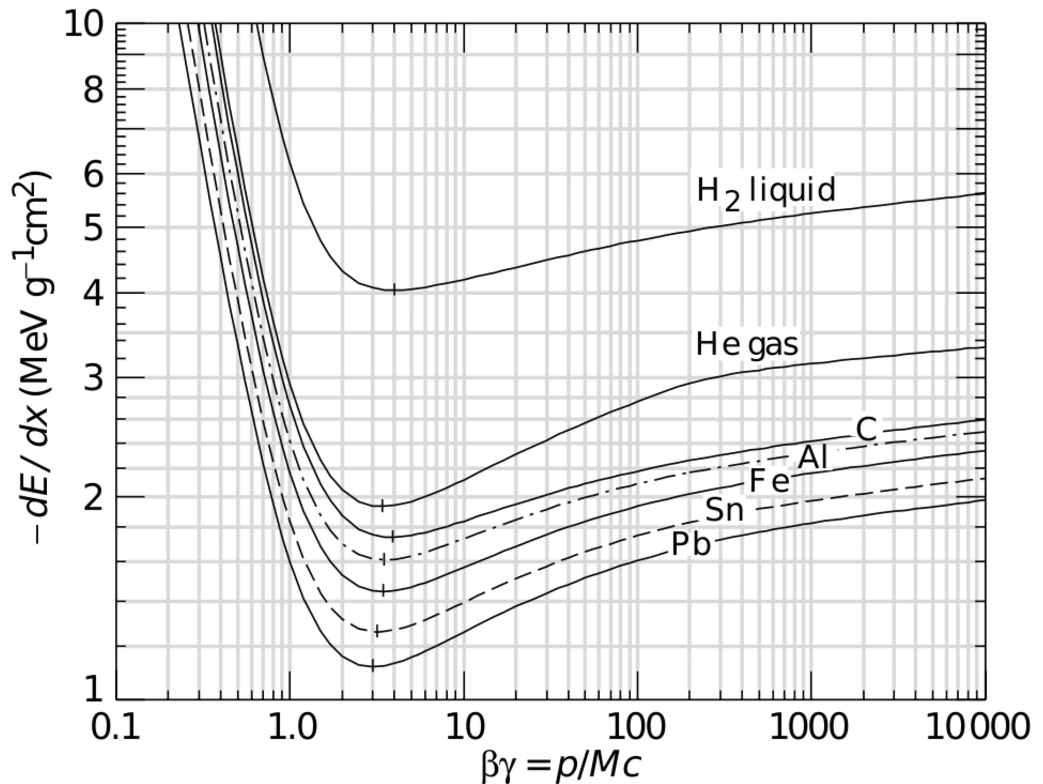

Figure 2.1: Energy loss ($=\langle -dE/dx \rangle$) as a function of $\beta\gamma = p/Mc$ for different materials [2].

2.1.3 Energy straggling -The energy loss distribution

A mono energetic beam that passes through a specific material of a certain thickness will have an energy loss distribution. The calculation of this distribution is a complex mathematical problem, and one normally distinguishes between thin absorbers and thick absorbers.

Energy loss distribution for thin absorbers

The calculation of the energy loss distributions for thin absorbers were made by Landau, Symon and Vavilov for different regions of applications. The distinguishing parameter for these theories is

$\kappa = \frac{\overline{\Delta}}{W_{max}}$,

which is the ratio between the mean energy loss $\overline{\Delta}$ and the maximum energy transfer permitted W_{max} in a single collision.

$\overline{\Delta}$ can be calculated by the Bethe Bloch formula (Eq: 2.1), however it is usually approximated by only considering the multiplicative term and ignoring the logarithmic term:

$$\overline{\Delta} \simeq \xi = 2\pi N_a r_e^2 m_e c^2 \rho \frac{Z}{A} \left(\frac{z}{\beta}\right)^2 x$$

Landau's theory applies for very thin absorbers, $\kappa \leq 0.01$ (Symon and Vavilov applies for intermediate κ). Landau makes three assumptions;

1) The maximum energy transfer permitted W_{max} is infinite, making κ approach zero.
2) Each individual energy transfer is sufficiently large to treat the electrons as free (ignoring energy transfers from so called distant collisions).
3) The decrease in velocity of the particle is negligible i.e., the particle maintains constant velocity.

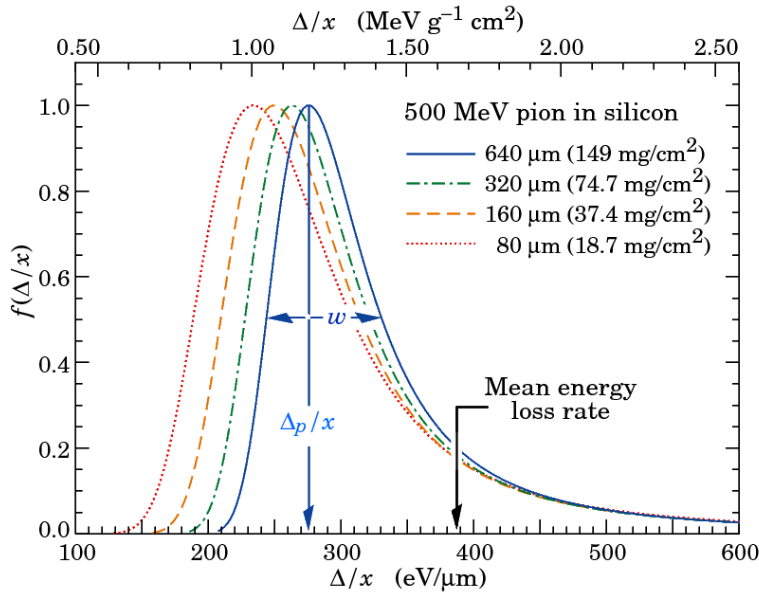

Figure 2.2: The Landau distributions (Straggling functions) in silicon for 500 MeV pions, normalized to unity at the most probable value. The w is the full width at half maximum [2].

The Landau distribution is expressed as:

$$f(x,\Delta) = \phi(\lambda)/\xi \tag{2.2}$$

with

$$\phi(\lambda) = \frac{1}{\pi}\int_0^\infty exp(-u\,\ln u - u\lambda)\,\sin\pi u\,du$$

and

$$\lambda = \frac{1}{\xi}\left[\Delta - \xi(\ln\,\xi - \ln\varepsilon + 1 - C)\right]$$

Where C = Euler's Constant = 0.577 and

$$\ln\varepsilon = \ln\frac{(1-\beta^2)I^2}{2mc^2\beta^2} + \beta^2.$$

The most probable value was found to be

$$\Delta_{mp} = \xi\left[\ln\left(\frac{\xi}{\varepsilon}\right) + 0.198 - \delta\right], \tag{2.3}$$

where δ is the density correction.This correction is important in liquids and solids and tends to reduce the energy loss at high energies. The full width at half maximum is given by $w = 4\xi$.

Energy loss distribution for thick absorbers

Relatively thick absorbers have κ approaching zero and an energy loss distribution approaching a Gaussian if the number of collisions is sufficiently large (Figure 2.3).

$$f(x,\Delta) \propto exp(\frac{-(\Delta-\overline{\Delta})^2}{2\sigma^2}) \tag{2.4}$$

Denoting x as absorber thickness, Δ as the energy loss in the absorber, $\overline{\Delta}$ as the mean energy loss(μ) and σ as the standard deviation of the distribution, then from Figure 2.3 one can see that the width of the distribution is determined by $\sigma = w/2.36$ [3] .

2.2 Ionization detectors

Ionization detectors can measure the ionization caused by a passing particle. The ionization detectors can be found in various forms, as gaseous ionization chambers and as solid detectors like the semiconductor detectors. Reference [4] gives a general introduction to ionization detectors.

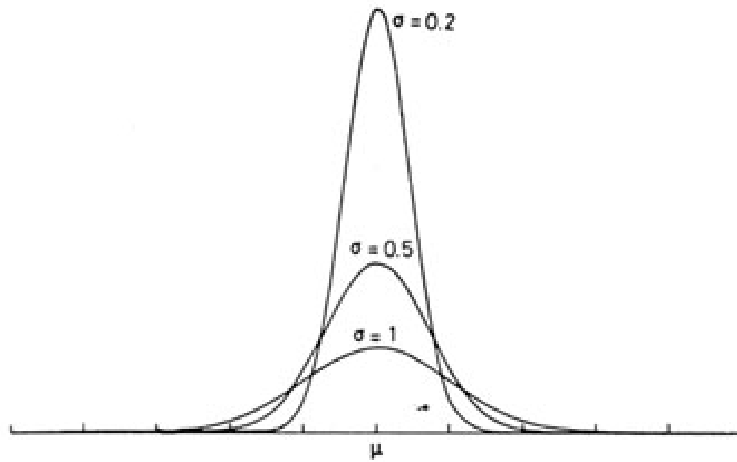

Figure 2.3: The Gaussian distribution for various σ. One can see that σ determines the width of the distribution [3]

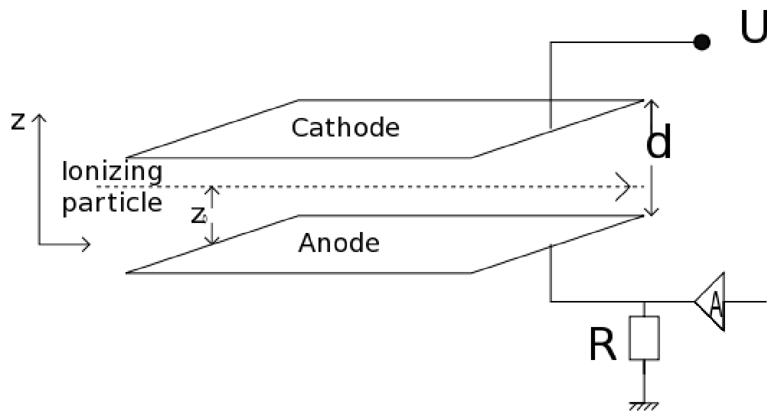

Figure 2.4: Gaseous ionization detector: A parallel plate capacitor is filled with counting gas (Argon, etc) and an electric field applied. Ionizing radiation creates an electron-ion pair that induces a charge on the capacitors plates when drifting in the electric field. This charge moves through a resistor and can be measured as a voltage pulse.

2.2.1 Gaseous ionization detector

The simplest form of an ionization gas detector is a parallel plate capacitor filled with, e.g., Argon as counting gas (Figure 2.4) . An electric field is applied so that one of the plates get a positive potential; the anode plate, while the other plate gets a negative potential, the cathode plate. As radiation passes through the capacitor, the gas is ionized in the trajectory of the incoming particle, i.e. an electron -ion pair is created. If the electric field that is applied is of the right strength, the pair will not recombine, but the electron will drift towards the anode and the ion towards the cathode. The moving charges will induce a charge on the capacitor electrodes. This charge moves through a resistor and is measured as a voltage pulse.

2.3 Semiconductors

Semiconductor detectors are particle track detectors with high position resolution. These are analogous to the gaseous ionization detectors, but with some very significant differences. Instead of a gas, the medium is a solid semiconductor crystal. The ionization products are electrons and holes instead of electrons and ions. These two factors gives them a great advantage: the semiconductor has an ionization potential of only 3.6 eV in Silicon and 2.9 eV in Germanium, compared to between 20 and 40 eV in gases. This reduction in in potential leads to an improved energy resolution because the number of ions produced in a semiconductor is 10 times larger than in gas. Another factor is that the higher density gives the semiconductors higher stopping power than the gas [5].

Some disadvantages of semiconductor detectors are that except for Silicon, the semiconductors must be cooled while operating. Semiconductors are also very sensitive to radiation damage, which will be discussed later in this chapter.

2.3.1 Some properties of semiconductors

In a so called pure or intrinsic semiconductor, the 4-valence atoms are arranged in a crystal lattice with covalent bindings between them as illustrated in Figure 2.5.

2.3.2 Energy Band model

The energy band model is used to describe the the behavior of electrons and holes to externally applied forces like light, heat, or voltage. The energy band structures of insulators, conductors and semiconductors are shown in Figure 2.6: The energy bands are several discrete energy levels very close to

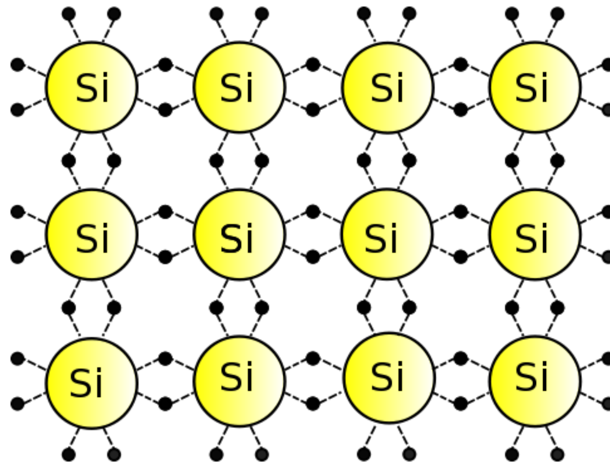

Figure 2.5: The silicon lattice structure. The silicon atoms forms a grid of covalent bindings, sharing all their outer electrons with the surrounding atoms

each other. The forbidden band is a region where there is no allowed energy levels. In the highest allowed band, called the conduction band, electrons can move freely around in the structures of the material, while in the lower allowed band, called the valence band, the electrons are attached to the atom.

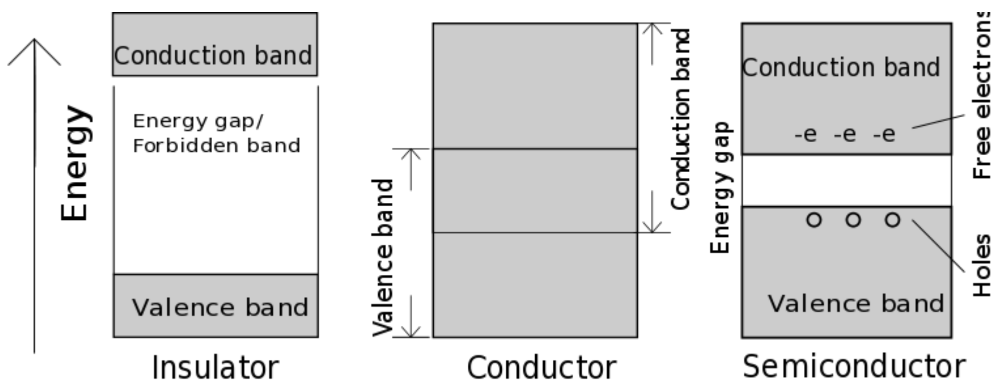

Figure 2.6: The energy band models for an insulator with a large forbidden gap, a conductor with overlapping allowed energy levels and a semiconductor with an intermediate band gap.

In an insulator, the forbidden gap is large and the electrons will stay in the valence band and thus attached to an atom even when an electric field is applied to it, and therefore no current is generated.

A conductor has overlap between the valence and conduction bands so that electrons can easily be elevated from the valence band in to the conduction band and thus have a current flowing when an electric field is applied .

In a semiconductor the band gap is of intermediate size. At 0 K all electrons will be in the valence band, but as the temperature increases to room temperature, more electrons have sufficient thermal energy to be elevated into the conduction band, and one can observe a small current when an electric field is applied. At room temperatures thermal energies can excite an electron into the conduction band and thus leave a hole in the lattice, a current flows through the crystal as a neighboring electron might jump in to fill the hole and thereby leaving a new hole that again can be filled by another neighbor electron and so on. In this way current is flows from the negative electrons moving in the conduction band and the positive holes flow in the valence band. Under the influence of an external electric field, the drift velocities of the electrons and holes might be expressed as a function of their mobility and the electric field.

For silicon the mobility is constant so that there is a linear relation between E and the drift velocity.

2.3.3 Majority and minority carriers

There are two types of charge carriers in a semiconductor. These are the electrons that carry a negative electric charge and the holes that carry a positive electric charge. The majority carriers are the more abundant carrier while the minority carrier is the less abundant. In an intrinsic semiconductor the numbers are equal for both carrier types.

2.3.4 Recombination and trapping

Recombination of the electrons and holes is a rather rare process. However, impurities in a crystal add energy levels to the forbidden band and form recombination centers where an electron from the conduction band can be captured and then either be released back into the conduction band, or be annihilated with a trapped hole. These centers reduces the time when the charge carriers remain free, which needs to be longer than the collection time. Trapping is another effect that arises from impurities. Here only one of the charge carrier types will be trapped and then released after a certain time, the duration of the trapping is closely related to the effect. If the trapping time exceeds the collection time, the charge will remain uncollected, while if the trapping time is much shorter than the collection time the effect will be negligible. From this it is evident that the crystal should not have too large concentration of impurities (more than (10^{10} impurities pr cm^3). Structural

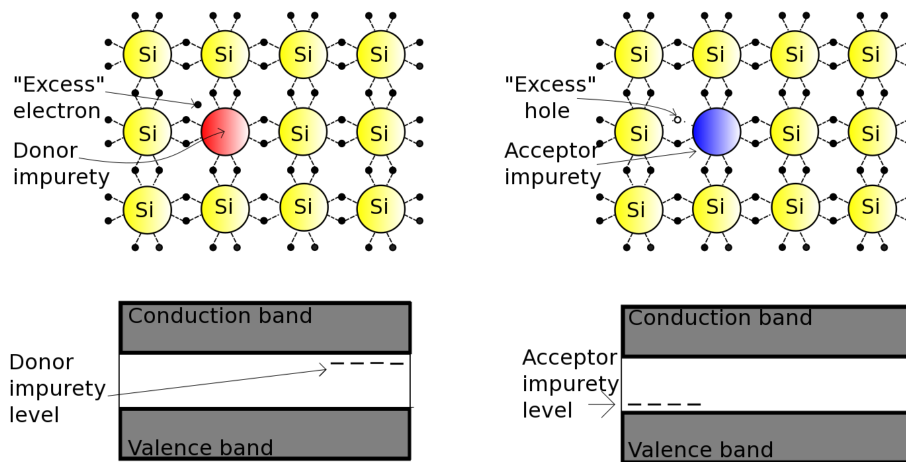

Figure 2.7: Illustrations of the principles of doping with lattice structures above and energy bands below. In n-doping a 5-valence atom is added to the silicon, leaving one excess electron, while in p-doping a 3-valence atom is added, creating a hole where the missing electron should be.

defects in the crystal might give rise to the same type of effects [5]. Silicon detectors are therefore produced from materials with very high purity.

2.3.5 Doping

If impurities in the crystal are added in a controlled manner, then they are quite beneficial. To dope a crystal one introduces a small amount of impurity atoms with one more or less valence electron: The semiconductor is then called an extrinsic semiconductor. Figure 2.7 illustrates both these cases.

If the impurities have one more electron in its valence band (for example Phosphor) the result is an excess of loosely bound electron in the covalent binding of the atoms and then the impurity is called a donor impurity or n-doping (n for negative charge carrier). The electron is located 0.045 eV below the conduction band and can be raised by thermal vibration energy at room temperature. Therefore for every impurity there is a donor electron available for conduction.

If the impurities have one electron fewer in its valence band (for example Boron), this is called an acceptor impurity as it can accept weakly bound electrons. Here the four lattice bonds are incomplete and an electron will be transferred from the valence band to rectify this . The electron then leaves a vacancy in the valence band (hole) which can be used for conduction. The acceptor impurity level is only 0.16 eV above the valence band. This is also called p-doping as the charge carrier is positive.

Concentration of dopant and the conductivity and resistivity of a material

Normal doping has a concentration of a few parts per billion or 10^{13} atoms pr cm^3, but higher concentrations can be a great advantage especially as an electrical contact for semiconductors. Heavily doped materials are marked with a "+" or even "++" to separate the different doping levels. These can have impurity concentrations as high as 10^{20} atoms pr cm^3 and are, therefore, highly conductive.

The conductivity of a material is given by

$$\sigma = en_i\left(\mu_e + \mu_h\right). \tag{2.5}$$

where n_i is the intrinsic carrier concentration and μ_e and μ_h are the mobility of the electrons and holes respectively. The resistivity, ρ, is the inverse of the conductivity. The conductivity and resistivity of a doped material can be calculated from the dopant concentration and the mobility of the majority carrier.

$$\sigma = \frac{1}{\rho} = eN_D\mu_e, \tag{2.6}$$

is the conductivity of a n-type material, where N_D is the concentration of impurities.

2.3.6 P-n junctions:

All semiconductor detectors are based on a semiconductor junction. The simplest form of junctions is the p-n junction, which is a p-type semiconductor and a n-type semiconductor joined together by a special technique.

Figure 2.8 illustrates how mobile electrons from the n-types and mobile holes from the p-types, drift across the junction and combine with each other. The n-type is now left with a positive charge layer and the p-type with a negative charge layer. These charge layers generate an electric field,

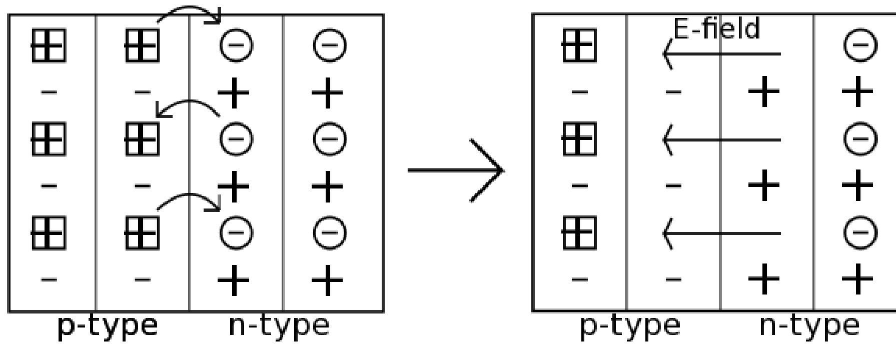

Figure 2.8: A p-n junction, where free electrons and holes from the n-type and p-type material recombine, thus leaving charge layers on both sides that generates an electric field E across the junction.

E, across the junction. This area across the junction is now completely depleted of charge and there is no charge flow [6]. The area is referred to as the depletion zone.

2.3.7 Application of voltage to a p-n junction

One can apply bias voltage on the junction, leading to two different cases, forward and reverse bias voltage.

If one applies a so called forward bias voltage, then the diffusion current increases. The entire region of the semiconductors is in this case filled with charges making it an excellent conductor, but leaving no potential gradient to separate any charges, and thus electron hole pairs will recombine easily. In this state, the junction is not suitable for radiation detection.

Applying reverse bias voltage acts to detain the diffusion current. The donor electrons are attracted to the positive charge applied on the n side and the acceptor holes are attracted to the negative potential applied on the p side. This results in a potential difference and the depletion zone becomes wider with a stronger electrical field strength [4].

Figure 2.9 illustrates the band structure in an asymmetric p-n junction, without and with applied reverse bias voltage. Both the thickness of the depletion layer and the potential difference between the two layers increases if voltage is applied.

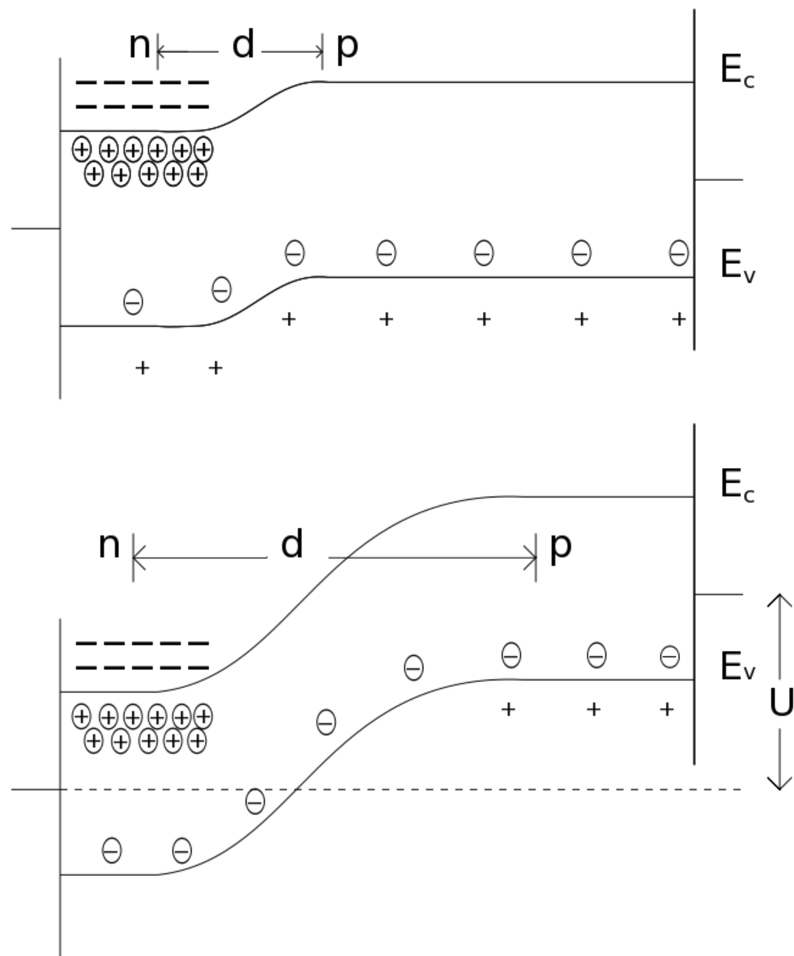

Figure 2.9: Band structure in an asymmetric p-n junction, without (top) and with (bottom) applied reverse bias voltage U. The thickness of the depletion layer,d, and the potential difference between the two layers increases with U. E_c is the lower limit of the conduction band, while E_v is the upper limit of the valence band [4].

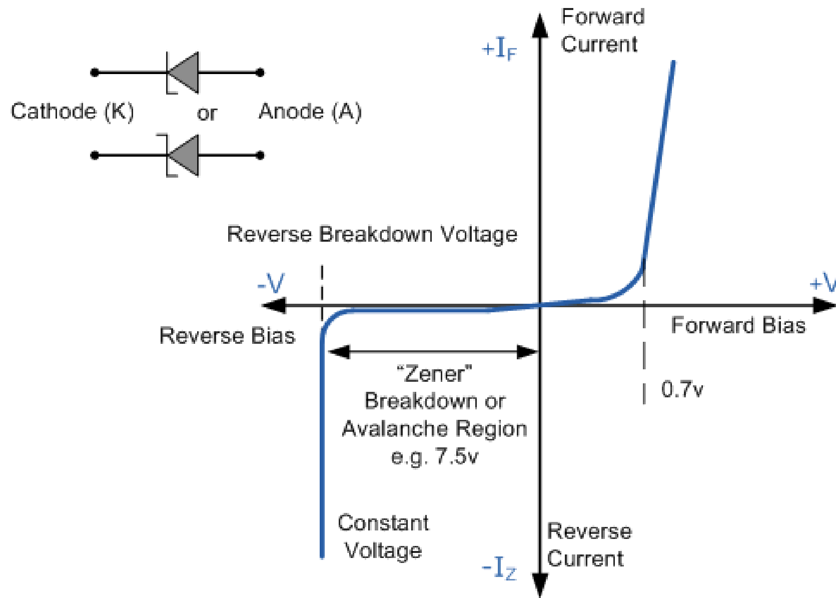

Figure 2.10: Current vs applied voltage across a p-n junction. The suddenly increase in value at reverse bias voltage starts at the so called breakdown voltage [7].

Diode current

The characteristic of the current as a function of the applied bias voltage shown in figure 2.10 whether this is forward or reverse is given by the equation [8]:

$$I_{net} = I_0 \left(e^{+eV_b/kT} - 1 \right) \tag{2.7}$$

Where I_0 is the current without any bias voltage, V_b is the bias voltage, k is the Boltzmann constant, and T is the temperature. At breakdown voltage, there is a suddenly increase of current value. This is either called a Zener breakdown, where electrons are stripped from their atomic bonds, or it is called an avalanche breakdown, where free electrons are accelerated across the junction, and gain enough energy to break loose other electrons.

2.3.8 Junction capacitance

Capacitance is a measure of how much energy is stored for a given electrical potential, and will affect the noise characteristics when a p-n junction is used as a detector. For planar regions the capacitance is

$$C = \varepsilon A/d \tag{2.8}$$

Where A is the area of depletion zone and d is the width of depletion zone

2.3.9 Energy deposition in a semiconductor

When a particle passes through a semiconductor, less than a third of the energy deposited in the material is converted into an electron-hole pair, while the rest goes into lattice vibrations. The energy required to form an electron-hole pair is independent of radiation type and energy at any given temperature. It is only material dependent and for semiconductors, this energy is very low. Therefore, semiconductors have an energy resolution that is much higher than for gas detectors and scintillators, as the number of pairs created for any given radiation is several orders of magnitudes larger than the number of electron-ion pairs or photo-electrons in these detectors.

Relation between Energy deposition and voltage

The observed voltage on the electrodes is expressed as

$$V = \frac{Q}{C} = \frac{n\Delta E}{wC}. \tag{2.9}$$

where ΔE is the energy loss, w is the average energy of an electron-hole pair and C the capacitance. The charge collection efficiency,n, is an important parameter that depends on a number of parameters such as readout spread, bias voltage and the amount of radiation damage. Equation 2.9 expresses the voltage as a linear function of the energy ΔE. This relation is only linear for lighter particles such as electrons and positrons, but for heavier particles the charge collection efficiency varies.

2.3.10 Damages done by radiation to a crystal

Semiconductors are very sensitive to radiation damage, which gives rise to reduced detector performance, a higher leakage current and degraded energy resolution. The fundamental damage mechanisms are lattice displacements that are caused by the incoming particles colliding with the lattice atoms and changing their arrangements. These are lasting damages, which increases the number of discrete recombination centers in the forbidden band gap which again reduces the number of charge carriers. The effect of radiation damage can be reduced by decreasing the collection time. Either by increasing the bias voltage or by decreasing the drift distance. The last option will be discussed further in the subject of 3D sensors (section 2.5).

2.3.11 Effects of temperature

Temperature affects the conductivity of a semiconductor detector. Germanium detectors need to be cooled to low temperatures before operated or else the high leakage current will cause irreversible damage to the crystal. Silicon does not necessarily need to be cooled, but an increase in temperature causes higher leakage current and noise. The upper temperature limit

for silicon detectors at which a break down occurs is between 45 °C and 50 °C [5]. By reducing the temperature one can reduce the noise.

2.3.12 Detector efficiency

When describing detector efficiency one generally refers to the total efficiency and the intrinsic efficiency of a detector.

If a detector is exposed to a radioactive source, then its intrinsic efficiency is the fraction of the particles actually passing through the detector that are registered as a signal [5]:

$$\varepsilon = \frac{N_{\text{reg}}}{N_{\text{true}}} , \tag{2.10}$$

where N_{reg} is the number of registered events and N_{true} the number of true events.

The intrinsic efficiency is a function of the radiation type as the probability of registration is dependent on the interaction cross section between the incident radiation and the detector medium.

The intrinsic efficiency of a semiconductor is generally very high. However, there are some limiting factors such as; noise from leakage current and the detection threshold of the electronics. If the signal amplitude fails to reach the threshold value, then the event will not be registered and the efficiency will, therefore, decrease. The depletion depth of a sensor must be chosen carefully to achieve a balance between noise reduction and the ability detect low signal events.

Geometrical efficiency is the the fraction of the radiation from a source intercepted by the detector; i.e. the average solid angle fraction.

The total efficiency of a detector is the fraction of radiation events emitted from a source that is registered by a detector. This is a function of intrinsic efficiency and geometrical efficiency (geometrical acceptance).

2.3.13 Leakage current

If a voltage is applied to a semiconductor detector, then a small fluctuating current flows through the semiconductor junctions and adds noise to the output signal. The largest contribution to leakage current is through surface channels, which is due to complex factors such as contamination and surface chemistry. Other sources can have a small effect from minority carriers that move across the junction or trapping, and recombination centers that might catalyze the creation of electrons and holes from the valence band [5].

2.4 Planar semiconductor detectors

Of all the semiconductor detectors, a planar geometry is the most usual.

Electrodes are implanted at either side of a Silicon wafer in order to collect the charges induced by the radiation. The two conventional readouts of the planar semiconductors for the ATLAS inner detector are the pixel readout and the micro strip readout.

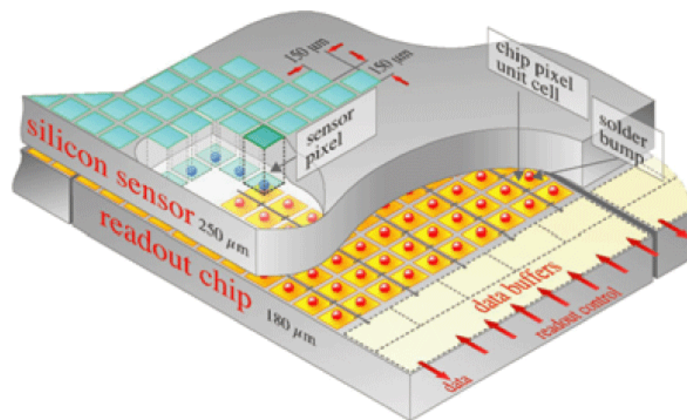

Figure 2.11: Illustration of a planar silicon detector with pixel readout [9]

Pixel detectors are made of an array of small silicon pixels (physically isolated pads), which gives an excellent two-track resolution. The pixels are bump-bonded to a pixellated readout chip and only the pixels with hits that give a signal above a certain threshold is read out.

The micro-strip readout is a more economical readout alternative, for which the sensor is read out using electrode strips implanted on the surface.

The planar silicon detectors are protected from current leaking around the edges by guard ring structures surrounding them. To obtain good signal to noise characteristics for the detectors it is necessary with a pulse shaping in the processing of the signal.

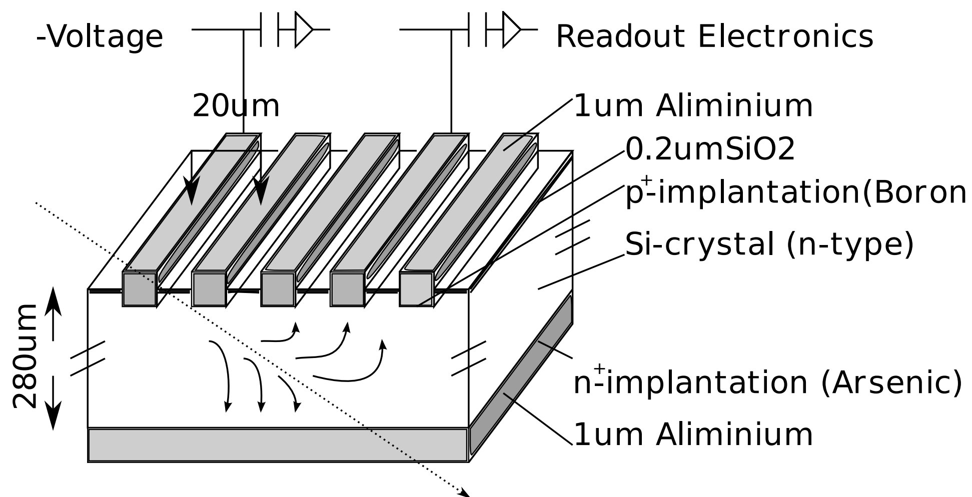

Figure 2.12: Illustration of a planar silicon detector with micro-strip readout

2.5 The 3D silicon sensor with active edge

3D silicon sensors are semiconductor sensors with the electrodes etched into the silicon wafer in columns of vertical cylinders as opposed to implants on the wafer's surface as for planar sensors [10–15]. It is this structure of electrodes in three dimensions shown in figure 2.13 that has given it the name 3D, and not the commonly misconception that the sensor produces three dimensional images of the radiation through a single sensor.

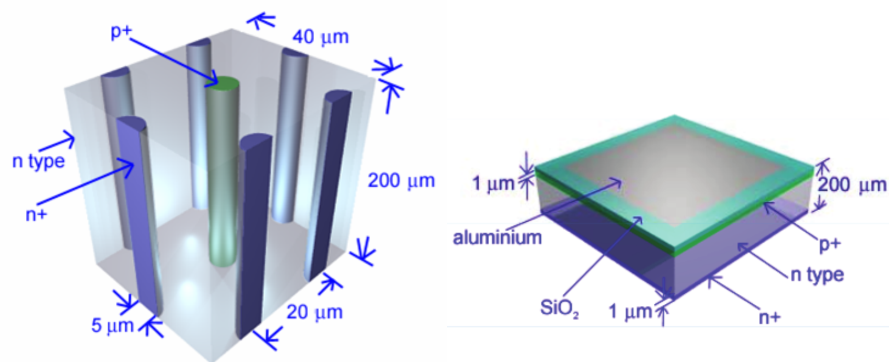

Figure 2.13: The principle features of a 3D Silicon Sensor's architecture (left) compared to the planar architecture (right). While the planar device has electrodes implanted on the wafer surfaces, the 3D sensor has electrodes penetrating the wafer.

3D silicon detectors were proposed in 1995 by S. Parker, active edges were proposed by C.Kenney in 1997, both of which made possible by a combination of the current state-of-the-art, Deep Reactive Ion Etching (DRIE), that allows etched vertical structures with an aspect ratio AR = D/d of over 20 and the two conventional fabrication techniques, Very Large Scale Integration (VLSI) and Micro-Electro-Mechanical-Systems (MEMS) [10].

The electrodes fully or partly penetrate the silicon substrate which allows several readout schemes, for example the micro-strip and pixel readouts (section 2.4). The electrode pins generate an electrical field between them, which guides the charges produced by radiation to the electrodes for readout as shown in figure 2.14. The 3D geometry allows for very short drift distances (typical 50 -100μm) which have several benefits.

One of the most obvious advantages of a very short drift distance is that the charge collection is much faster in 3D sensors than in the planar sensors. The charges in the perpendicular tracks come in simultaneously, rather than

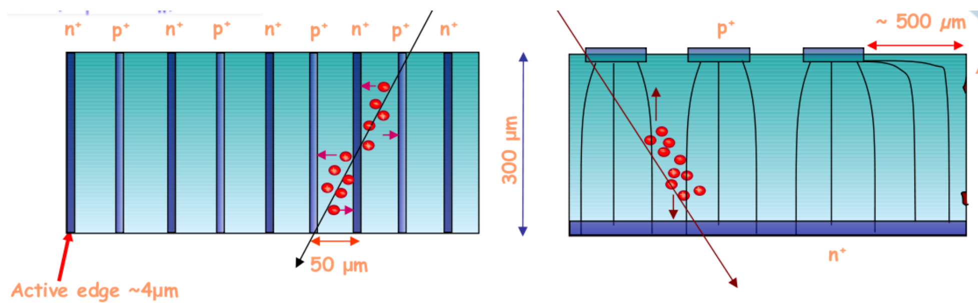

Figure 2.14: Illustration of the difference in drift distance between a planar sensor and a 3D sensor [16].

sequently, which results in an order-of-magnitude shorter pulse.

The short drift distance also makes the sensors more radiation hard. The short distance between the electrodes increase the probability that the charge carriers reach the electrodes before being trapped and, hence, causing permanent changes in the crystal lattice. Radiation hardness is a key property required for the inner b-layer of the ATLAS detector. In this layer, primary and secondary vertices of very short lived particles are reconstructed with high precision. Damage in the crystal due to radiation will significantly degrade the sensors performance and, therefore, these sensors will eventually need to be replaced.

Another advantage of a short electrode distance is that the 3D sensors can be depleted and have full sensitivity at lower bias voltages than planar sensors. Also, the electrode surface is larger in 3D sensors than in planar. This means that for any given applied voltage, the electric field is much larger for 3D sensors than for planar.

Planar detectors are surrounded by guard rings that protect the detector from current leaks at the edge. These guard ring structures have an edge efficiency loss associated with them. The 3D sensors have eliminated the need for these guard rings and are efficient all the way to the edge because of an etched and doped edge-electrode that completes the horizontal electric field lines as shown in figure 2.15. This reduces the amount of dead material, which is good for both large area and low mass devices for high energy physics detectors and for medical and biological imaging.

One of the drawbacks of 3D geometry is that the volume occupied by the electrode columns is not fully efficient for the tracks normal to the sensor surface and the inefficient volume is determined by electrode density and the hole aspect ratio.

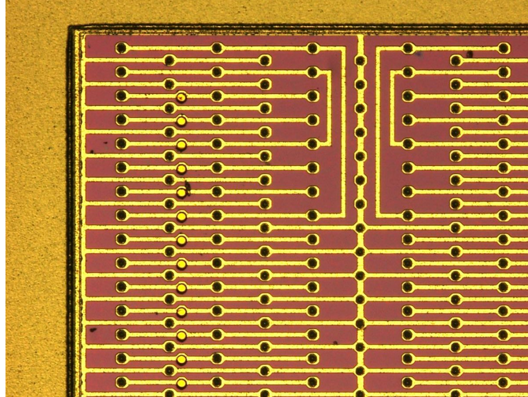

Figure 2.15: Depiction of a sensor's edge, illustrating the continuous electrode around the edge [17].

Because of the short distance between the electrodes and the high electrode density, 3D detectors have a higher associated capacitance than planar sensors [11]. This implies a higher noise level for the 3D sensors than for the planar sensors.

The production of the 3D sensors is a very difficult, time consuming process in which a significant percentage of the sensors are either not working or are defective.

2.5.1 Electrode configuration layouts

3D sensors sensors layouts are characterized by the number of readout electrodes per 50 μm $\times$ 400 μm ATLAS-compatible pixels as shown in figure 2.16. There exist two, three and four electrodes configurations.

2.5.2 Readout of the 3D sensor

The 3D sensors are bump bonded to a FEI3 pixel readout chip. This is the ATLAS pixel readout chip used for all the sensors under study in this thesis. Bump bonding shown in figure 2.17 is a very complex soldering technique that connects each pixel to a FEI3 readout cell. A system to performed a such accurate technique is located in Bonn and the 3D sensors from SINTEF are bump bonded there.

The FEI3 contains 2880 readout" cells of 50μm x 400μm size arranged in a 18x160 matrix. Each readout cell contains an analogue block where the sensor charge signal is amplified and compared to a programmable threshold by a discriminator. The Digital readout part transfers the hit pixel address,

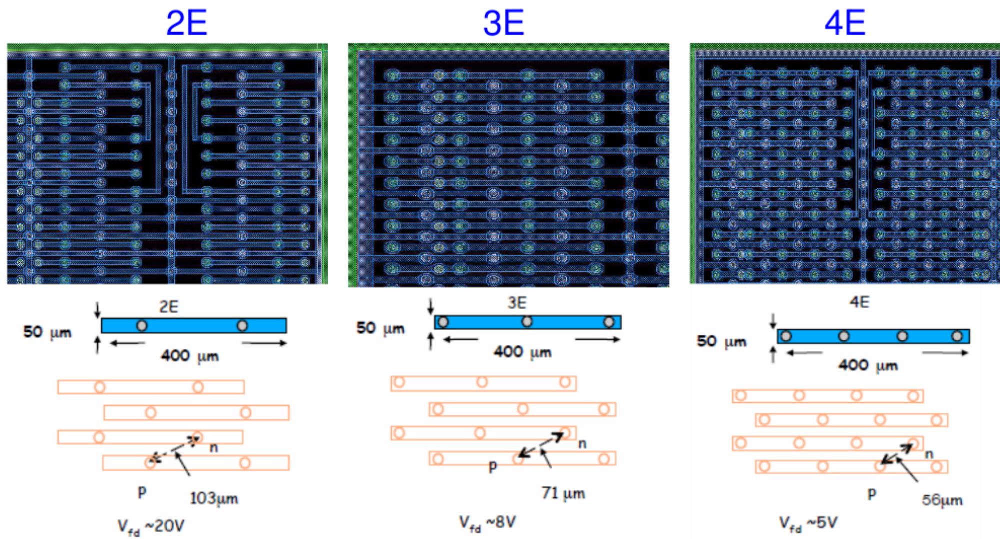

Figure 2.16: The electrode configurations for 2E, 3E and 4E-sensors with the respective number of readout electrodes in a pixel of 50 $\mu m \times 400$ μm [13].

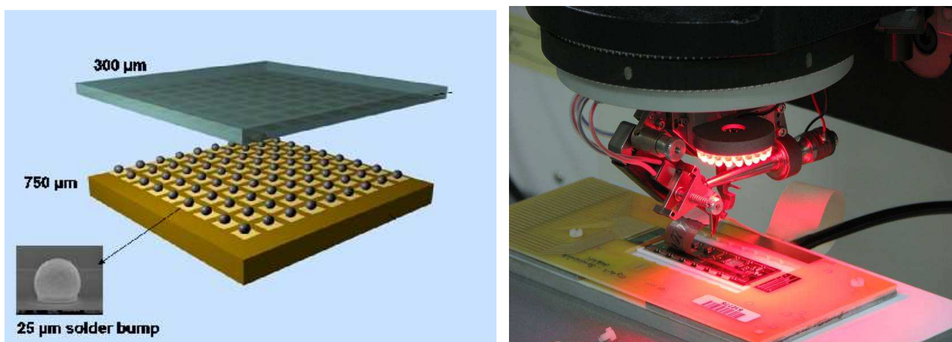

Figure 2.17: Bump bonding of sensor to the FEI3 readout chip performed in Bonn. Each bump has a diameter of only 25μm [16].

a hit time stamp and a digitized amplitude information at the time over threshold (ToT) to buffers at the chip's periphery." [18].

The second most important part of a semiconductor detector system (after the detector itself) is the charge sensitive preamplifier. The charge sensitive preamplifier was originally designed for semiconductor detectors, which have changes in their capacitance with temperature. The charge sensitive preamplifier is insensitive to changes in the capacitance and, therefore, makes it a preferred choice compared to other preamplifiers. The basic idea is to integrate the charge carried by the incoming pulse on the capacitors.

2.5.3 Time over Threshold

The time over threshold (ToT) is a measure of how long time a signal is above a certain minimum detection threshold. The ToT is proportional to the charge deposited in one pixel, hence the radiation energy . (since the number of charges liberated is proportional to the energy of the radiation). ToT depends on deposited charges, discriminator threshold and feedback current.

Chapter 3

The Large Hadron Collider and The ATLAS experiment

3.1 The Large Hadron Collider

On the 10Th of September 2008, The Large Hadron Collider (LHC) had its first successful circulation of proton beams of protons [19]. LHC is the largest accelerator in the world with a circumference of 27km, running about 100 meters underground on the French-Swiss border near Geneva. LHC was newly built in the tunnels of the previous Large Electron Positron collider accelerator (LEP) at The European Organization for Nuclear Research (CERN -the largest particle physics laboratory in the world).

In LHC protons are being accelerated to extremely high energies, expected to provide collisions with a center of mass energy of 14 TeV (Each proton has the energy of 7 TeV) [21]. The protons are obtained by ionizing hydrogen and are grouped together in bunches containing 1.15×10^{11} protons, with each bunch separated by 25 ns [22] . A beam consists of 2808 bunches, and one individual proton takes about 90 μs to travel around the collider. The beam of protons is accelerated by magnetic fields created by superconductive magnets and split up in tubes going in opposite directions. There are additional magnets to steer and focus the proton beams into each other at the four collision points, one of which is (A Toroidal Lhc ApparatuS) ATLAS detector. The beams can be up to a few mm wide while circulating in the accelerator and are squeezed together into 64 μm at the collision points in order to increase the probability of collisions [23].

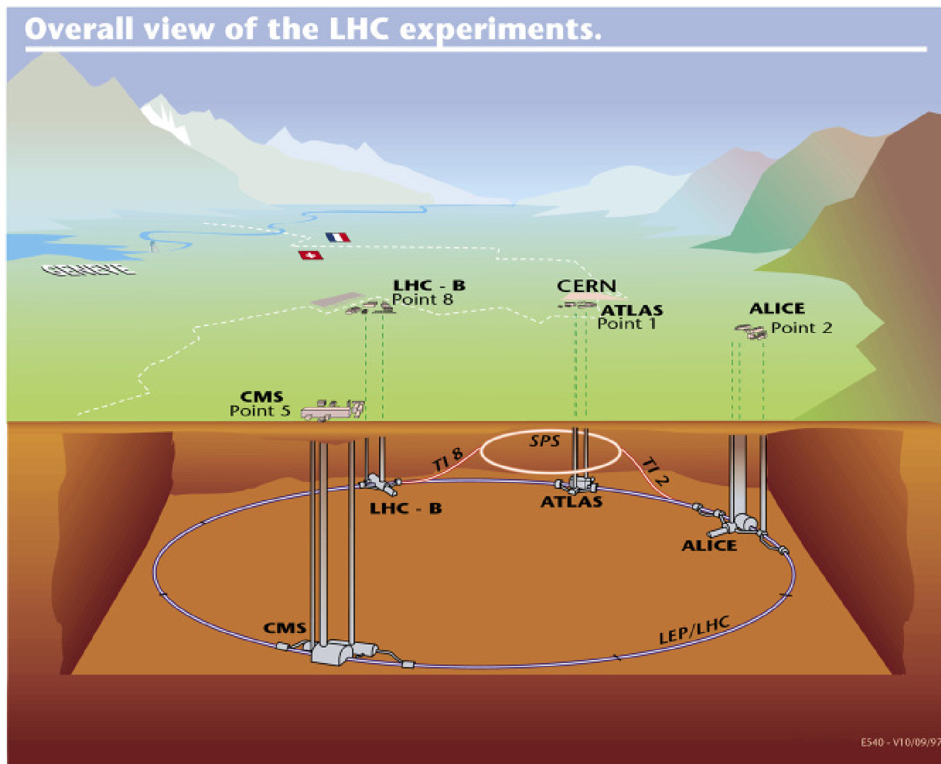

Figure 3.1: The Large Hadron Collider on the French-Swiss border showing its experimental sites [20].

3.1.1 Cross section and luminosity

Before discussing the LHC experiment further, two very important parameters in colliding beam experiments should be discussed; the cross section and the luminosity.

The number of events per unit time N_s is a product the luminosity $\mathscr{L}$ and the cross section σ_{tot} [24].

$$\mathscr{L} = \frac{N_s}{\sigma_{tot}} = \frac{N_1 N_2 f k_b}{A}, \tag{3.1}$$

Equation 3.1 expresses the luminosity in the interaction region of two beams, where f is the revolution frequency of the beams, bunch i contains N_i particles, k_b is the number of bunches in a beam and A is the area. The luminosity is usually expressed in the units of $\left[cm^{-2}s^{-1}\right]$.

The total cross section σ_{tot} is a measure of the probability for a collision between beam particles. The cross section has the dimension of area, and has the unit of barns in subatomic physics.

$$1barn = 1b = 10^{-28}m^2(= 10^{-24}cm^2 = 100fm^2) \tag{3.2}$$

At low energies the cross section decreases with the particle energy as $1/E^2$. The cross sections for the processes looked at at the LHC is very low, and thus the luminosity of the experiment must be increased in order to provide a high enough rate of collisions.

In the LHC experiment a luminosity of 10^{33} $\mathrm{cm^{-2}s^{-1}}$ was expected during the first three years of operation, and then reaching its design luminosity of 10^{34} $\mathrm{cm^{-2}s^{-1}}$. However, technical problems have forced a shut down for almost a year and caused delays to the original schedule. When design luminosity is reached, one would expect it to lead to new advances in particle physics.

3.1.2 The LHC experiments

The LHC has six experiments conducted by international collaborators. These are all characterized and made possible by its unique particle detector systems.

The LHC has two high luminosity experiments, ATLAS and The Compact Muon Solenoid (CMS), that aim for handling a peak luminosity of 10^{34} $\mathrm{cm^{-2}s^{-1}}$. Both of these detectors are designed to investigate the largest range of physics theories as possible, and two independently designed detectors are for cross-confirmation whenever new discoveries are made.

ALICE (A Large Ion Collider Experiment) and LHCb (Large Hadron Collider beauty) are two medium-size experiments, which are designed for special particle physics phenomena. The LHCb is a low luminosity experiment designed for B-physics, while ALICE is a dedicated ion experiment. TOTEM (Total Cross Section, Elastic Scattering and Diffraction Dissociation) and LHCf (Large Hadron Collider forward) are two smaller experiments [21, 25].

3.2 The (A Toroidal Lhc ApparatuS) ATLAS detector

The ATLAS detector is one of the largest collaborations ever in the physics world, involving 2900 physicists, 172 universities and laboratories and 37 countries . It is more than 25 meters high and 45 meters long (The official outreach page for the ATLAS Experiment at CERN, 2010) [26].

3.2.1 Physics studied in the ATLAS detector

The Standard Model (SM) is a theory, that describes all particles yet known and all interactions between them with only 6 quarks, 6 leptons and force carrier particles shown in figure 3.2.

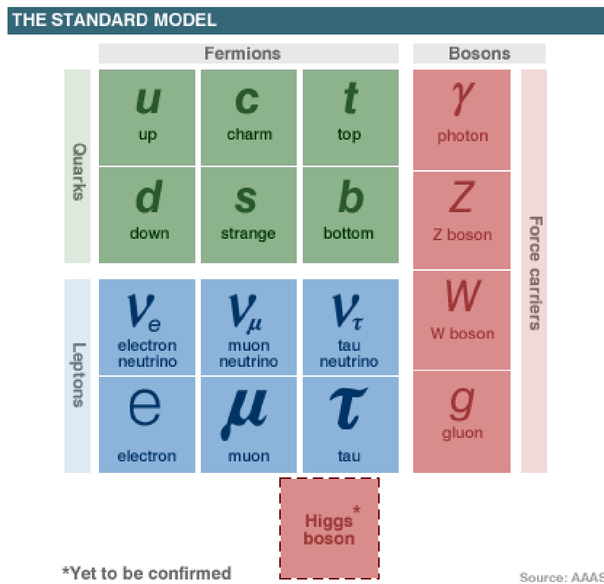

Figure 3.2: The Standard Model (SM) [27]

This theory stands very strong as it has accounted correctly for a wide range of observations, and all particles that had been predicted by this the-

ory have now been found, except the Higgs Boson. The SM does however leave a number of fundamental questions unanswered. The gravity for example, is not explained by the SM [8].

The main purposes of the ATLAS detector are; measurements of known SM- physics, like the top quark mass and the W-boson mass,and to contribute to the search for the Higgs Boson and new physics behind the SM. Higher precision than previously obtained is possible because of the high number of detectors and the high event rate from the LHC. The ATLAS detector has high a potential for discovery of new physics up to the TeV-energy region, which so far is unexplored.

In the high energy collisions of protons in the ATLAS detector, many short lived particles are created. These particles do not leave direct tracks in the detector, but can only be found by studying their known decay products.

3.2.2 Layout off the Atlas detector

The ATLAS detector consists of four main components. The three main detector systems are: i) the Inner detector; which measures the momentum of charged particles, reveals their trajectories and scattering angles, ii) the calorimeter, which measures the energies carried by both charged and neutral particles and iii) The Muon spectrometer that identifies and measures muons. The fourth major component is the magnet system that bends the charged particle's trajectories in order to measure their momentum (Figure 3.3) [28]. The combination of different detector systems and methods will make it possible to identify a large scale of particles. Figure 3.4 show that the different properties of particles gives them a unique signatures which can be identified in the ATLAS detector.

The inner detector

The inner detector roughly consists of the Pixel detector, the semiconductor tracker and the transition radiation tracker. It combines high-resolution detectors closest to the beam pipe with continuous tracking elements farther out. The inner detectors are all arranged within a central solenoid (CS) that provides it with a nominal magnetic field of 2 Tesla.

The Pixel detector is designed to provide precise tracks as close as possible to the interaction point. One reason for this is to reconstruct the trajectories of very short lived particles such as B-hadrons and τ-leptons. To obtain tracks with such high resolution, planar silicon pixel sensors are used.

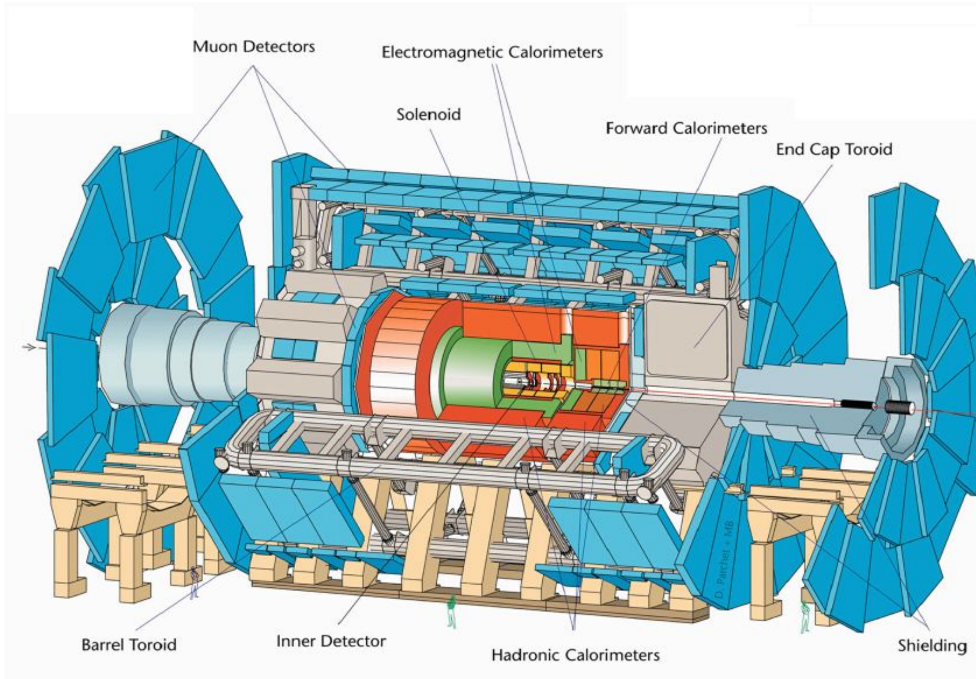

Figure 3.3: Overall layout of the ATLAS detector [29]

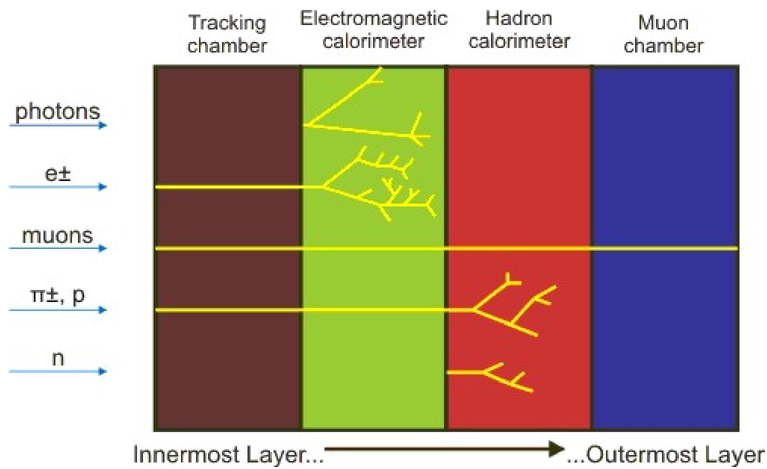

Figure 3.4: Principle for identification of high energy particles in the ATLAS detector layers. One can identify the particle type by noting in which layers of the detector the particle leaves tracks. Photons, electrons, muons, hadrons and neutrons all their their individual signatures in the detector layers [30].

3.3 ATLAS upgrade activities

There are constant activities to upgrade the ATLAS detector for several reasons.

One expects that after a period of six years of collecting data at the nominal LHC luminosity (10^{34} interactions per second per cm^2 of cross section), further improvements in error bars will be very slow.

Another reason for upgrading the detector is that eventually it will have reached its designed lifetime with respect to the radiation dose it can take before its performance is significantly degraded.

Also the inner triplet quadrupole magnets used to focus the beam on the interaction point of ATLAS may need replacement due to radiation damage.

3.3.1 The plans for upgrading LHC

The further development to increase the luminosity of LHC is divided into phase-I and phase-II.

Phase-I of the LHC upgrade is at the earliest expected to start at the end of 2013. There will be a six to eight month shut down to perform installation of the machinery that will take the luminosity up to 2-3 times the nominal luminosity. During this shut down a new linac (Linac4) will be brought on-line and the inner triplet magnets will be replaced with larger ones. During the shut down there will also be a good opportunity to make improvements or replacements in the detectors.

Phase-II of upgrading to super LHC (sLHC) has a goal to bring the luminosity up to 10 times the nominal luminosity, and there are several options under investigation to achieve this increase.

3.3.2 The scheduled ATLAS upgrade activities

Prior to the next phase of the LHC upgrade, ATLAS will need to evaluate the necessary changes to make the most of the advantage of the increased luminosity. For now a new insertable B-layer (IBL) is under development that will be inserted inside the current pixel detector on a smaller beam pipe during the shut down for phase-I upgrade. The 3D sensor is a leading candidate for this upgrade [31].

For the second upgrade phase, major changes to ATLAS will be necessary to cope with such enormous data rates and radiation levels. The largest

ATLAS upgrade project will be the replacement of the entire inner tracker. Also other issues are being considered such as optimizing the trigger and data acquisition systems to cope with a much larger raw data rate and also improve the forward liquid argon calorimeter's performance at high luminosity [32].

Compared with the present detector, it will need to have a reduced depletion voltage, a reduced capture of charge carriers, increased speed and a smaller charge sharing region to minimize further reduction of signal size [33]. For this the 3D sensor might be a strong candidate.

Chapter 4

Test beam activities

To investigate the properties of the 3D-sensors with an active edge, several test beam activities have been and are still taking place. At test beam June 2008 the motivation for the tests was to study edge effects of the detector, test an irradiated detector and to perform bias scans.

4.1 Testbeam 2008

The data used in this thesis' analysis are from a test beam in 2008. The 2008 test took place during two weeks in June at CERN using a 180 GeV/s $\pi^{\pm}$ beam. The 3D detectors tested were produced by Stanford and bump-bonded to the ATLAS FE-I3 readout chip in 2006. For a complete list of participants see [34].

4.1.1 The devices under test

During this test beam three different sensors were under test. These were designed and manufactured by J. Hasi (University of Manchester) and C. Kenney, (MBC at CIS-Stanford). The sensor layouts were characterized by having 2, 3 or 4 readout electrodes per pixel. The p and n electrodes were fully penetrating the detector wafer and the edge was etched and implanted as an electrode. The modules that were tested were named: 4E-C, 3E-G and 3E-S (This 3E assembly was irradiated with 9.8×1014 cm^{-2} 24GeV protons.)

4.1.2 Data collecting

The test beam was a 180 GeV/s $\pi^{\pm}$ beam provided by the SPS machine which is is the second largest machine in CERN [35]. The pion beams are ideal for characterization of high precision tracking detectors, because their high momentum gives a minimization of multiple scattering in the experimental setup.

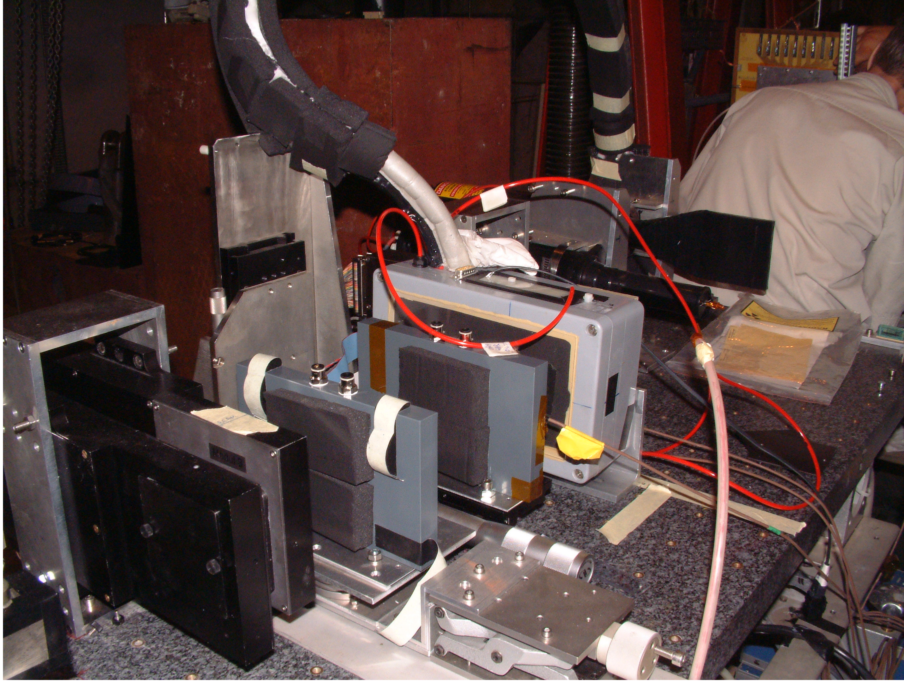

Figure 4.1: Picture taken of the setup at the test beam in 2008 [34]

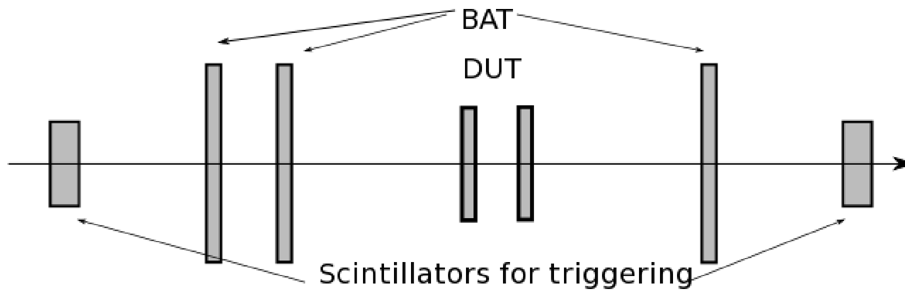

Figure 4.2: Schematic drawing of the 2008 test beam setup.

During data taking, the pions passed through several detectors and scintillators in the setup shown in figures 4.1 and 4.2. For triggering the readout of the detector, coincidence of several overlapping scintillators was used. A sub-ns resolution Time Digitization Counter (TDC) recorded the phase of each trigger with respect to a 40 MHz "LHC"-clock to study the electronics time walk.

There is a very well calibrated beam telescope that provides the information on the real tracks. The beam telescope (Bonn Atlas Telescope (BAT)consists of three planes of 50 μm pitch double sided Silicon strip detectors, provided by Bonn university, and tracks were reconstructed whenever an event had exactly one hit in each telescope plane. When a particle traversed several layers in a row, a track was reconstructed even though the hits were not always on a line. The recognition of a track of a particle depends of the detector calibration and performance [17].

When a charged pion traverses the detector material, an electron-hole pair is created in the respective pixel. As the charges drift towards the electrodes, a current is read out and is registered as a hit in this pixel. Information of ToT is read out together with the hit address in units of 25 ns.

4.1.3 Track reconstruction and alignment

During the test beam 2008 almost 1100 runs were completed with two modules in the beam at each run. The majority of these runs were very short. The reconstruction code preformed by Ole Røhne and Håvard Gjersdal consisted in BAT clustering with many corrections, checking synchronisation by finding the correlation of cluster positions in the BAT modules and keeping events with cluster in each BAT layer. The alignment of BAT is checked by the biased residuals (the position of cluster - the position of the track at the surface), while the alignment of the Device Under Test (DUT) is checked using the unbiased residuals (The center of the pixel - The position of the track) [34].

Chapter 5

Analysis

The analysis presented in this thesis was made using data taken from test beam runs in June 2008 at CERN.The test beam was a 180 GeV/s $\pi^{\pm}$ beam provided by the SPS machine which is is the second largest machine in CERN's accelerator complex. During the test beam runs considered, two modules have been included in the setup every time; a sensor with three electrode configurations; 3E-G for all runs, a four-electrode sensor; 4E-C for the bias scan and a sensor that has been exposed to extreme radiation; 3E-S for a selection of runs. The data from each of the detectors are identified by a module identifier number; 160 or 164.

Table 5.1 gives the run numbers were used in the analysis. Bias voltage was applied to the detectors individually. The 4E-C sensor was replaced with the irradiated sensor; 3E-S for some runs at 80V, but the sensor was completely dead.

The first half of this chapter presents an analysis of the 3E-G sensors performance, and in the second half a short study of the 4E-C sensor.

5.1 Parameters used in the analysis

For the analysis several parameters are considered. These are described in the following sections and summed up in table 5.1.

The sensor consists of a 18 $\times$160 matrix of pixels with the dimensions of 400 μm $\times$ 50 μm. This gives the dimension of 7200 μm $\times$8000 μm for the whole sensor. This measure does not, however, include the "Active edge" electrode that surrounds the sensor.

The three telescopes upstream and downstream of the the sensor give the track positions of the beam. These have the track coordinate (0,0) in

Run numbers	Detector(id:160)/Voltage	Detector(id:164)/Voltage
9493-9496, 9498, 9500, 9503-9505	4E-C/ 10V	3E-G/ 10V
9437, 9444, 9445, 9447, 9449-9445, 9465, 9467, 9468, 9470, 9471, 9476-9484, 9488	4E-C/ 15V	3E-G/ 15V
9420, 9422, 9424, 9425, 9427, 9429-9433, 9436	4E-C/ 20V	3E-G/ 20V
9341, 9342, 9345-9348, 9351-9357, 9359-9370	4E-C/ 30V	3E-G/ 30V
9520, 9534-9536, 9550-9552, 9552, 9554, 9556-9567, 9569	3E-S/ 80V	3E-G/ 40V
9571-9580 (Only used in the alignment study.)		3E-G/ 40V

Table 5.1: Detectors and respective bias voltages for the runs included in the analysis.

the center of the zeroth pixel (The so called zeroth pixel is in reality the first pixel, but has been given its name due to its index number and coordinates.). The track positions given by the beam telescope are called `xTrack` and `yTrack`.

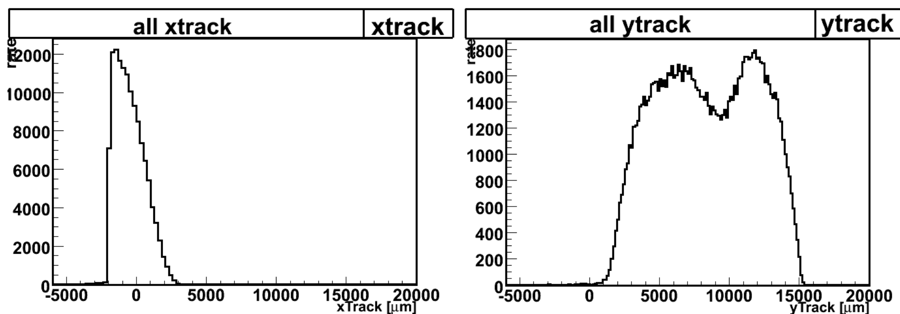

Figure 5.1: x and y profiles of the beam as it is projected in the beam telescope, without any cuts.

In figure 5.1, the x and y profiles of the beam are shown. The beam is not uniform especially the y profile, has two distinctive tops. The reason for the very sharp edge in the x-profile probably is shielding or collimation of the beam in the test beam area before it reaches the test setup. In figure 5.2 a two-dimensional image of the beam profile and how it intercepts with the detector is shown. This illustrates that it is not the most dense area of the beam that has been detected by the sensor. Because of this cuts had to be

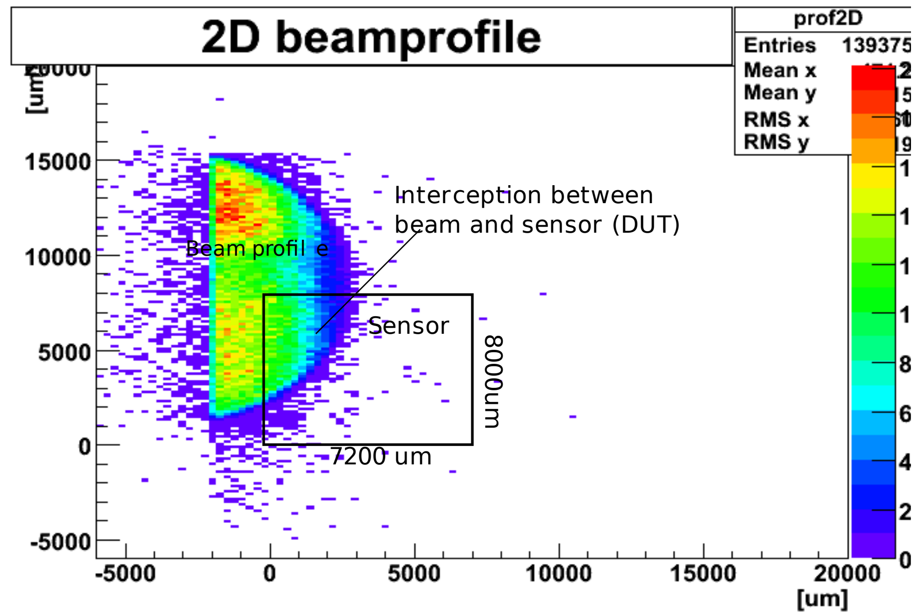

Figure 5.2: Beam profile as it is projected in the beam telescope, without any cuts. The black rectangle represents the 3D detector that is tested. Only the upper corner of the sensor is intercepted by the beam.

placed on impact parameters and slope in the analysis.

Sometimes particles gets slightly scattered from its normally well collimated beam direction. The variables `dxTrack` and `dyTrack` give the change in x or y position as a function of the beam direction, as illustrated in figure 5.3. Figure 5.4 is an illustration of the `dxTrack` and `dyTrack` distributions of the beam tracks. Conditions are defined in the code to keep `dxTrack` and `dyTrack` within two standard deviations of the mean.

When a particle is registered in the sensor, the hit position gets the coordinate of the center of the pixel that is hit. The parameters `difx` and `dify` are the coordinates of the `xtrack` and `ytrack` minus the coordinates of the pixel center as shown in figure 5.5.

.

5.2 Alignment studies

Because the alignment of the sensor was done manually during the test beam, it has been necessary to make adjustments in the the analysis code.

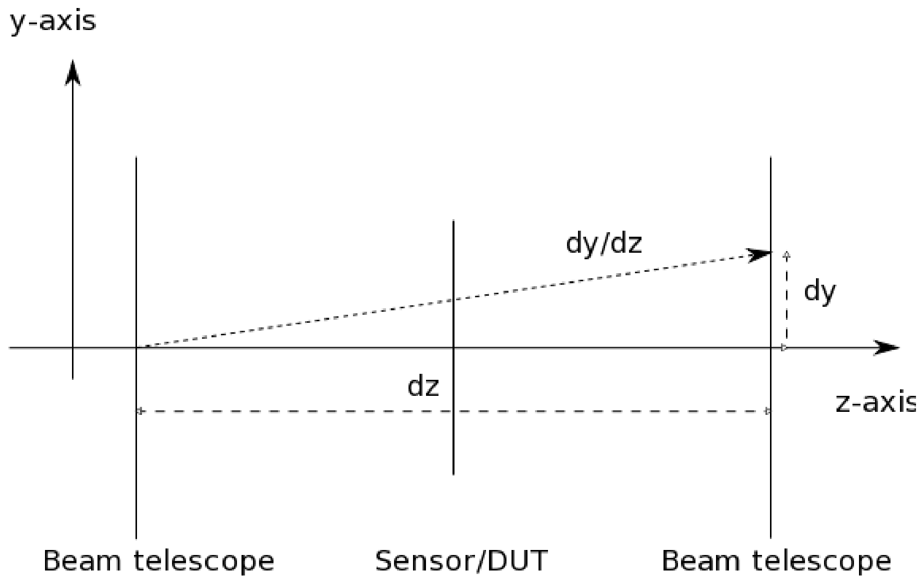

Figure 5.3: Illustration of `dyTrack` = dy/dz whose basic principles also applies to the `dxTrack`. These deviations in direction are due to scattering of the beam

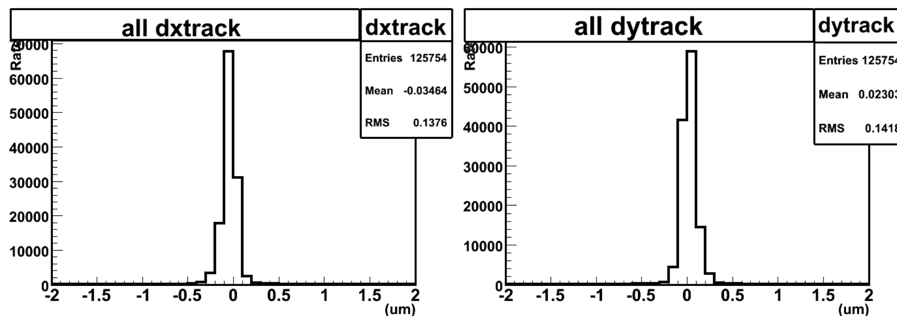

Figure 5.4: `dxTrack` and `dyTrack` distribution of the beam.

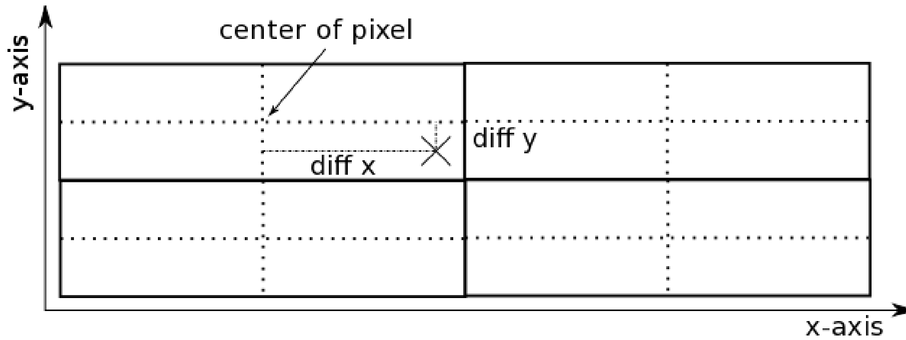

Figure 5.5: Illustration of `difx` = position of `xTrack` minus position of `xpix` (`xpix` = pixel number in x-direction × the pixel size in x-direction) and `dify` = position of `yTrack` minus position of `ypix` (`ypix` = pixel number in y-direction × the pixel size in y-direction).

Parameter	Explanation
`xTrack` and `yTrack`	The track positions given by the beam telescope
`dxTrack` and `dyTrack`	dx/dz and dy/dz of tracks
`xpix` and `ypix`	pixel number in x-direction × the pixel size in x-direction and pixel number in y-direction × the pixel size in y-direction
`difx` and `dify`	position of `xTrack` minus position of `xpix` and position of `yTrack` minus position of `ypix`.
`maxToT`	The ToT value of the strongest signal in one event.
`cluToT`	The sum of ToT value for a cluster of pixel in one event.
`nhit`	The number of pixels with a hit in each event.
`ncluster`	The number of pixels included in a cluster for each event.
`k`	The address of the pixel with strongest signal in that event.

Table 5.2: Parameters considered in the analysis

Alignments studied were performed by Bjarne Stugu and Ahmed Abdelsalam during the summer of 2008as a contribution to alignment of the data from the test beam. The alignment study in this thesis is performed after the realignment of the data made by Håvard Gjersdal and Ole Røhne.

To determine how well aligned the detector is, the distribution of `dify`, which is the difference between track- and hit position(section 5.1), is evaluated. Initially corrections had to be applied to the calculation of hit positions, but after realignment of the data, these corrections were no longer necessary and could be removed.

The `dify` distribution is fitted with a Gaussian distribution to calculate its mean value. The routine is performed for several separate runs, and then the mean value is plotted as a function of run number to see if the detector position is shifting.

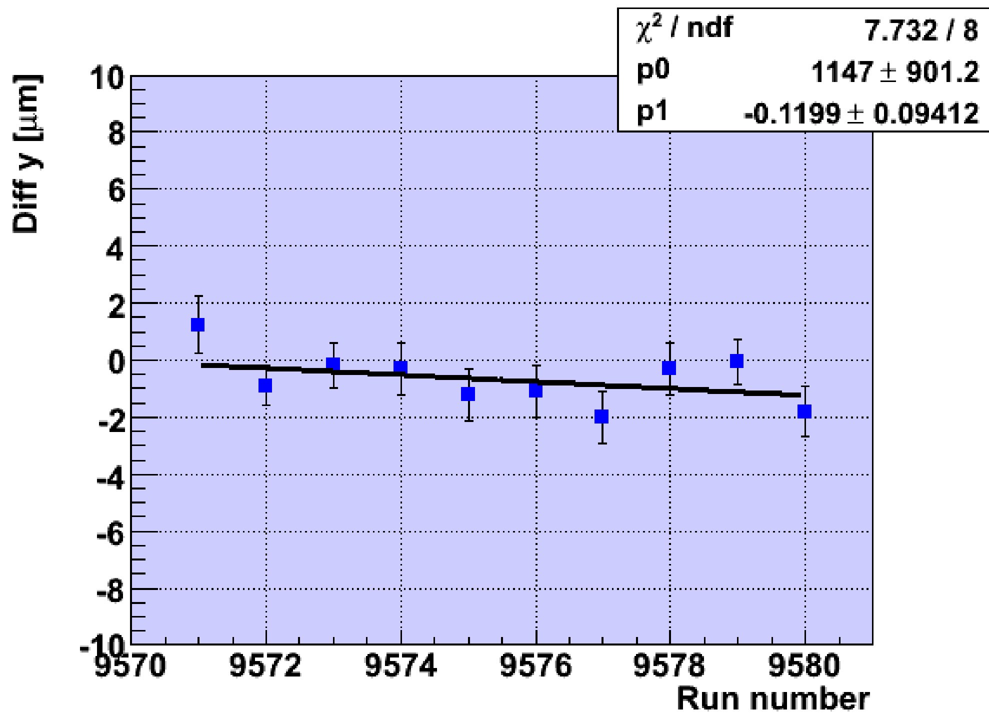

Figure 5.6: Alignment plot: The Gaussian mean of the difference in y-direction between the positions of hits and tracks in units of μm for run numbers between 9571 and 9580. The line is a function y = $p_0 x \ + p_1$.

In figure 5.6 one can see the mean of the distribution of `dify` plotted for 10 separate runs. if the alignment is good these values should be distributed

around 0. In this graph the majority of the points lie below 0, and thus it seems that a possible systematic negative shift has occurred in these runs. There is also a small drift as a function of run number, but one can still claim that the precision of the alignment is very good; better than 3 μm.

5.3 Time over Threshold

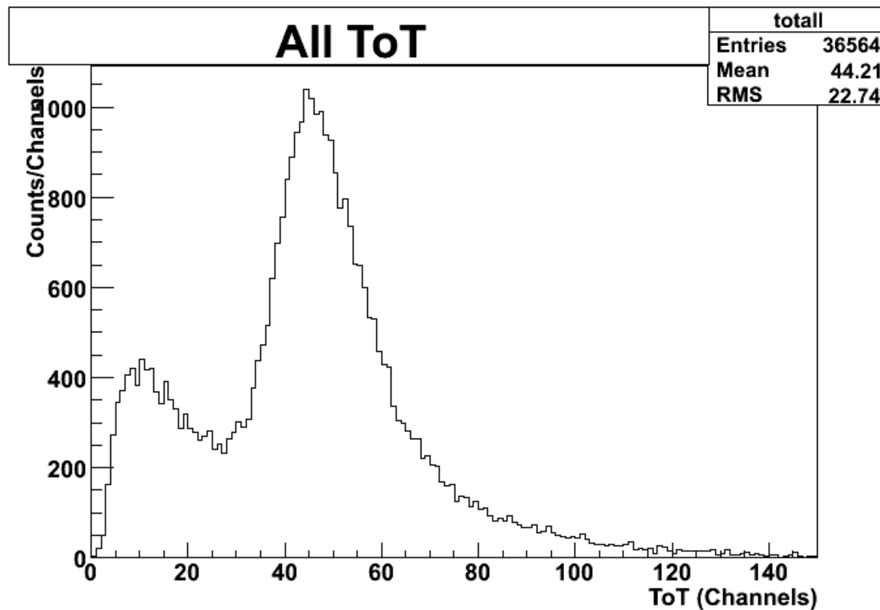

Figure 5.7: All Time over Threshold measured without any cuts

The Time over Threshold (ToT) is the time between which a signal rises above a threshold until it sinks below the threshold again. It is an important parameter to find because it gives a handle on how much energy a traversing particle has lost/deposited in the detector. The ToT is read out in units of 25 ns [36].

First it is necessary to find the pixel with the strongest signal, in other words, the pixel with the highest time over threshold registered in an event. Because a traversing particle does not necessary deposit all its energy into a single pixel, a combined signal from the pixel with highest ToT and the surrounding pixels is considered. This is called a cluster. In figure 5.8 such a cluster of hit modules is illustrated.

In order to find the total signal in the cluster, several steps of loops and if-statements has been used. A simplified diagram of the code is shown in

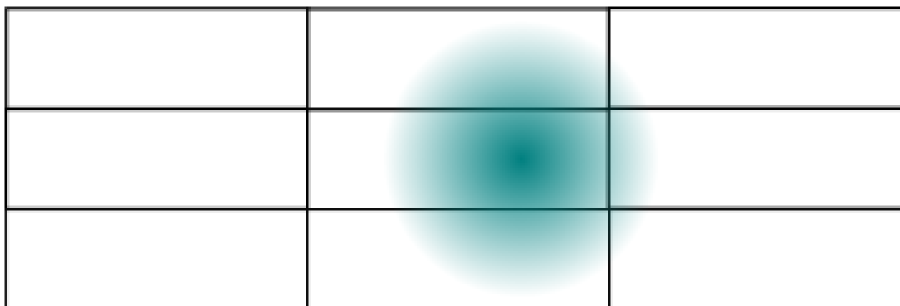

Figure 5.8: A simplified illustration of how the charge released results in a cluster of adjacent pixel. It is necessary to include bins adjacent to the one with the largest value of ToT.

figure 5.9.

In the first loop all the pixel hits from each event are looped over, first making sure that the right module identifier is in place, so that only one sensor is looked at each time. The pixel with highest ToT is found by replacing `maxTOT` with the ToT value of the pixel hit if this exceeds the existing `maxTOT`. The address of this pixel is also found.

In the next loop, all pixels with a hit in an event is looped over. Then the condition that a pixel hit must be within two pixel heights and lengths from the pixel with highest ToT to be counted as part of the cluster is set. When this condition is satisfied the ToT signal from this hit is added to the sum of cluster ToT. In addition there is added one to the number of pixel in the cluster, so that the output of this loop is the total ToT signal from a cluster and the number of pixels included in the cluster.

After these two loops, a requirement is made so that the tracks from the cluster must be within an area without any noisy or dead pixels (conditions: number of pixels in cluster must be larger than zero, `xTrack` must be within 7200 μm, the `dxTrack` between -0.4 and 0.3, `yTrack` must be between 1000 and 7200 μm and the `dyTrack` must be between -0.1 and 0.4. A condition is made so that absolute value of the `difx` is below 350 μm and `dify` below 75 μm to stay within two standard deviations of their distributions). If these conditions are satisfied a histogram is filled with the highest ToT value (Figure 5.10) and one with the sum of the cluster ToT signal (`clutot` shown in figure 5.11). Also histograms are filled with the difference between hits and tracks (`difx` and `dify` shown in figure 5.12), the number of pixel hit in one event(`nhits`) and the number of pixels included in a cluster (`ncluster`) shown in figure 5.13.

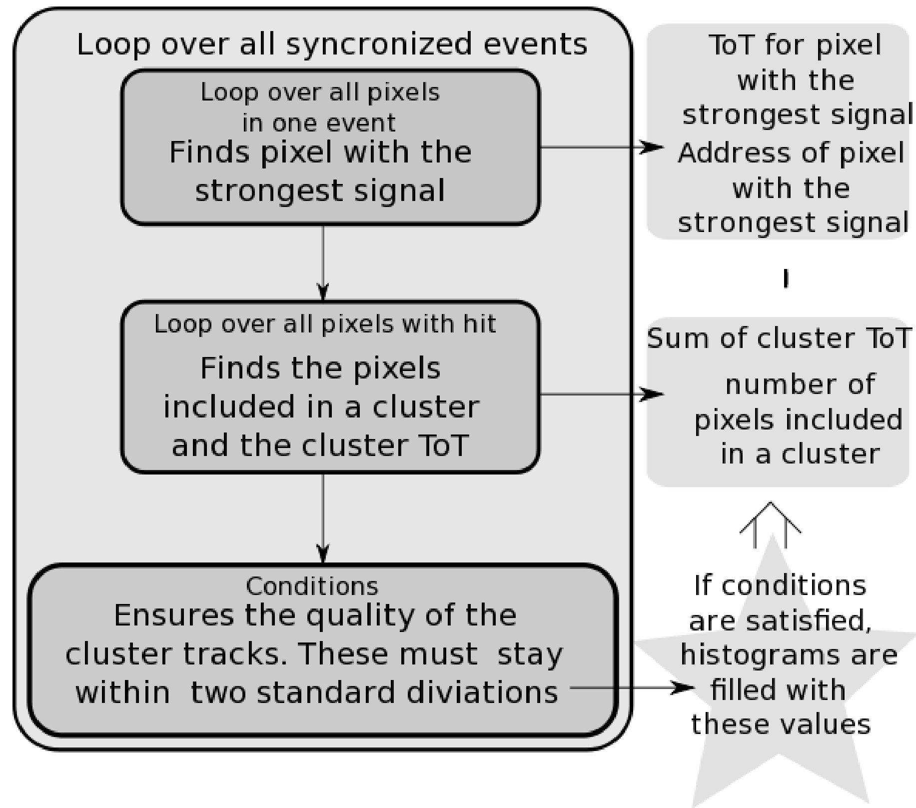

Figure 5.9: Simplified diagram of the code.

5.3.1 Time over threshold results

When comparing the mean values of figures 5.10 and 5.11 one sees that the mean value is slightly higher for the cluster ToT at 52.01, than for the mean of the highest ToT at 50.77. This is because the signals from the pixels in a cluster are added on top of each other. However the difference is not great, which indicates that in most cases most of the energy is deposited in the center pixel of a cluster.

In figure 5.12One can see that while `dify` has a relatively symmetrical distribution around 0, the `difx` distribution is more skewed. This skewness might be caused by a non-flat beam profile [17] shown in figure 5.1 In the `difx` plot, one can see the contours of the electrode holes. In this plot one can also see the contours of the edge electrode in the zeroth pixel, where the distribution goes below -200 μm.

In figure 5.13 one can see the distributions of how many pixels are hit in the detector, and how many pixels are included in a cluster. In both

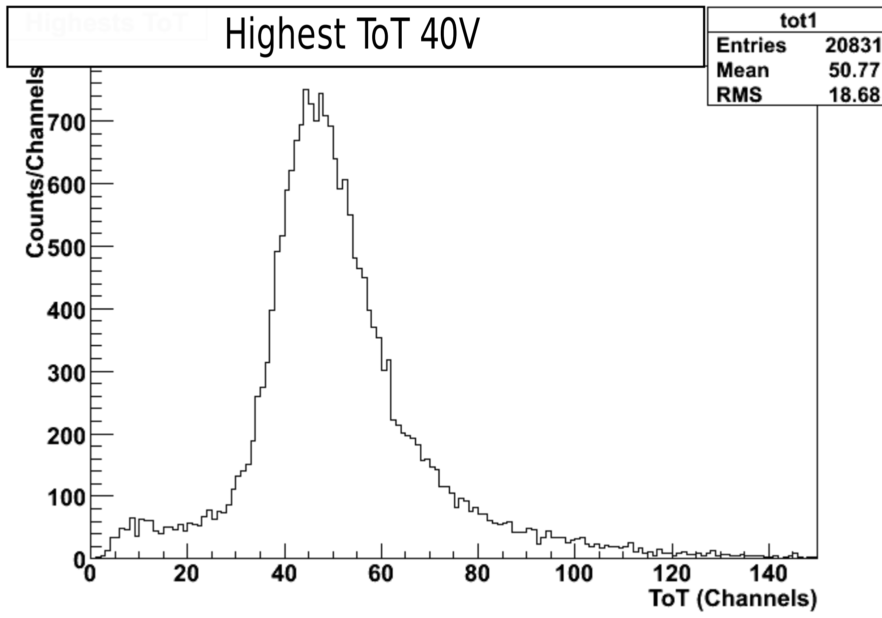

Figure 5.10: Distribution over largest ToT

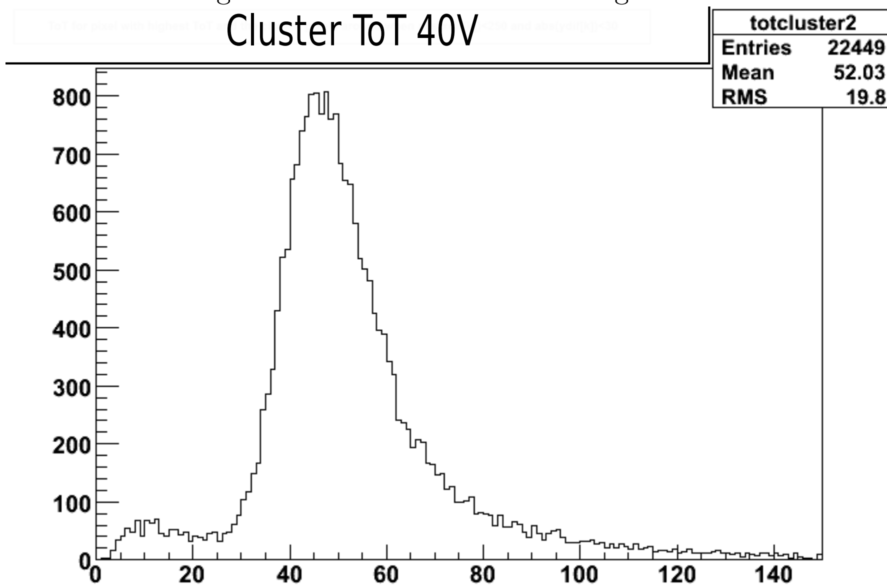

Figure 5.11: Distribution of the cluster ToT

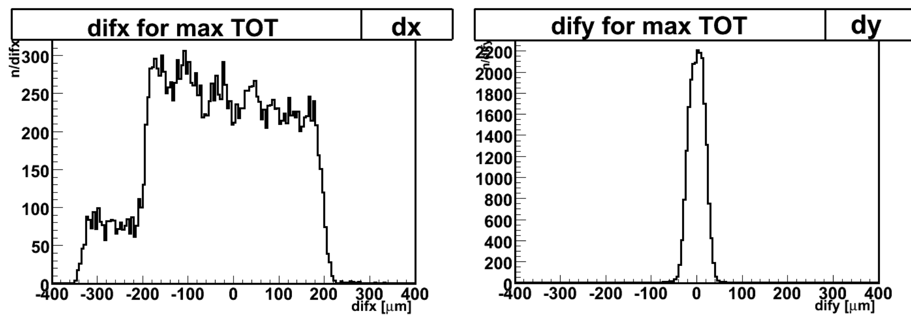

Figure 5.12: `difx` and `dify` distributions for the largest ToT [μm]. In the `difx` one can see the edge electrode in the area between -300 and -200 μm.

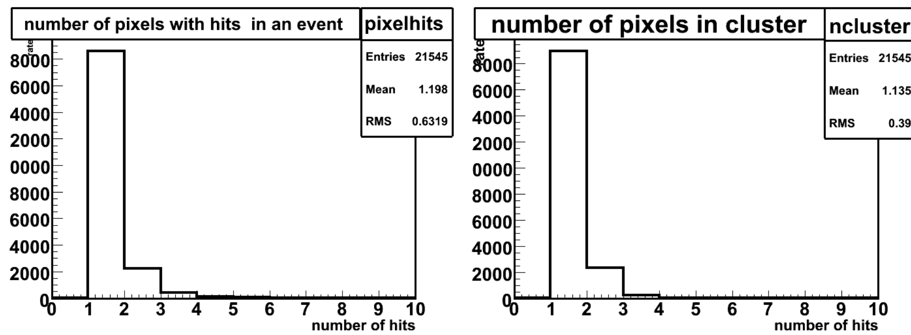

Figure 5.13: Distributions of number of pixel hits in the detector in each event and the number of pixel included in a cluster.

cases one can see that the majority of all signals are only from one pixel in an event, but one can also conclude by comparing these, that whenever the detector has several pixel hits in one event, these are mostly in a cluster.

After the histograms have been filled for all the events, the ToT plots are fitted with a Gauss-Landau convolution.First by a code and then manually. For the manual fitting, it was decided that the range of the fit should go from where the bin content is at its 1/3 of the maximum height to a ToT value of approximately 2 times the most probable value.The Gauss-Landau convolution was used as neither the Gaussian nor the Landau distribution could fully cover the shape of this intermediate distribution obtained, and as mentioned in subsection 2.1.3, the calculation of the distribution from an absorber of intermediate thickness and distinguishing parameter is too complex to tackle in this thesis. Figure 5.14 shows that the Gauss-Landau convolution is a good fit at 40V. The signal has the shape of a Landau distribution smeared by a Gaussian.

This procedure is done at various bias voltages, as shown in figure 5.15, 5.16, 5.17 and 5.18. The ToT distributions for bias voltage below 40V shows deviations from the Gauss-Landau distribution with a secondary peak. So far this peak remains to be explained.

The mean value and the most probable value for the maximum ToT and the cluster Tot are plotted as a function of bias voltage in section 5.7.

Evaluation of fits: The χ^2 test

For an unbiased evaluation of the goodness of fits one can use the χ^2 test. This gives a rough measurement of the agreement between an observed distribution of measured data, and the theoretical distribution one expects this to follow [37]

$$\chi^2 = \sum_{k=1}^{n} \frac{(O_k - E_k)^2}{E_k}, \tag{5.1}$$

where O_k is the number of observations that falls into each bin k, and E_k is the expected number of entries in bin k. The number of degrees of freedom is n minus the number of parameters in the model (in this case: four). χ^2 over the number of degrees of freedom should not be too small. $F(\chi^2)$ is the function of how one expects the χ^2 divided by the number of degrees of freedom to be distributed across values of χ^2 when a model is correct. $P(\chi_0^2)$ is the integral of $F(\chi^2)$ between $-\infty$ and the observed χ_0^2 and when this lies between 0,1 and 0,9, the agreement between the distributions is satisfactory.

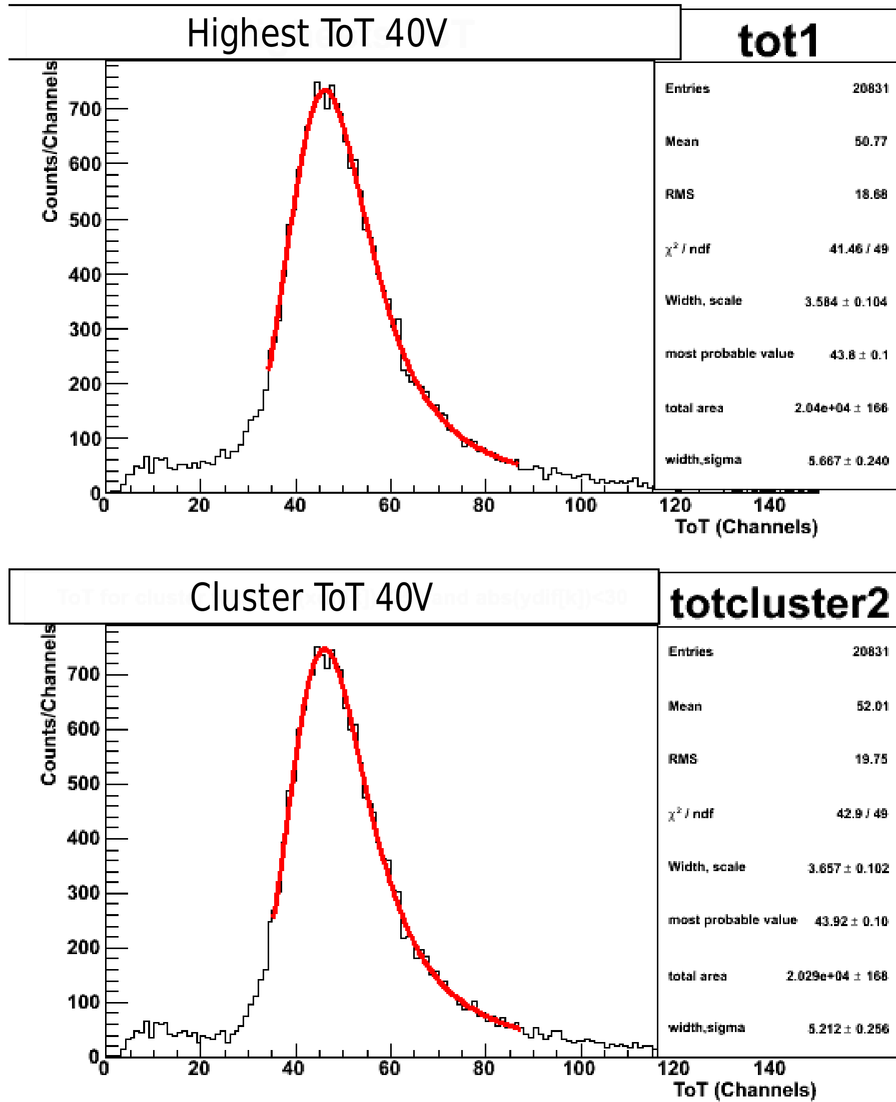

Figure 5.14: Gauss-Landau convolution fitting of top: Largest Time over Threshold (ToT), bottom: cluster ToT (ie:ToT for the pixel with largest ToT and its closest surrounding pixels at 40V).The fitted curve agrees well with the measured data.

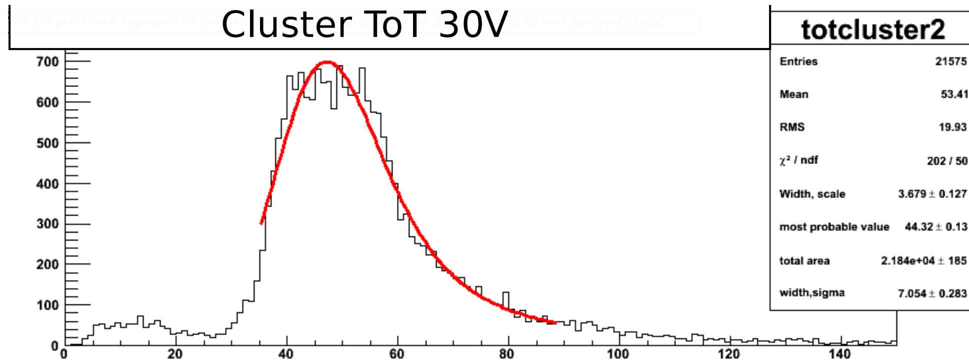

Figure 5.15: Gauss-Landau convolution at 30V: The most probable value is 44.32 ±0.13 with a χ^2 over the number of degrees of freedom of 202/50.

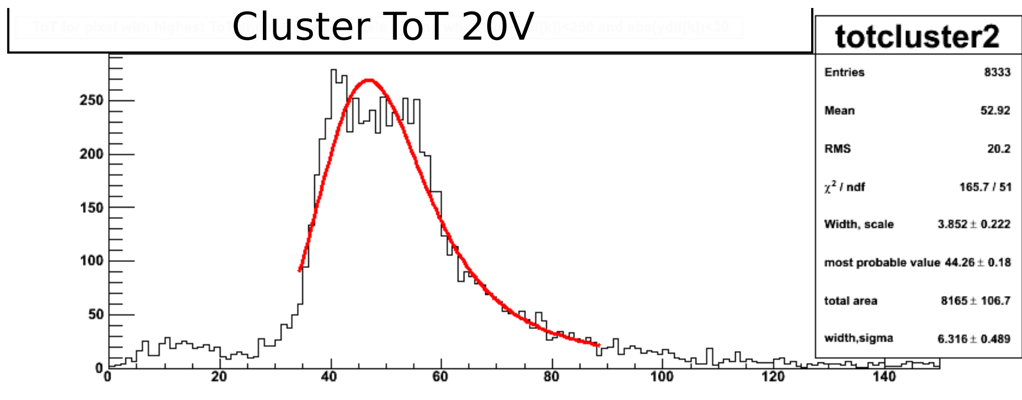

Figure 5.16: Gauss-Landau convolution at 20V: The most probable value is 44.26 ±0.18 with a χ^2 over the number of degrees of freedom of 165.7/51.

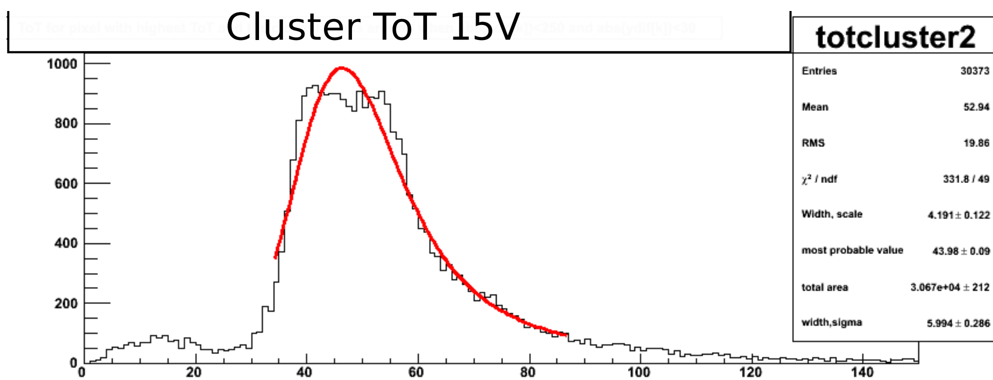

Figure 5.17: Gauss-Landau convolution at 15V: The most probable value is 43.98 ±0.09 with a χ^2 over the number of degrees of freedom of 331.8/49.

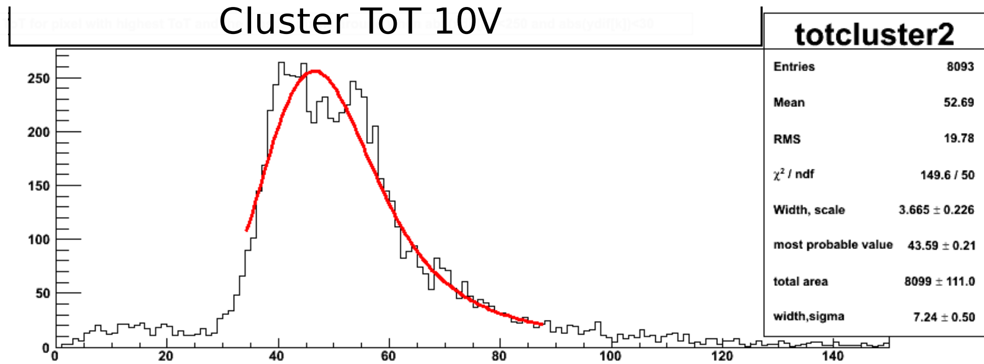

Figure 5.18: Gauss-Landau convolution at 10V: The most probable value is 43.59 $\pm$0.21 with a χ^2 over the number of degrees of freedom of 149.6/50.

5.4 Efficiency

To study the intrinsic efficiency of the detector, the ratio between the number of tracks that pass through the detector and the number of tracks with hits in the detector was calculated.

Some cuts and conditions are made for plotting the profiles. For the `xTrack` profile, the condition is for the same track in y direction to be within a good detector area where the `dyTrack` is minimal (if 3000 μm`<yTrack` <7800 μm and -0.1< `dyTrack` <0.4:) The same condition was made for the `xTracks` when plotting the `yTrack` profile (0μm< `xTrack` <2000μm and -0.4< `dxTrack` <0.3). For the two dimensionally plotting, the same conditions are made in both directions at the same time (`-0.4<dxTrack<0.3 and -0.1<dyTrack<0.4 and abs(ydif[k])<75`μm `and abs(xdif[k])<350`μm. These profiles are shown in figures 5.19 and 5.22.

To find out which tracks has hits registered by the detector, the same conditions as above has been used, but with the extra condition of a hit in the pixel in which the track is projected, and also conditions of abs(`ydif[k]`)< 75μm and abs(`xdif[k]`)< 350 μm for the x and y profiles. (Figure 5.20 and Figure 5.23).

Then the efficiency plots are made by dividing the histograms containing tracks with hit (histogram a) on the histograms containing tracks in detector area(histogram b). By this the content of each bin in histogram a is divided on the content of the respective bin in histogram b (Figure 5.21, Figure 5.24 and Figure 5.25).

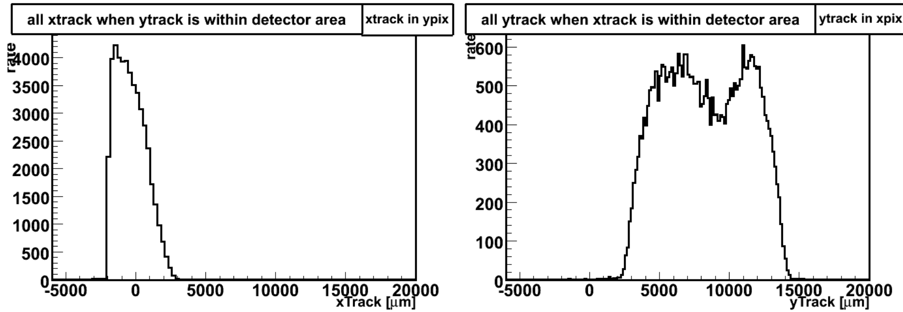

Figure 5.19: Beam x- and y-profile as it is they are projected in the beam telescope, with cuts made in the y-tracks for the x-profile, and cuts made to the x-tracks in the y-profile

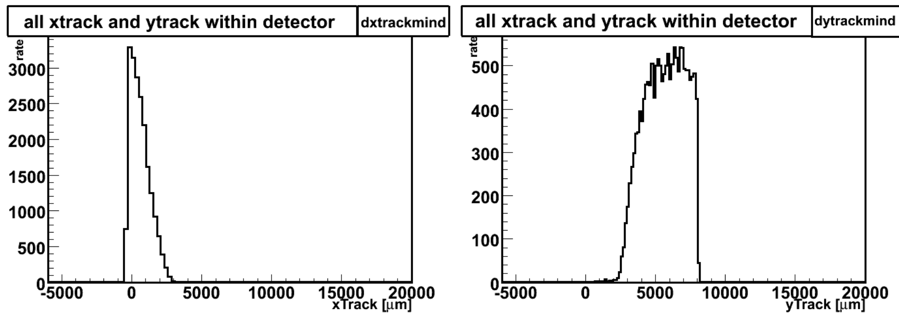

Figure 5.20: Profiles of xtracks and ytracks that have hit in the detector.

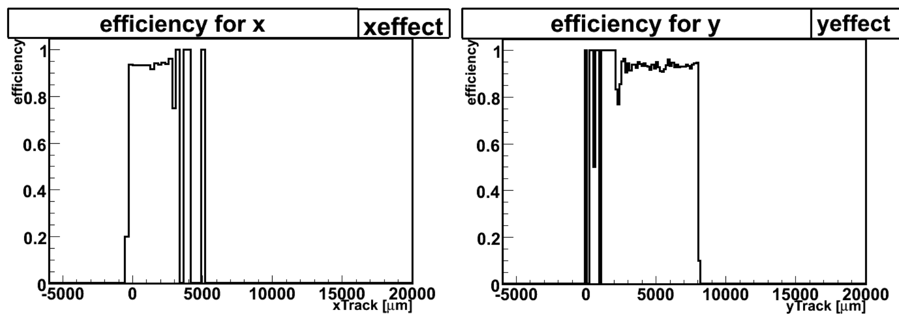

Figure 5.21: Intrinsic efficiency of the sensor: registered events divided on real number of events

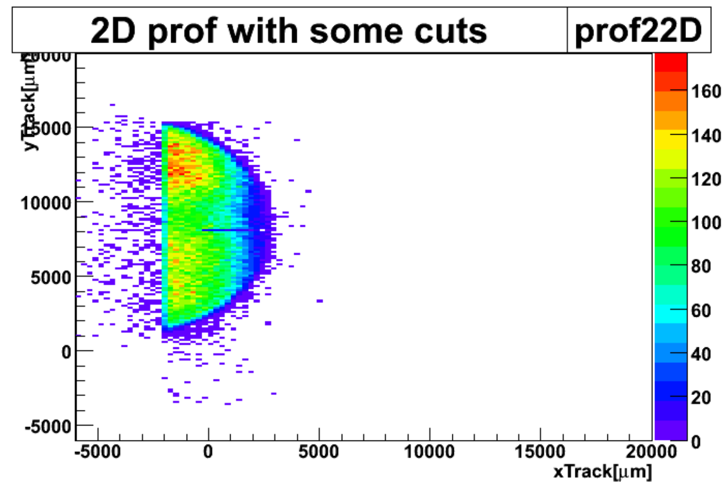

Figure 5.22: Beam profile as it is projected in the beam telescope, with conditions made to `dxTrack`, `dyTrack`, `difx` and `dify`

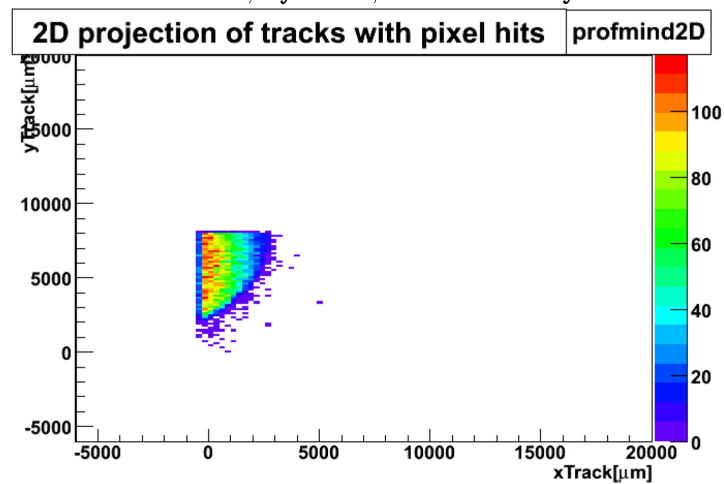

Figure 5.23: Tracks with hit in the detector

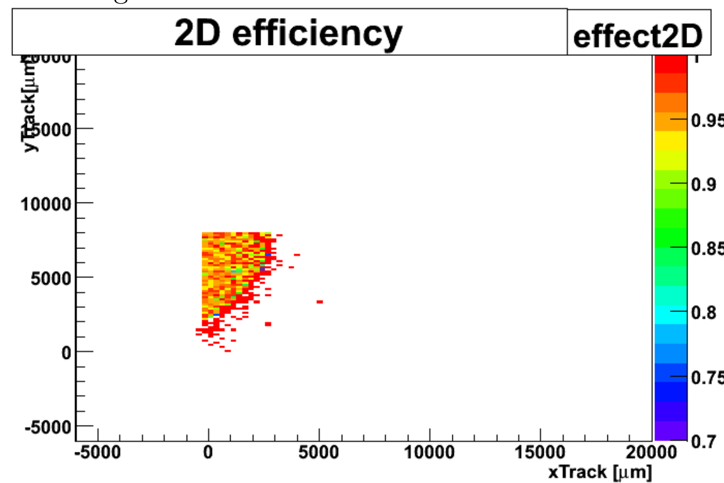

Figure 5.24: Intrinsic efficiency of the sensor: registered events divided by real number of events. Note that the color scale range from 0.7 to 1 and represents the efficiency.

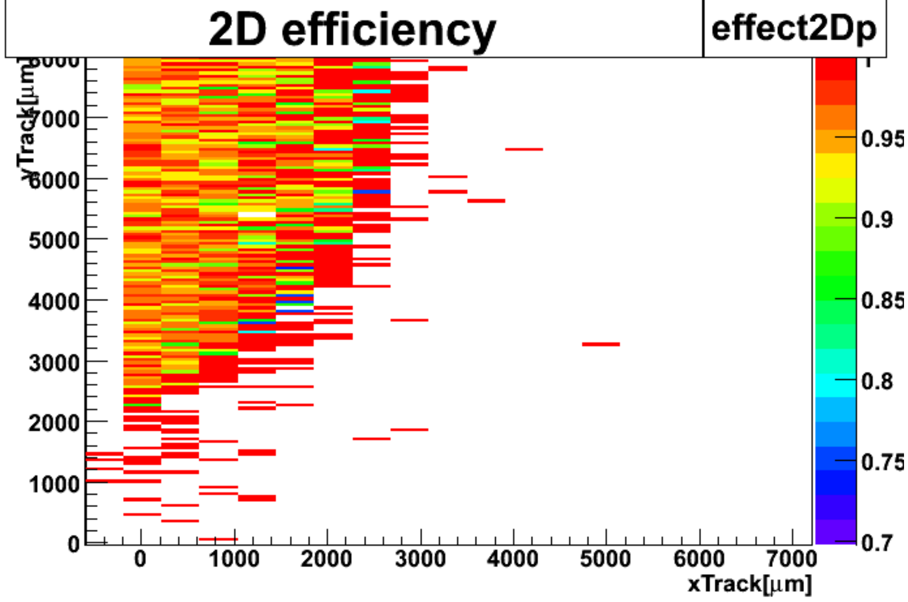

Figure 5.25: Close up of the intrinsic efficiency of the sensor: registered events divided on real number of events. Note that the color scale range from 0.7 to 1. The efficiency mainly ranges between 0.9 to 1

The binomial distribution is used to calculate and plot the errors [38]. If one call the number of tracks passing through the detector N which represents the number of trials, and the number of tracks with hits n, representing number of successes, then the probability $p = n/N$ must equal the efficiency ε. The efficiency with error is then given by

$$\varepsilon = \frac{n}{N} \pm \sigma_{\varepsilon}\,, \tag{5.2}$$

where the error is

$$\sigma_{\varepsilon} = \frac{1}{N}\sigma_{n} = \frac{1}{N}\sqrt{N\varepsilon(1-\varepsilon)}. \tag{5.3}$$

5.5 Study of the "active edge"

Because this type of detector is supposed to have sensitivity all the way to the outer edge, a study of the efficiency in the zeroth pixel was carried out.

Like in the efficiency study above, one denominator histogram (figure 5.26) was filled with xtracks that had the conditions (3000 μm<`yTrack` <7800μm and -0.1<`dyTrack`<0.4).

Then the numerator histogram is filled with the same conditions as the previous, but with the additional condition of having hit in the 0th pixel

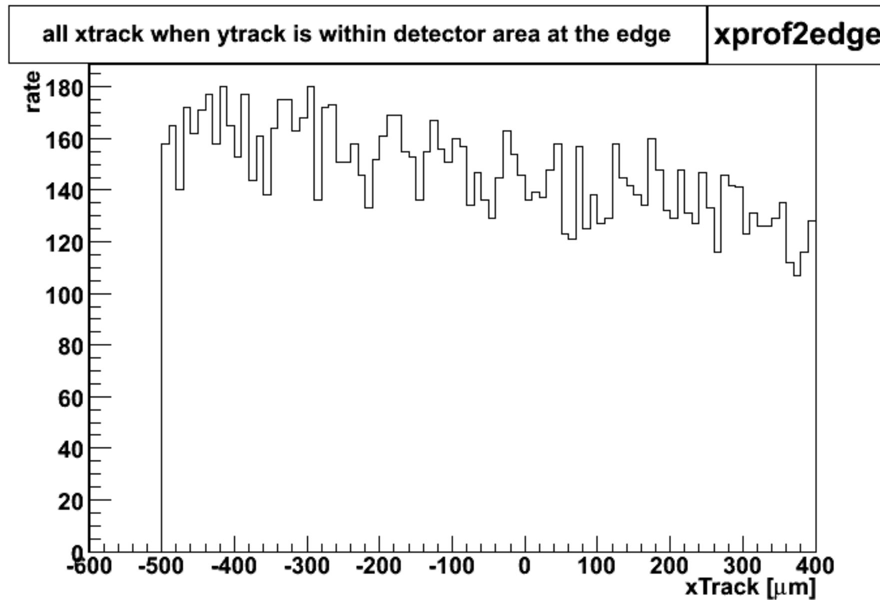

Figure 5.26: Beam profile as it is projected in the beam telescope, without any cuts

only (figure 5.27).

The efficiency in the 0th pixel is then found by dividing these histograms. Figure 5.28 shows the efficiency in the 0th pixel with binomial errors and a box fitting. One can see that the 0th pixel shows a high efficiency all the way out to approximately -350 μm, which is 150 μm outside the normal boundary of the zeroth pixel. This is the area of the edge electrode.

5.5.1 Box-convolution of the efficiency in the edge pixel

The efficiency in the zeroth pixel was then fitted with a box-plot seen in figure 5.29in a separate routine to find the resolution of the sensor. from the plot one can read out the results from the fit. The height of the box gives an efficiency of 97.424 $\pm$ 0.002 %, which is a bit higher than the real efficiency of approximately 95 %. This is due to the nature of the box-fitting and the binomial error-bars in the efficiency plot.

Sigma is a convolution between the resolution of the individual track and the spread in charge deposition. The left sigma is the resolution at the edge, while the right sigma is the resolution of the boarder to the next pixel. The left side has the resolution of 9.6 $\pm$0.7 μm, while the right side has a resolution of 9.9 $\pm$0.6 μm. This is consistent with the results presented in

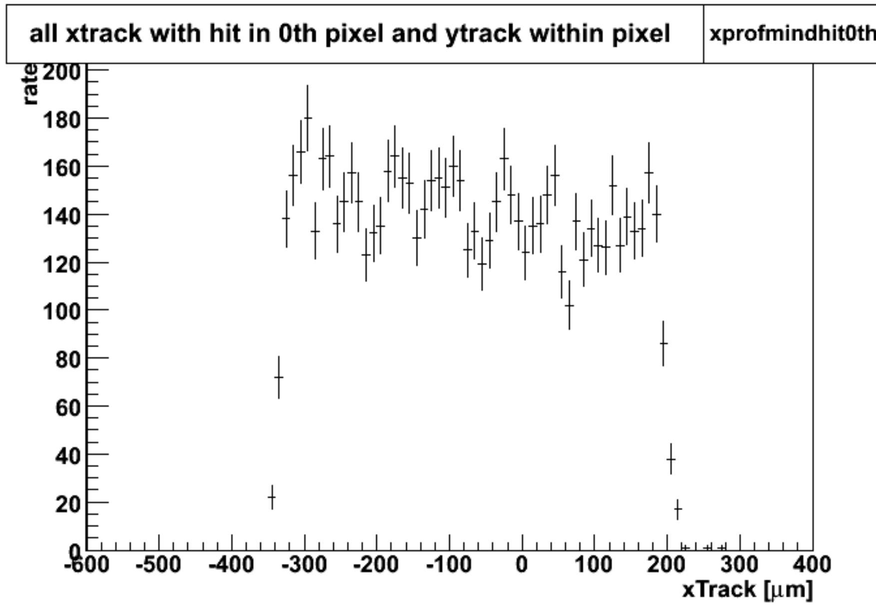

Figure 5.27: Positions of `xTrack`s with hit in the zeroth pixel.

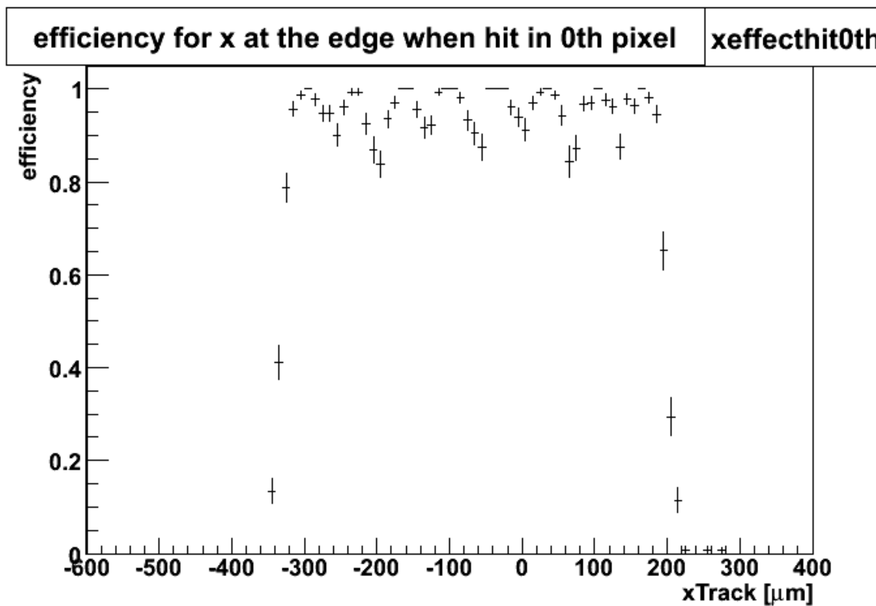

Figure 5.28: edge efficiency of the sensor: registered events divided on real number of events shows good efficiency all the way to the sensor edge

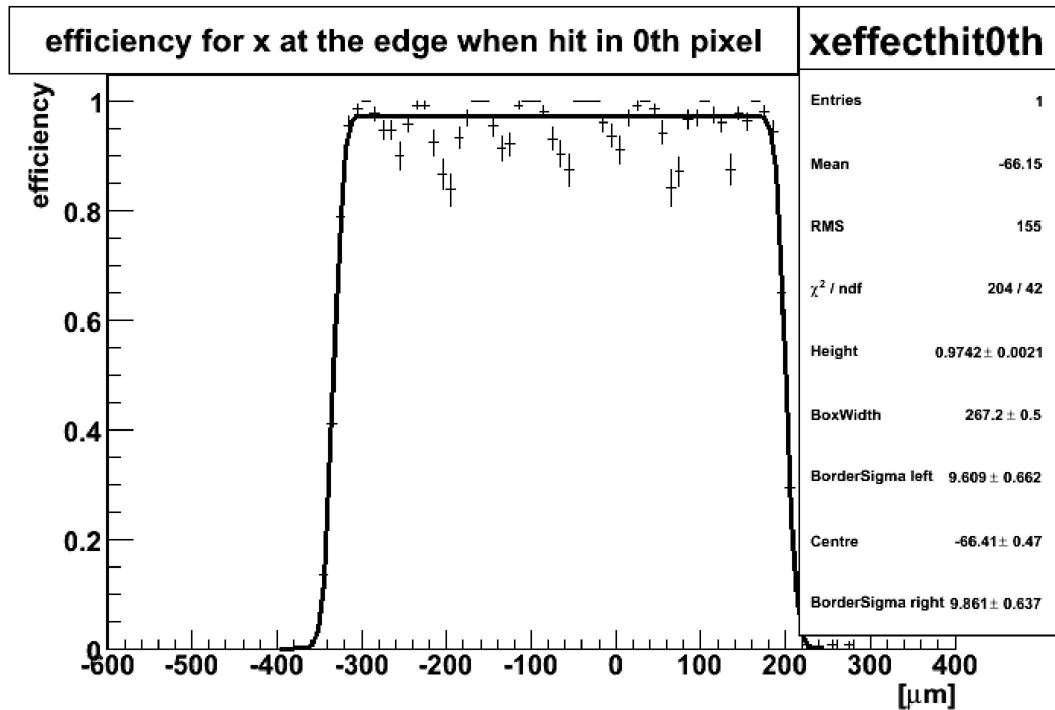

Figure 5.29: Box convolution of the efficiency in the zeroth pixel with resulting values from the fit: Height gives the efficiency of the pixel, Box width gives half of the total pixel width, while Centre refers to the location of the pixel centre along the x-axis. Left and right sigma is a convolution between the resolution of the individual track and the spread in charge deposition at either side of the pixel. The left side has the resolution of 9.6 ± 0.7 μm, while the right side has a resolution of 9.9 ± 0.6 μm. The χ^2 divided by the number of degrees of freedom is not so good due to the electrode holes that the fit does not cover.

the article [17]. They have also obtained a track-resolution with an upper limit of about 11 μm with data from other runs taken at the same test beam. An earlier characterization made by M. Mathes et.al [15] , using essentially the same instruments, obtained a much better resolution of 5-6 μm. This can partly be because this setup contained one extra tracking plane, but can also result from misalignments in the present track reconstruction.

A box convolution of the efficiency in the pixel next to the zeroth pixel is presented in 5.30. The box height is slightly higher in this pixel than in the zeroth pixel. It is, however, possible to claim that the efficiency is just as good at the edge as for the rest of the detector. On the right side of this pixel, a resolution as good as 8.0 ± 0.7 μm is obtained.

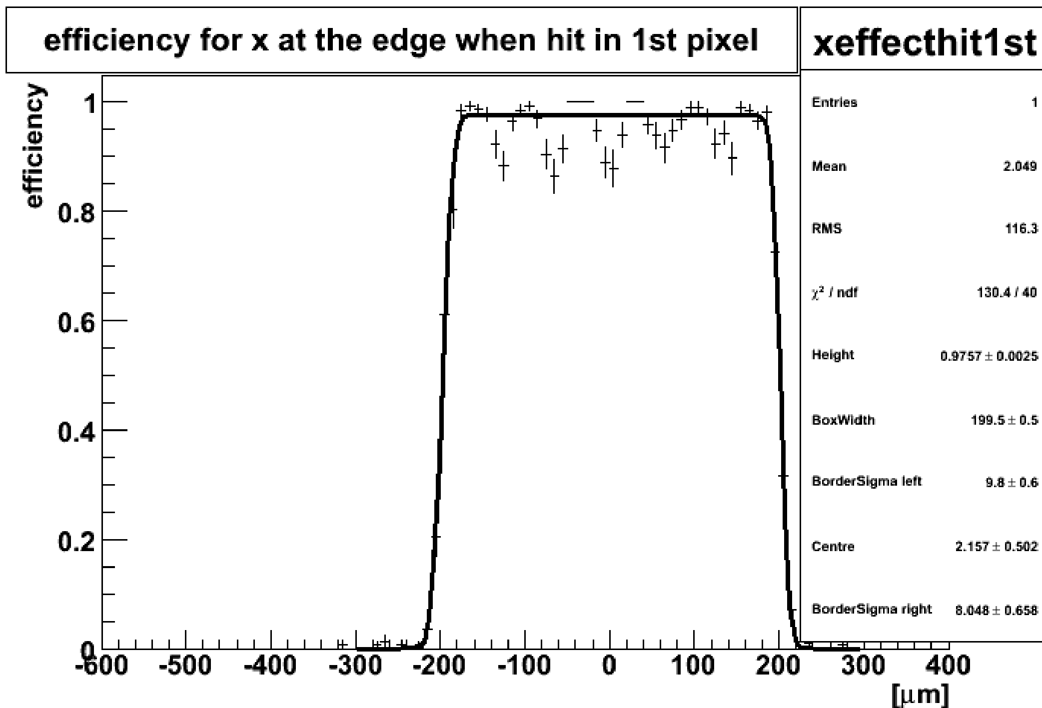

Figure 5.30: Box convolution of the efficiency in the first pixel with the results from the fit. Height gives the efficiency of the pixel, Boxwidth gives half of the total pixel width, while Centre refers to the location of the pixel centre along the x-axis. Left and right sigma is a convolution between the resolution of the individual tracks and the spread in charge deposition at either side of the pixel. From this table, one can see that the left side has a sigma of 9.8 ± 0.6 μm, while the right side sigma is as low as 8.0 ± 0.7 μm.

5.6 Study of the loss of detection efficiency in volume occupied by the electrode cylinders

A study of the efficiency in a pixel has been plotted on a detailed level to illustrate the non-homogeneity of the sensor. To gather sufficient statistics to see the detector holes, information on efficiency for all the pixels has been added on top of each other with the conditions: `xTrack` $<7200\mu m$ and -0.4$<$ `dxTrack` <0.3 and $1000\mu m<$ `yTrack` $< 7950\mu m$ and $-0.1 <$ `dyTrack` < 0.4 . A two-dimensional histogram is filled with the track position of the track minus the combined size of the numbers of whole pixels from (0,0), which in other words move the position of tracks in all pixels into just one pixel by subtracting the product of pixel size and the pixel number from the track position.

The numerator histogram is filled in the same way, but with the condition of having hits. This is then divided by the previous histogram.Figure 5.31 shows the result. Here one can clearly see the three electrodes in the centre (3E-G has its name from the three electrodes in each pixel. One can also see the contours of the electrodes that give rise to the additional holes in figure 5.5).

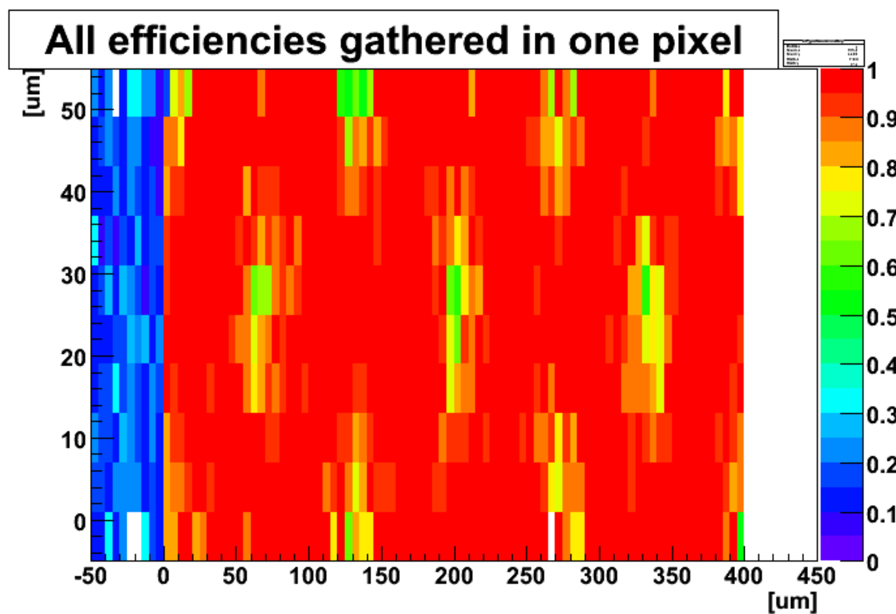

Figure 5.31: Detailed plot of the efficiency of track detection in one pixel.Red is 100% efficiency, while green is 50% efficiency. The green spots in the plot shows the efficiency loss in the electrode volumes.

5.7 Efficiency and ToT as function of bias voltage

As mentioned in section 5.3.1, the Most probable value of the maximum ToT and cluster ToT was plotted as a function of bias voltage. This was done to investigate whether the sensor's performance and signal would increase with the voltage. However, when studying the most probable value and the mean value of the ToT between 10 and 40 volts in figures 5.32 and 5.33, one could only see very small fluctuations in channel numbers. This indicates that after 10 volts, there is no increase in signal to be gained from increasing the voltage. This is consistent with the fabricators prediction of fully efficientness after 10V.

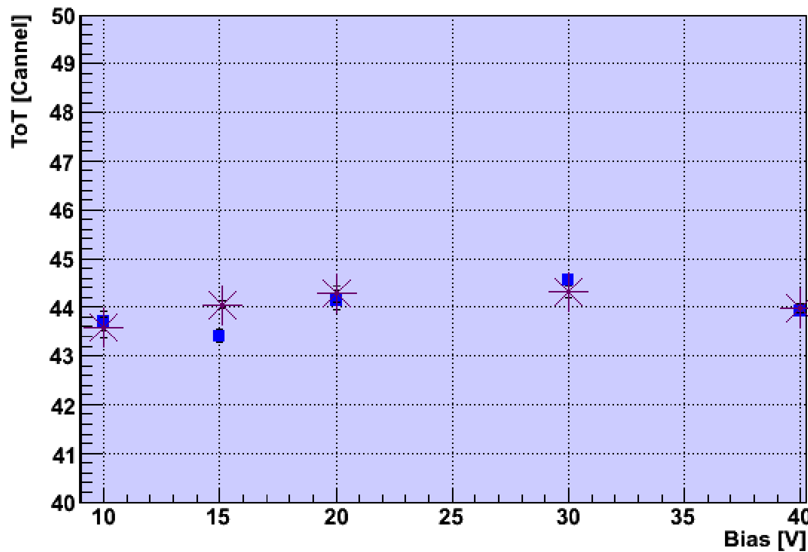

Figure 5.32: The Most Probable Value of ToT plotted as a function of Bias voltage for the 3E-G chip. The star markers represents the signal from the cluster, while the square markers represents the ToT from the pixel with the strongest signal. The size of the error bars lies between 0.1 and 0.2, and are thus barely visible in this scale.

The efficiency, which has been plotted as a function of bias voltage in figure 5.34, is found by counting the number of tracks passing through an area of a box where xTrack lies between 0 and 2000 μm and yTrack between 3000 and 7800 μm, and then also counting the number of tracks passing through this box that has a hit. The errors are found by applying the formula for binomial uncertainties. The plot shows that the efficiency does not increase as a function of bias voltage after 10V.

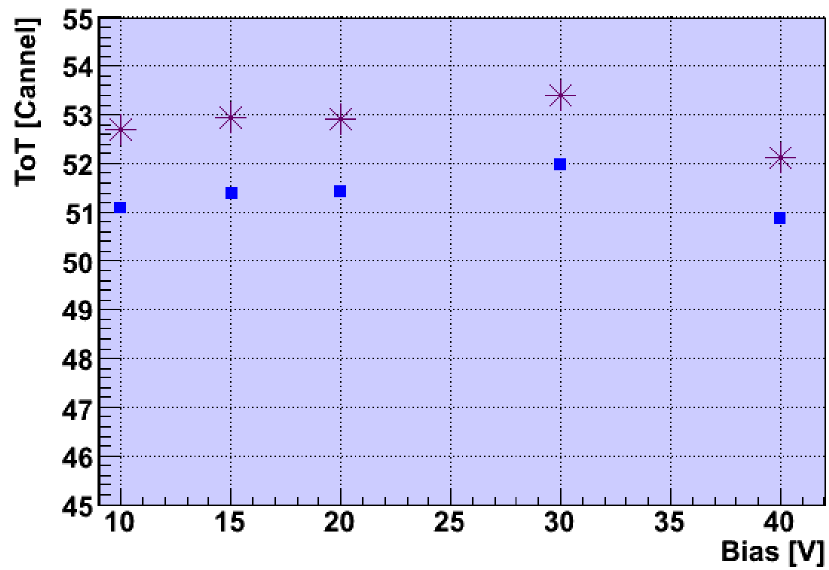

Figure 5.33: The mean of ToT plotted as a function of Bias voltage for the 3E-G chip. The star markers represents the signal from the cluster, while the square markers represents the ToT from the pixel with the strongest signal. This plot does not include errors, and only shows the the tendencies of the mean ToT.

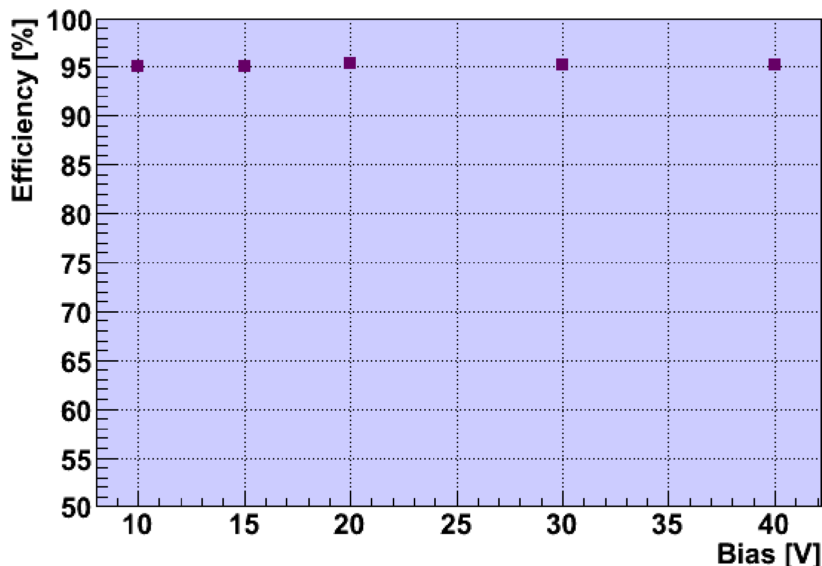

Figure 5.34: Intrinsic efficiency as a function of bias voltage. The efficiency does not vary with the voltage after 10 V. The error bars have sizes between 0.1 and 0.3 , and are thus to small to show in this scale.

The efficiency was calculated with some additional conditions, and the results are found in table 5.3.

5.7.1 Analysis of the 4E-C sensor

Some of the analysis code made for the 3E-G sensor was also applied to data of the 4E-C sensor. Although track information is provided by the beam telescope, there are two sets of track information for each run, one for each sensor. This is because each set of track coordinates are adjusted to have point (0, 0) in the center of the zeroth pixel. Figure 5.35 shows how the beam intercepts the 4E-C sensor slightly lower than the 3E-C sensor does. However, the same cuts and conditions were made to the tracks for the 4E-C sensor as for the 3E-G sensor.

The `dxTrack` and `dyTrack` distributions shown in figure 5.36 were quite unexpected, as the distributions were not limited to a narrow distribution around 0, but had an extra distribution or tail around -1 for `dxTrack` and around 1 for `dyTrack` . When conditions were made for the `dxTrack` and `dyTrack` during the analysis code as for the 3E-G sensor, these tails were cut away. To check how these strange `dxTrack` and `dyTrack` distributions affected the efficiency, the efficiency was calculated as previously, but under

Efficiency [%] for the 3E-G sensor	10V	15V	20V	30V	40V
e1 :	95.0 ± 0.3	95.1 ± 0.2	95.3 ± 0.2	95.2 ± 0.1	95.3 ± 0.2
e2 :	92.0 ± 0.3	92.3 ± 0.2	93.1 ± 0.2	92.4 ± 0.2	92.5 ± 0.2
e3 :	95.4 ± 0.3	95.24 ± 0.2	95.3 ± 0.3	95.4 ± 0.2	95.33 ± 0.2
e4 :	93.3 ± 0.3	93.3 ± 0.2	93.5 ± 0.3	93.2 ± 0.2	93.4 ± 0.2

Table 5.3: Table of efficiencies for the 3E-G sensor with various conditions: **e1** has only conditions of xTrack between 0 and 2000 μm and yTrack between 3000 and 7800 μm, **e2** has conditions as for e1, but with additional condition of difx and dify within 2SD for the denominator **e3** has the same conditions as e1, but with dxTrack and dyTrack within two SD and **e4** has the same conditions as e2, but with dxTrack and dyTrack within two SD

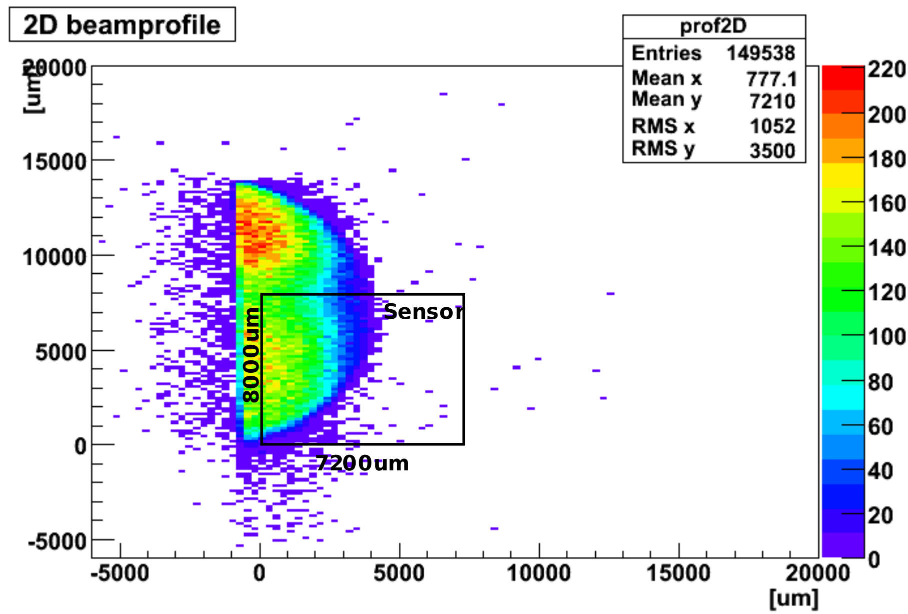

Figure 5.35: The 4E-C sensor intercepted by the beam. More of the 4E-C sensor is intercepted by the beam than the 3E-G sensor.

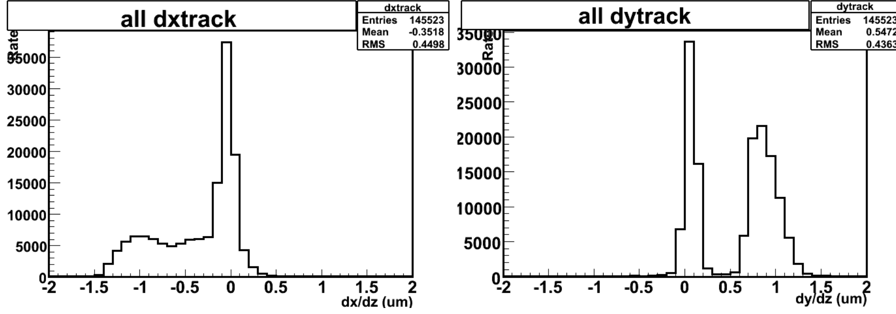

Figure 5.36: dxTrack and dyTrack distribution of the beam for the 4E-C sensor.

Efficiency [%] for 4E-S sensor	10V	15V	20V	30V
e1 :	93.8 ± 0.3	90.5 ± 0.2	93.8 ± 0.3	93.6 ± 0.1
e2 :	90.4 ± 0.3	87.8 ± 0.2	91.2 ± 0.3	90.6 ± 0.2
e3 :	93.9 ± 0.3	90.5 ± 0.2	93.8 ± 0.3	93.6 ± 0.2
e4 :	91.9 ± 0.3	88.8 ± 0.2	91.6 ± 0.3	91.7 ± 0.3

Table 5.4: Table of efficiencies of the 4E-C sensor with various conditions: **e1** has only conditions of xTrack between 0 and 2000 μm and yTrack between 3000 and 7800 μm, **e2** has conditions as for e1, but with additional condition of difx and dify within 2SD for the denominator **e3** has the same conditions as e1, but with dxTrack and dyTrack within two SD and **e4** has the same conditions as e2, but with dxTrack and dyTrack within two SD

various conditions. The results are found in table 5.7.1. By comparing the efficiency without conditions made to dxTrack and dyTrack, e1, to the efficiency with conditions e3, it seemed that the cuts made little difference to the efficiency. This could indicate that the importance of restricting dxTrack and dyTrack had been overrated previously in the analysis.

The ToT sizes and efficiencies without conditions to dxTrack, dyTrack, difx or dify were plotted as a function of bias voltage.

Figure 5.37 shows the intrinsic efficiency of the sensor as a function of the Bias voltage, One can see that the efficiencies lies a bit lower for the sensor with four electrodes compared to the sensor with only three electrodes due to efficiency loss in the electrode volume as shown in figure 5.38, but this is less than 4%.

Figures 5.39 to 5.42 shows the distribution of the cluster ToT for the 4E-C sensor. The Gauss-Landau convolution makes a better fit for the ToT

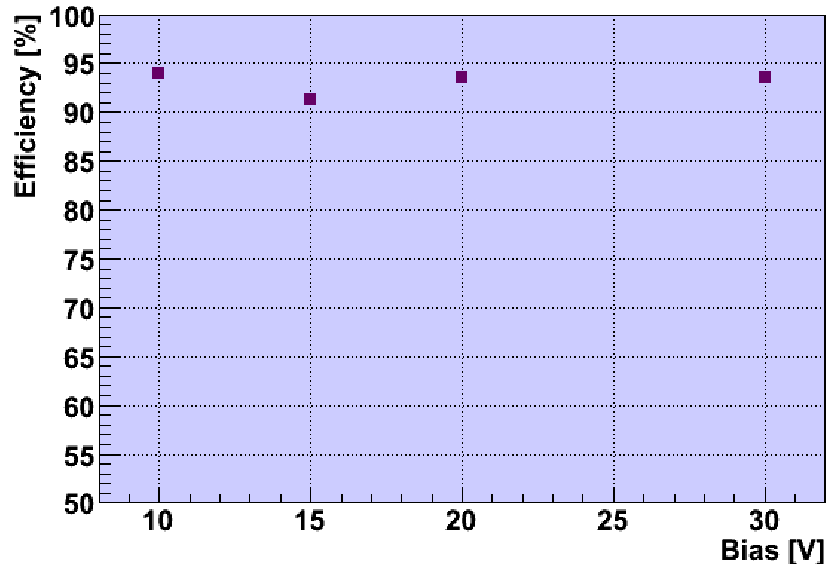

Figure 5.37: Intrinsic efficiency as a function of bias voltage for the 4E-C sensor.

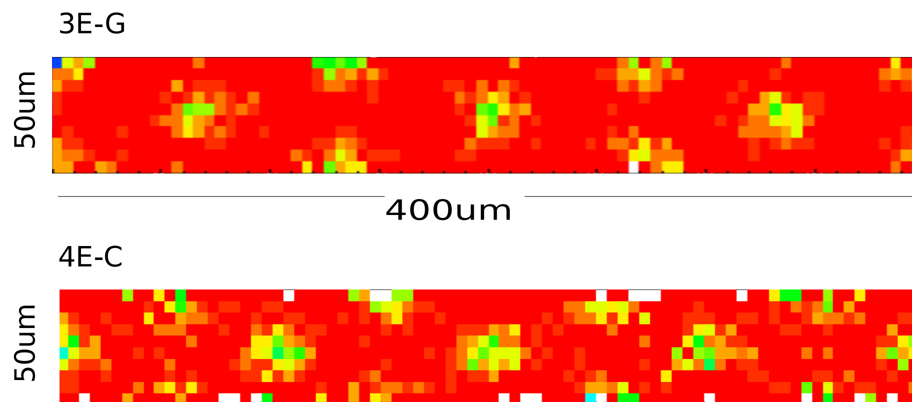

Figure 5.38: Efficiency map in a single pixel of $400\mu m\times$ $50\mu m$ for the 3E-G sensor and the 4E-C sensor. This shows how the electrodes of the 4E-C sensor is closer packed together than of the 3E-G sensor, making the efficiency of a pixel area slightly lower.

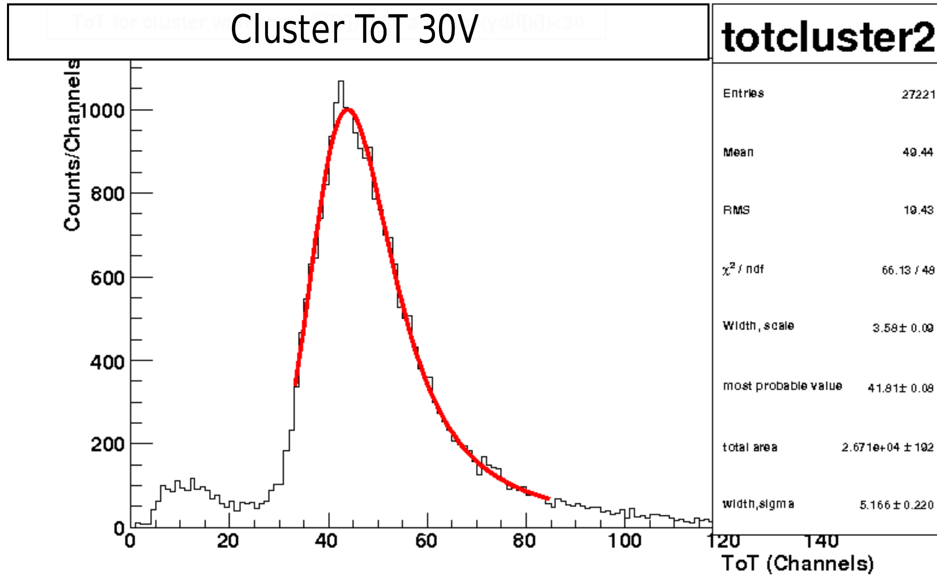

Figure 5.39: The distributions of cluster ToT at 30V for the 4E-C sensor .

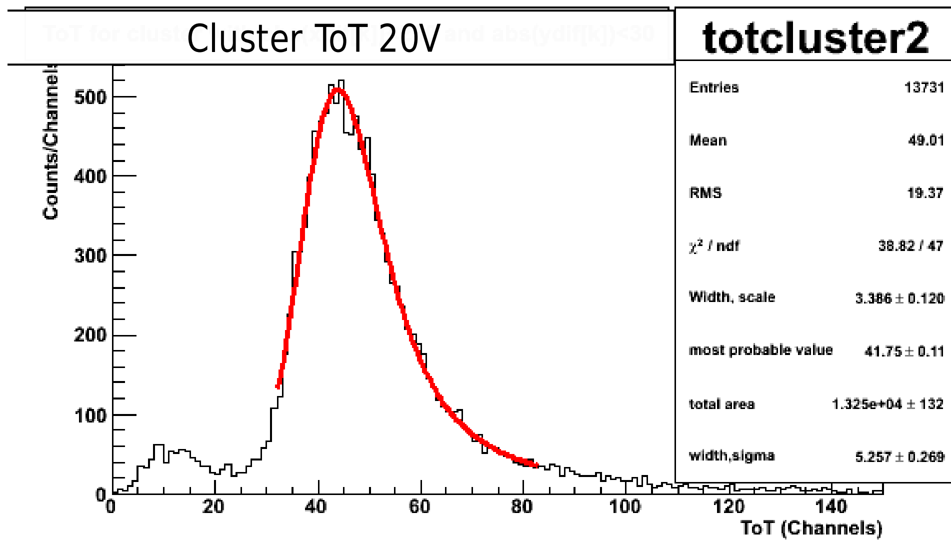

Figure 5.40: The distributions of cluster ToT at 20V for the 4E-C sensor .

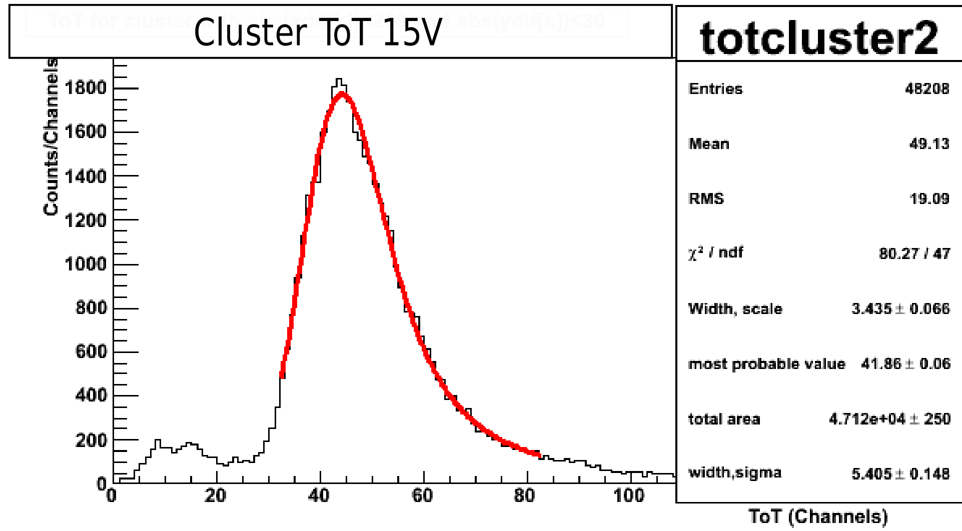

Figure 5.41: The distributions of cluster ToT at 15V for the 4E-C sensor .

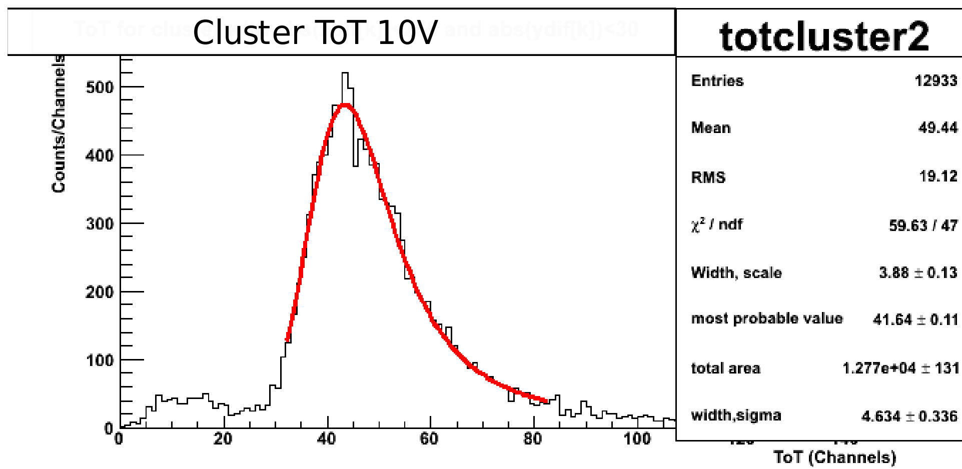

Figure 5.42: The distributions of cluster ToT at 10V for the 4E-C sensor .

distributions for this sensor than for the 3E-G sensor, as it does not have the same plateau around the most probable value.

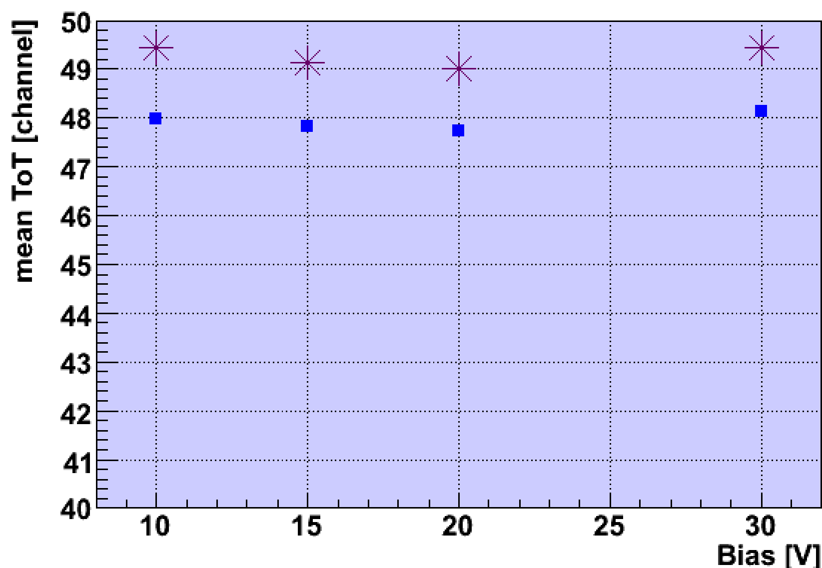

Figure 5.43: The mean ToT as a function of bias voltage for the irradiated detector. The star markers represent the clusterToT while the square markers represent ToT from the pixel with the strongest signal.

In figure 5.43 and figure 5.44 one can see that also the ToT-values lies a bit lower than for the 3E-G sensor.

5.8 Summary of the analysis

An alignment study of the data was performed at an early stage of the analysis. This showed an improvement from earlier alignments studied by Bjarne Stugu and Ahmed Abdelsalam . A small negative drift was observed as a function of run number, however, the alignment can be claimed to be good as it is better than 3 μm.

The ToT was studied as a function of bias voltage. The ToT distributions for the 3E-G sensor at bias voltage below 40V shows deviations from the Gauss-Landau distribution. This has not been observed for the 4E-C sensor.

ToT was observed to be stable between 10V and 40V for the 3E-G sensor(10V and 30V for 4E-C). The ToT was a bit lower for the 4E-C sensor compared to the 3E-G sensor. This can be due to differences in calibration

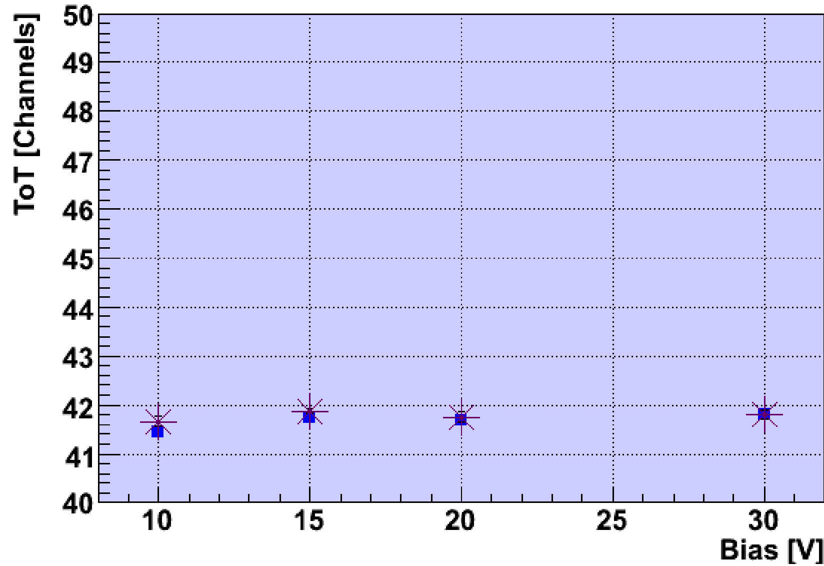

Figure 5.44: The Most Probable Value of ToT plotted as a function of Bias voltage for the 4E-C detector. The star markers represent the signal from the cluster, while the square markers represent the ToT from the pixel with the strongest signal

for the two sensors or sensor thickness. It may also be because the four electrode sensor has less active material because of more volume occupied by electrodes.

The efficiency was also studied as a function of bias voltage. It was found to lay around 95 % for the 3E-G sensor at all the voltages between 10V and 40V. For the 4E-C sensor, the efficiency was a bit lower due to more electrodes with efficiency loss.

Both the study of ToT an Efficiency as a function of bias voltage shows that the sensor is completely functional at 10V, which is a relatively low voltage.

The "active edge" pixel was found to have full efficiency all the way to the outer edge as expected and with a resolution of 9.9$\pm$ 0.6 μm, compatible with the resolution of the tracker.

The data from the 4E-C sensor showed some strange distributions of `dxTrack` and `dyTrack`, however, this did not seem to affect the efficiency.

In the sensors area occupied by the electrodes, a significantly energy loss was observed. Due to the small diameter of the electrodes, this did however not decrease the sensor efficiency significantly as was shown in the study of efficiency as a function of bias voltage.

Chapter 6

Test and calibrations of Silicon 3D detectors in Bergen

6.1 Motivation for a test set up in Bergen

When new technology has been developed it is very interesting to explore the possibilities of expanding the application area of this technology outside of the purpose of the original design. This also applies to the 3D silicon sensor. Now several areas of application are under investigation around the world, and among these are 3D for medical imaging. The structural molecular biology community will take advantage of 3D detectors to study protein folding, while research is ongoing to apply this technology to X-ray mammography [39].

At The Department of Physic and Technology at the University of Bergen, a new laboratory was opened in 2008 with the purpose of detector development. In this laboratory bridges are built between the high energy particle experiments and the medical physics. This laboratory should, therefore, make a perfect foundation for investigating the possibilities of medical application of the 3D silicon sensor while these are being considered for the ATLAS upgrade.

One goal is to develop and build a test bench for measuring various radioactive sources with the 3D sensors and approach the possibilities of their use within medical imaging.

Before even thinking about building a whole test bench, it is necessary to get the readout of the sensor in place.(One would think that making the readout work for one single sensor would be fairly trivial, however this has,

unfortunately, not been the case.) There are both electronics and software specifically developed for testing and calibration of ATLAS Pixel detector modules.

Unfortunately for the setup in Bergen, there have been difficulties of getting a hand on 3D-sensors that are not already damaged or broken. This has obstructed an efficient progression at the lab, as there has been a lot of time spent waiting for a sensor. Then when a damaged sensor has been available for use, one can not be sure whether failures of tests are due to the sensor's fault's or faults in the test setup.

Not until February of this year, has a sensor that was not completely broken been presented for the setup, the SI-106 sensor. This was brought to Bergen from the University of Oslo after first getting a good introduction of the setup and procedures of tests and calibration of the sensor by Ole Røhne and Håvard Gjersdal. The sensor was tested and performed threshold tuning with at the test set up in Oslo (Figure 6.1) under the supervision of Ole Røhne. This chip was contaminated and thus needed cooling to suppress noise.

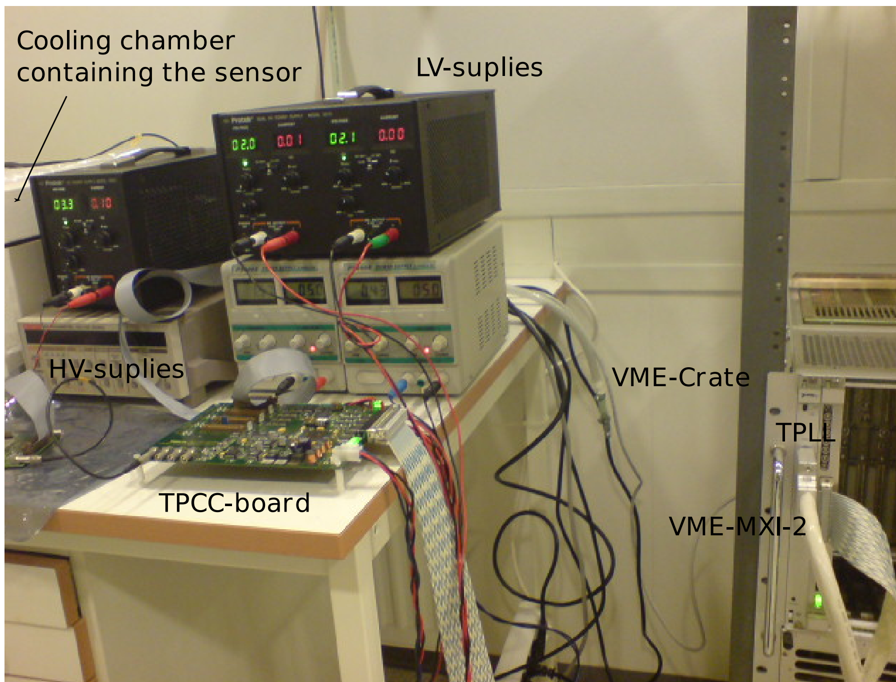

Figure 6.1: The setup at the laboratory in Oslo.

6.2 Setup and equipment

The majority of the test setup in Bergen was assembled by Cedric Virmontois and Dominik Fehlker in 2008. However, it was dismounted and some modules of the setup were used at CERN in the 2009 test beam. In 2010 the equipment had to be set up again with a few alterations, such as an additional low voltage supply for the FEI3 card and a environmental chamber for cooling. Figure 6.2 shows a simple schematic drawing of the setup in Bergen, and these components will be discussed further in this section. In figure 6.7 and 6.8 one can see pictures taken at the laboratory (lab containing environment chamber)of the setup and the sensor in the environment chamber.

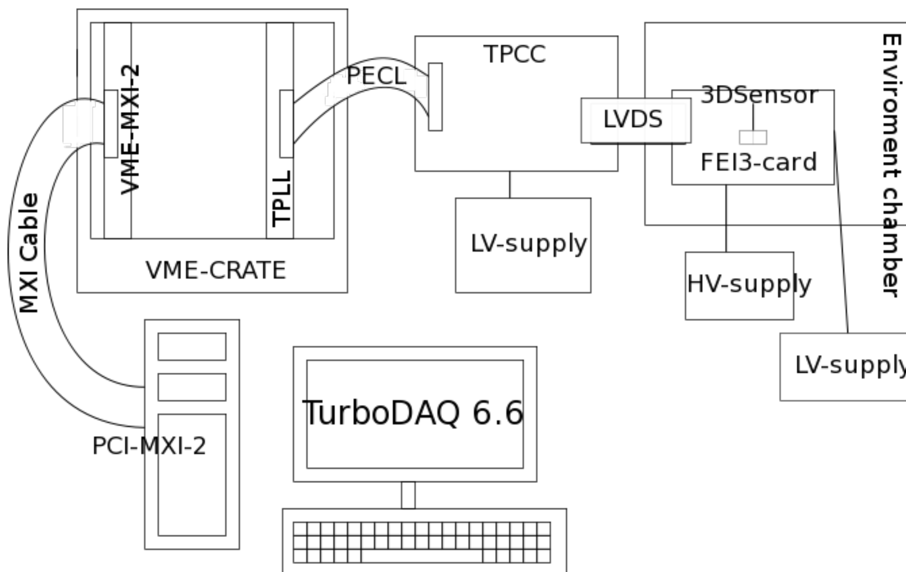

Figure 6.2: Schematic drawing of the setup at the lab in Bergen.

6.2.1 Front End electronic card (FEI3)

The 3D sensors have 18x160 (2880) pixels that are bump bonded to an electronic board (The FEI3 card discussed in section 2.5.2). This card makes readout of each individual pixel possible and also contains tunable components in order to select the best parameter for each pixel (Figure 6.3). The readout channels might have different threshold for readout and before the sensors can be used for particle detection it should therefore be calibrated in order to give all the pixels the same threshold and make the sensor surface as uniform as possible.

The FEI3 card has high voltage connection for depleting the sensor,

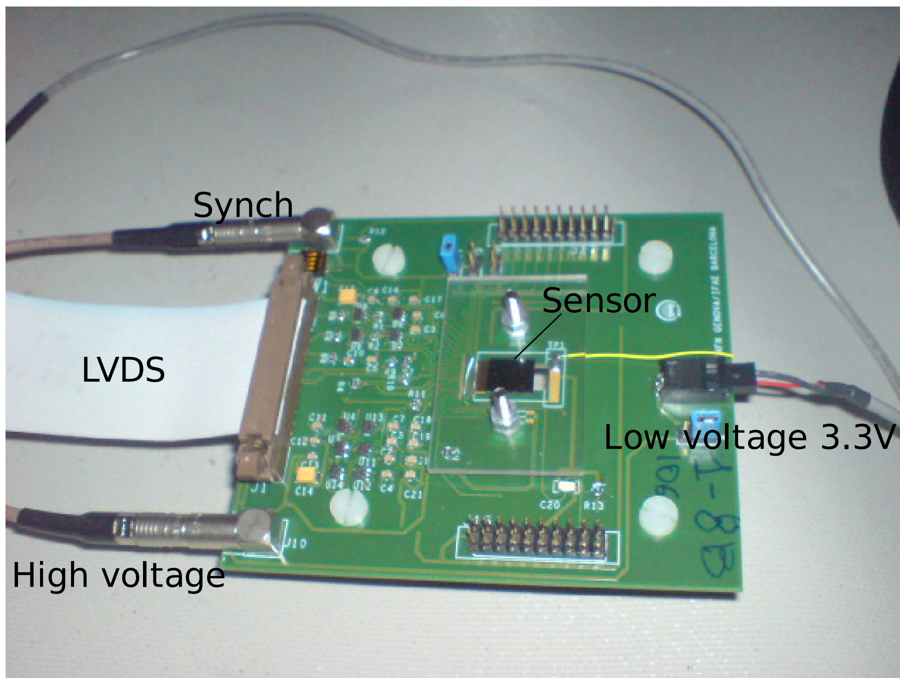

Figure 6.3: The Front End electronic card (FEI3: SI-106). The 3D sensor is the dark rectangular shape in the middle of the board.

an additional low voltage source of 3.3V is necessary to power the LVDS drivers.One lemo cable synchronizes the signals, and a flat cable transfers information between the FEI3-card and the Turbo pixel control card (TPCC board).

6.2.2 The TPCC board

The TPCC card (Figure 6.4) needs two digital and two analogue power supplies. These supply the board and a part of the Front End electronic card via two shielding cables with Molex connectors (Figure 6.5) .

6.2.3 The Turbo pixel low level card (TPLL board) and the VME system

The TPCC board is connected to the TPLL via a multicolor flat cable which transfers the data to the Turbo pixel low level card (TPLL board), a VME card used for clock generation and synchronization. This is plugged into the Versa Modular Eurocard(VME) crate and power is supplied through this. The TPLL converts the data to be transmitted on the VMEbus. This board

Figure 6.4: The TPCC board

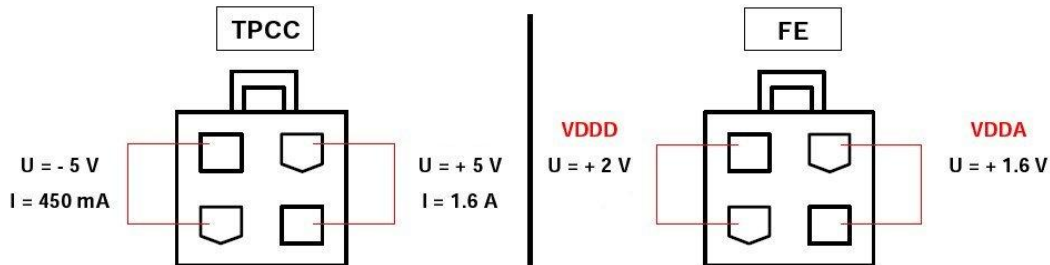

Figure 6.5: Pin-out of the Molex power connector, showing how the voltage is applied. [16]. These supply the TPCC board and FEI3 with low voltage.

is a single width, 6U, using 32 bit transfers.

The VME crate contains another board, The VME-MXI-2 controller board , from National Instruments to control the VMEbus. The computer and VME is connected through a MXI-2 cable plugged in the PCI card and in the VME-MXI-2 controller board (Figure 6.6).

The PCI-MXI-2 is a half-size, PCI-compatible plug-in circuit board that is plugged into the PCI-slot of the computer's motherboard. It is the interface between the computer and the VME [40]. Drivers are installed to communicate with the VMEbus via the MXI interface, . The NI- VXI/VISA drivers include a Resource Manager; an interactive configuration and troubleshooting program and libraries of software routines for MAX programming.

TurboDAQ

The computer IFTSUB041088 is a HP installed with Windows XP. TurboDAQ is essential to this setup. It is the software developed and used for electrical testing of ATLAS Pixel Detector Modules while under production [41]. It is only meant for readout of one module at the time and not used for the whole Pixel detector. TurboDAQ is based on National Instrument's LabWindows development suite. It communicates with the Pixel Modules through a combination of custom electronics (”TPCC”, ”TPLL”) and a generic PC-to-VME interface.

6.2.4 The environment chamber

Because the sensor was contaminated, it needed cooling to suppress noise and leakage currents. This was done in the environment chamber BS125-40 from Design Environmental limited. In this chamber one can regulate the temperatures between -40 °C and +130 °C. To avoid condensation during the cool down, the chamber was flushed with nitrogen before staring the

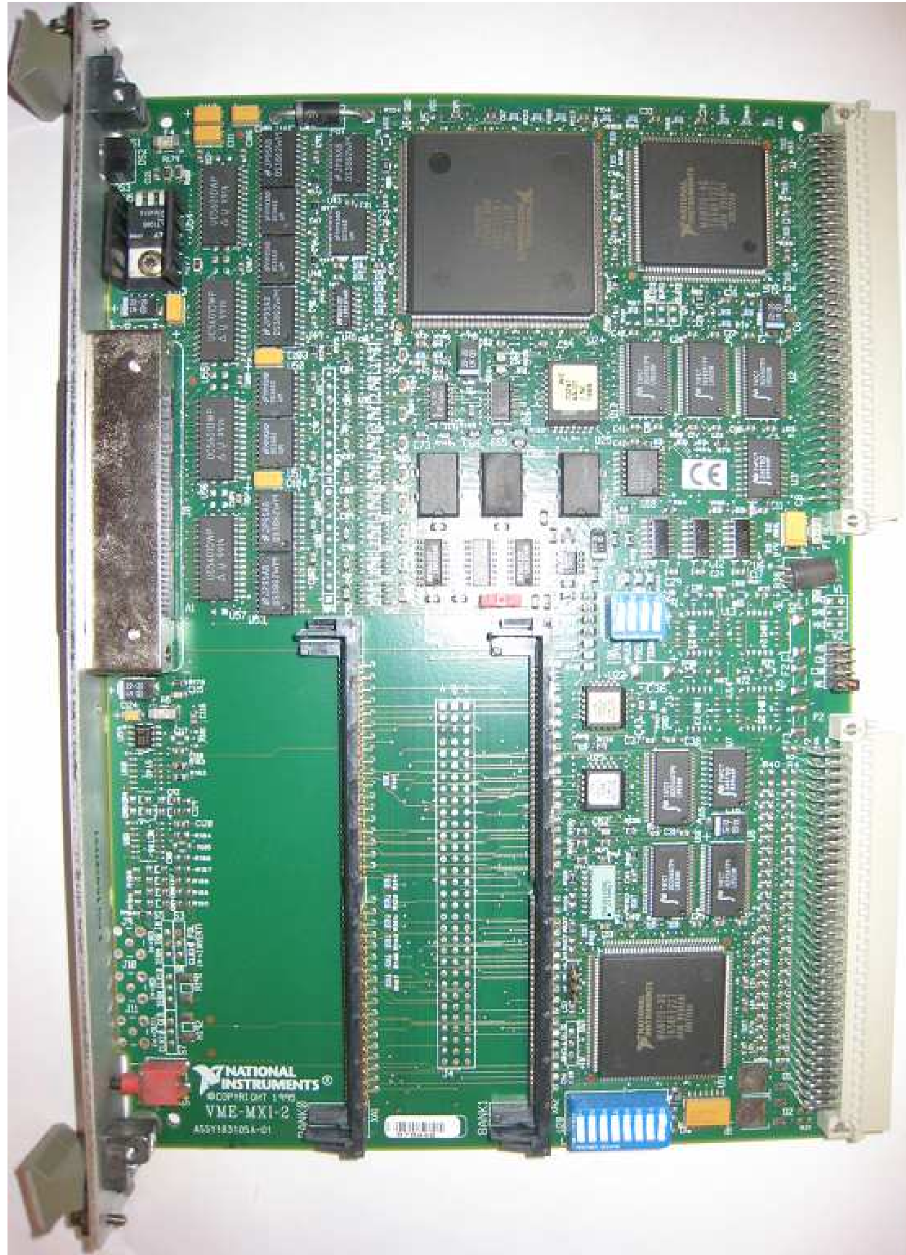

Figure 6.6: The VME-MXI-2 controller board [16]

cool down process.

In figures 6.7 and 6.8 one can see pictures taken at the laboratory (lab containing environment chamber) of the setup and the sensor in the environment chamber.

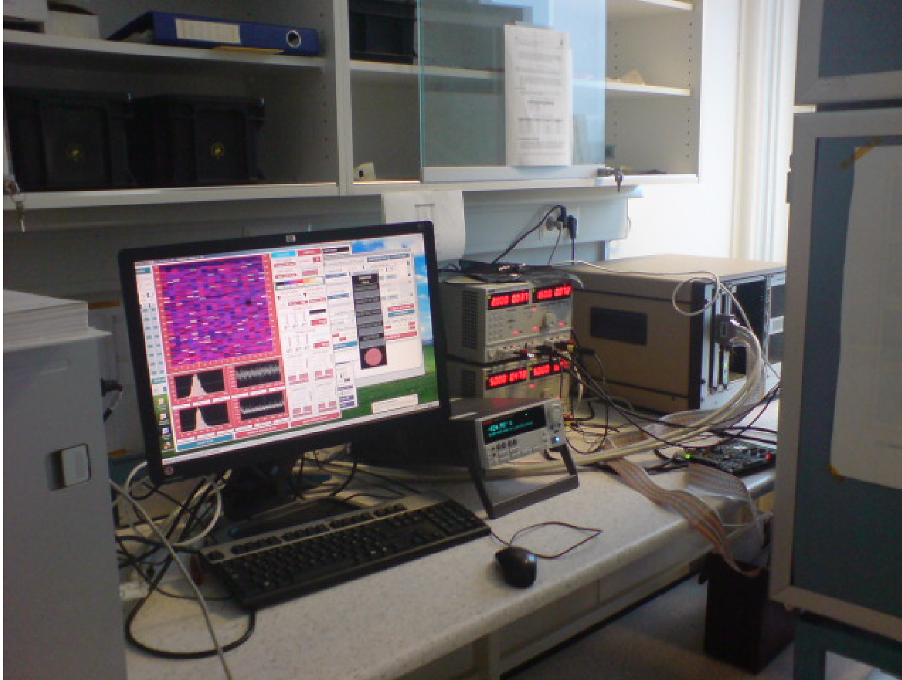

Figure 6.7: Picture of the setup at the lab in Bergen

6.3 Measurements and scans of the Si-106 sensor

Using TurboDAQ, one can perform various scans and calibrations depending on the setup and equipment.

Threshold scan

In the threshold scan, the threshold is read out for each pixel and plotted as a hit map as shown in the on-line plots in figure 6.9.

To see how the threshold varied, the threshold scan was performed at 5° C and -10° C in steps of 5V reverse bias. The scans were performed without any changes made to the fdac and IF values in the configuration

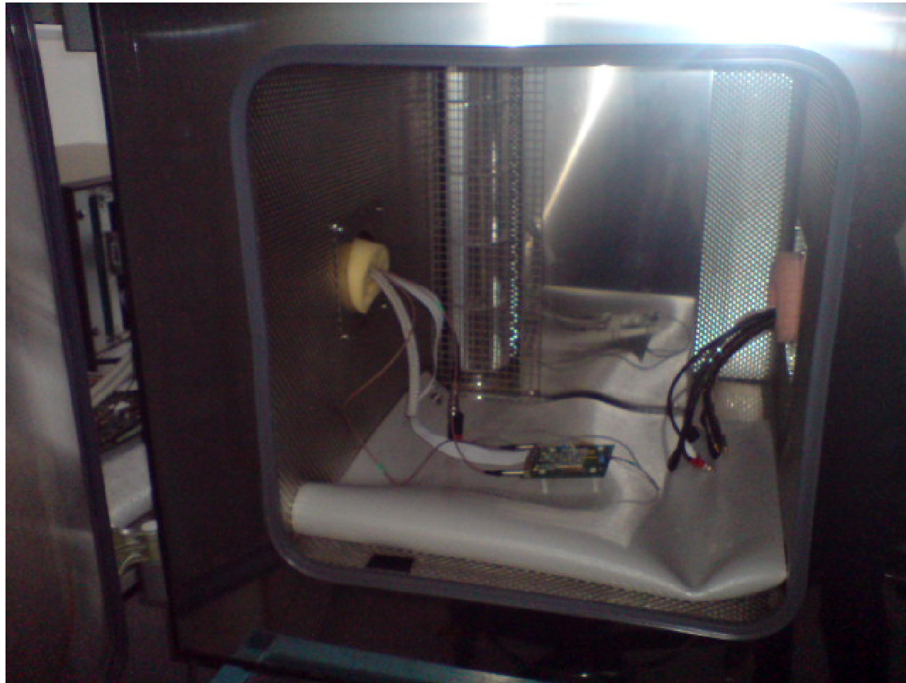

Figure 6.8: The FEI3 in the environmental chamber

panel: Only pre-set values of TurboDAQ were used.

Figure 6.10 shows the threshold map at 0 V, 5 V and 50 V. The color scale varies slightly, but is not significantly different for each of these plots. At 0 V, the sensor is totally un-depleted and has high thresholds for readout. The sensor is partly depleted at 5V, the threshold is lower and one can see the contours of the area with leakage current as a black dot in the right side area of the sensor. At 50 V the sensor is fully depleted, and the area of the leakage current is more evident.

A selection of the threshold distributions for 1 V, 5 V and 40 V at -10° C is shown in figure 6.11. TurboDAQ do a Gaussian fitting of these distributions, and one can read out the median and the standard deviation. This median was registered and plotted as a function of reverse bias voltage at 5° C and -10° C.

Figure 6.12 shows the median threshold of the sensor as a function of reverse bias voltage. The upper graph represents threshold scans performed at 5° C and the lower graph; scans performed -10° C. One can see that the difference of the thresholds between these two temperatures are approx-

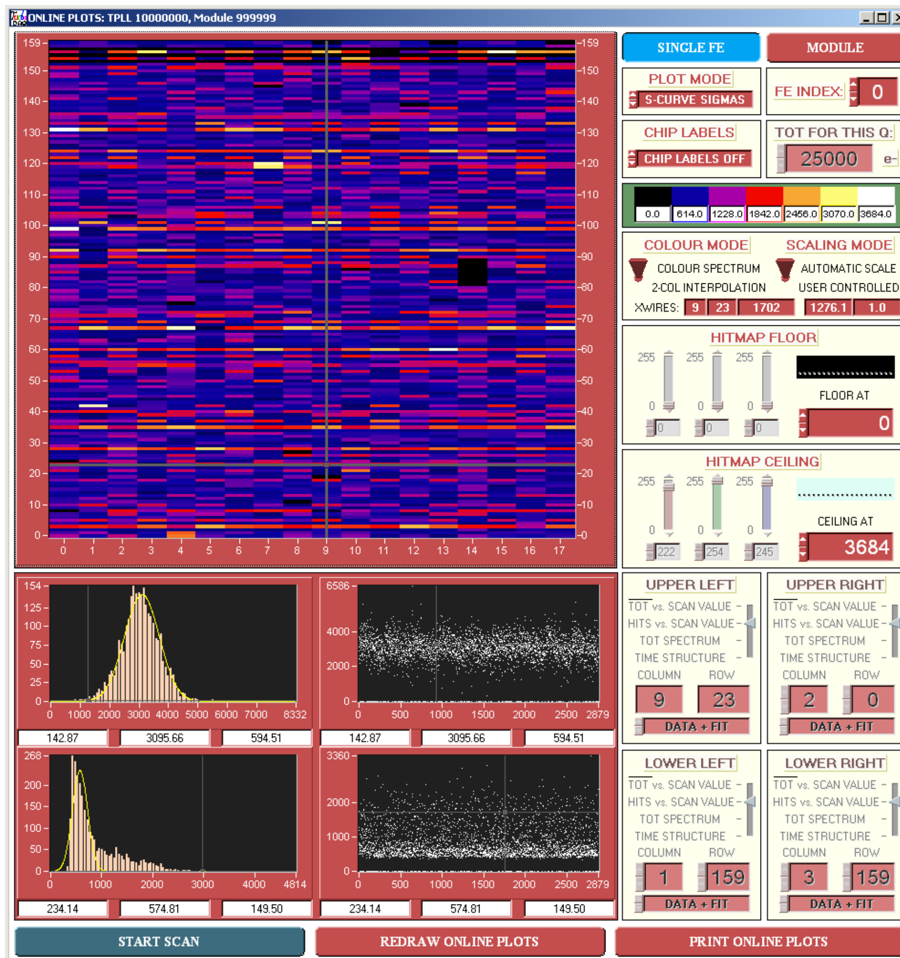

Figure 6.9:

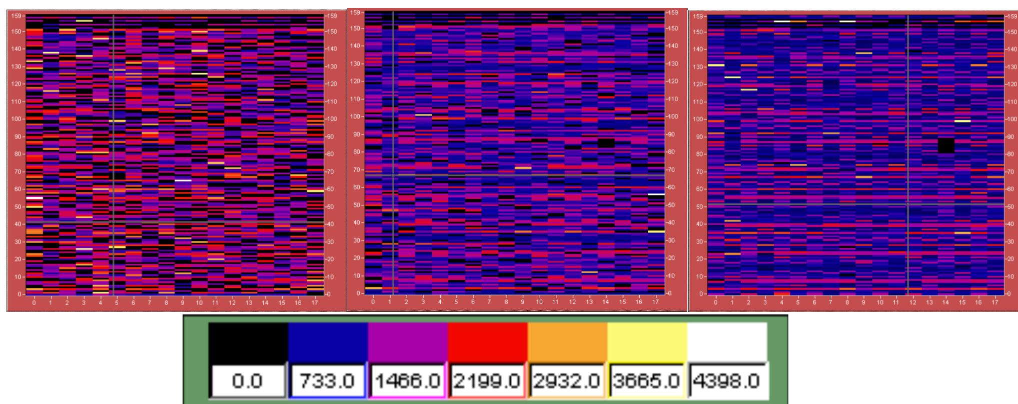

Figure 6.10: The threshold maps for (from the left) 0 V, 5 V and 50 V at -10° C. The color scale example is taken from the 50 V map.

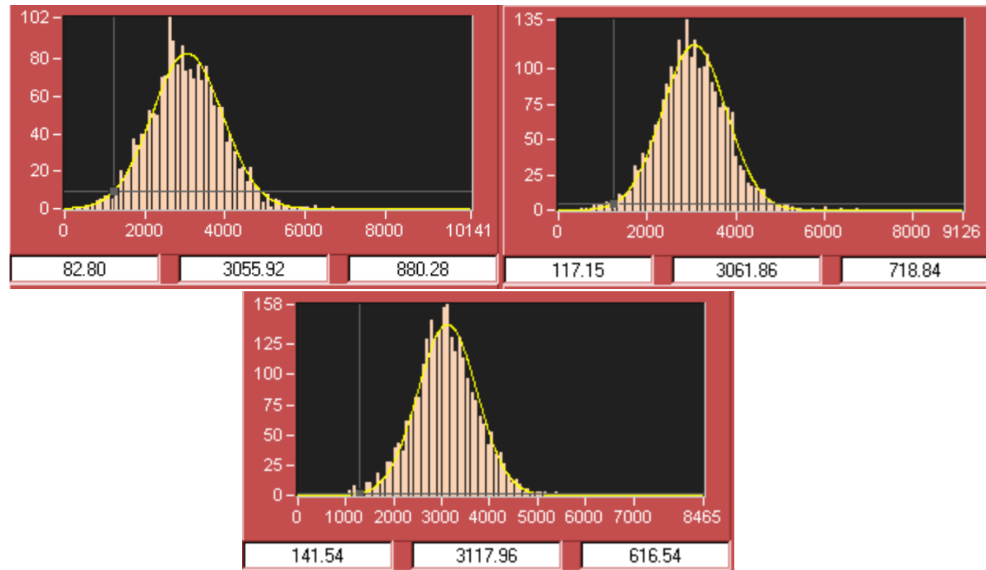

Figure 6.11: The threshold distributions for 1 V, 5 V and 40 V at -10° C. Below the distributions one can read out the mean value and standard deviation of the Gaussian fitting of the plot.

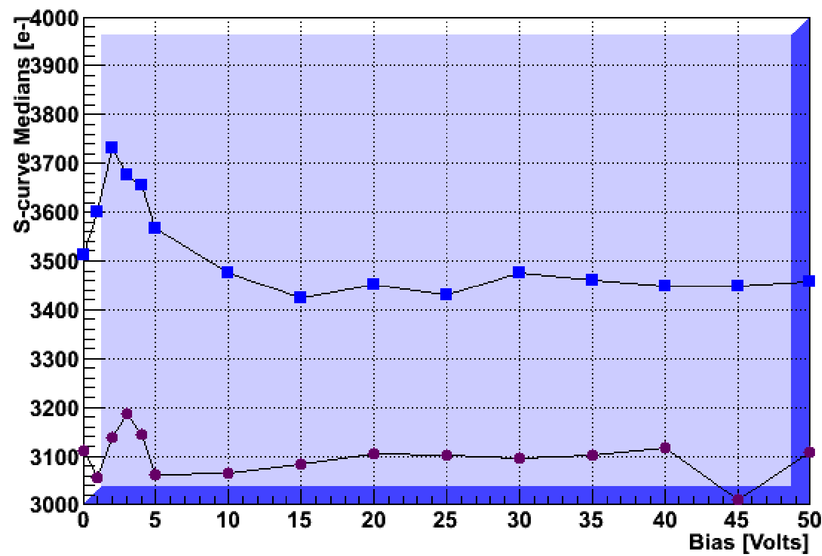

Figure 6.12: Median values of the threshold distributions as a function of reverse bias voltage. The blue square markers represent the scans at 5° C and the purple circular markers represents the scans made at -10° C.

imately the same for all the voltages. Both temperatures follow the same pattern with a peak threshold around 2-3 V, and a stable threshold after 10 V.

Noise scan

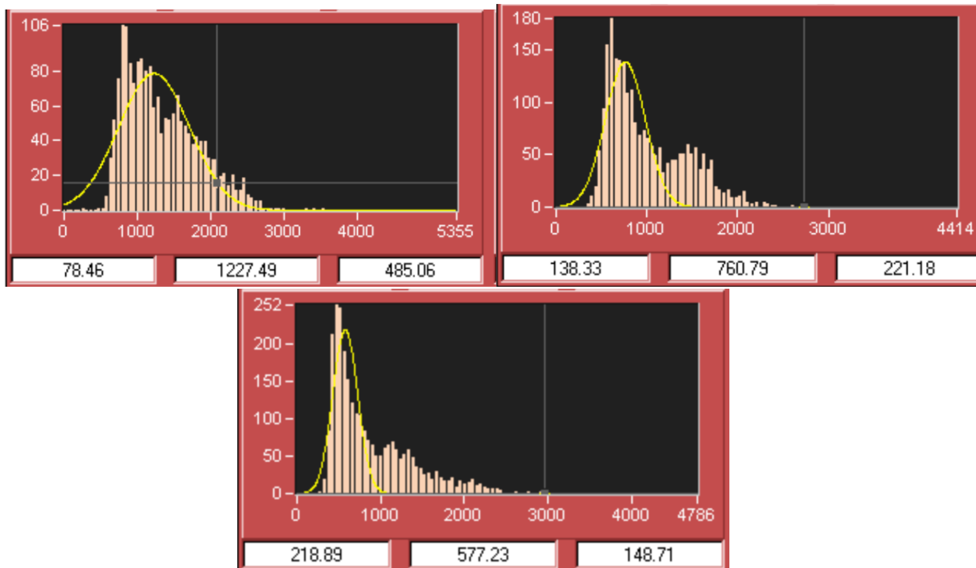

Figure 6.13: The noise distributions for 1 V, 5 V and 40 V at -10° C, with Gaussian fitting.

The on-line plots after a threshold scan also give the noise distributions fitted with a Gaussian distribution. Figure 6.13 shows how this distribution varies for 1 V, 5 V and 40 V at -10° C. One can see that the Gaussian fit is not very good for this distribution. The peak of the distribution is always lower than the mean value of the fit.

The mean value for this distribution was registered and plotted as a function of the reverse bias voltage shown in figure 6.14. As expected, the noise is high at lower voltages, before it fattens out around the value of 600 electrons. This shows that the sensor is fully depleted after 10V.

Mon-leak scan

An area of leakage current could be identified early in the threshold maps as a rectangle with a 0 e^{-} threshold. A Mon-leak scan was performed to see how large the leakage current was. For a monleak scan the IF-parameter was set to 1 in the configuration panel in accordance with instructions on how to

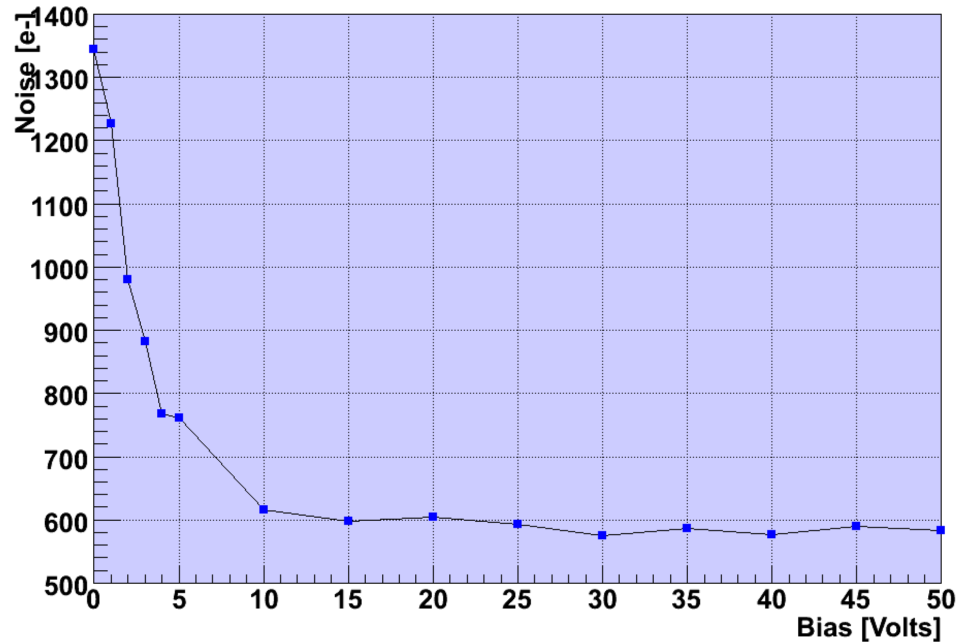

Figure 6.14: The mean noise as a function of reverse bias voltage.

perform scans in the notes: "Systematic Tests of 3D sensors for irradiation" by Per Hansson [42]. The resulting plot of the leakage current is shown in 6.15, where the leakage current from the white spot is so high that the color scale makes the other pixels appear almost black. By moving the cursor around the map, the respective pixel leakage current value can be read out. The value of the area with leakage current is 127 e^{-}. This value remains the same for all voltages and temperatures tested.

Threshold tuning

One of the main purposes of the TurboDAQ setup is to calibrate the sensor's pixels. Threshold tuning is a procedure performed to get a uniform sensor surface with respect to threshold.

Threshold tuning is made in steps where one interchanges between the two TurboDAQ scans "'TDAC Tune Internal-Cal" that tunes the threshold for each pixel individually, and "FDAC Tune Internal-Cal" that tunes the feedback current for each individual pixel.

Before one can start the scan, it is necessary to save and upload the calibration constants that are unique for every 3D-sensor. The calibration

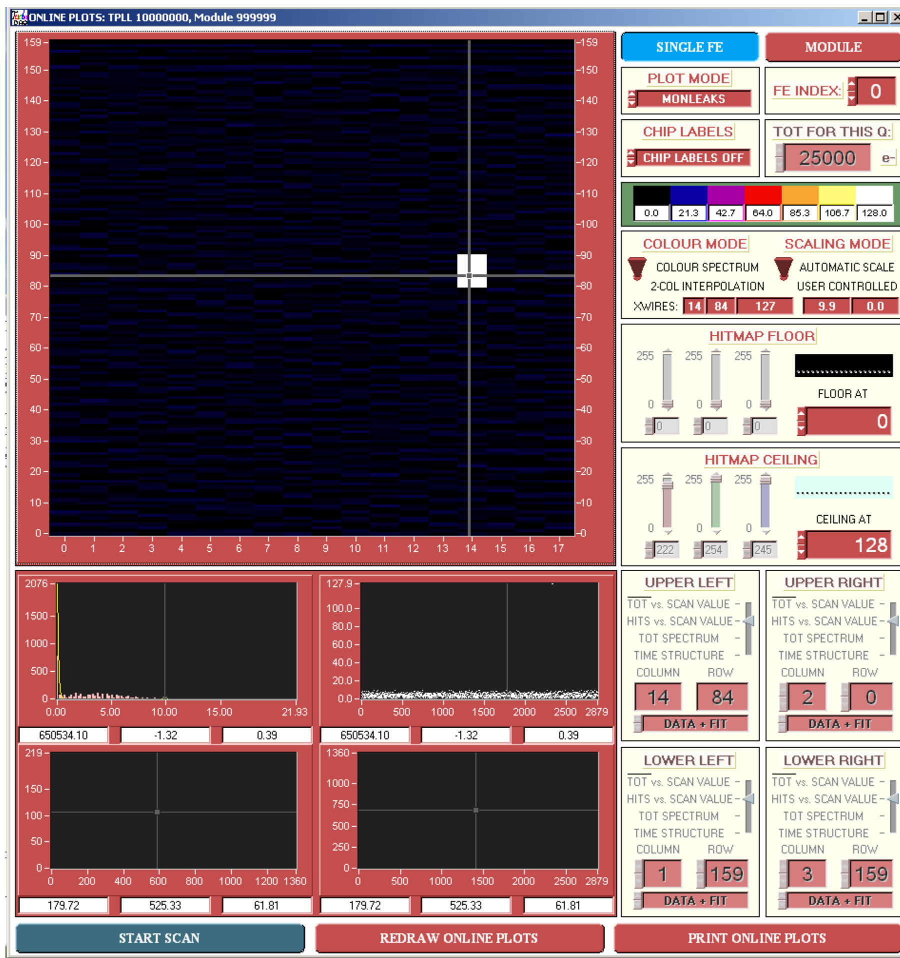

Figure 6.15: Mon-leak scan: The white square is the area with leakage current -same as in Oslo

constants for the SI-106 sensor was forwarded in mail by the group in Oslo. One must also adjust the configuration parameters gdac and IF, to obtain a target value rot the mean of the s-medians distribution as close to 4000 e^- and a ToT close to 60. Normally one would aim for a target value of 3200 e^-, but for noisy sensors this needs to be increased. When performing the threshold scan in Oslo at approximately 0 ° C, these target values were obtained by setting gdac to 22/23 and IF to 9. In Bergen, the target value of 4000 e^- was only obtained at temperatures above 0 ° C, and at -10 ° C, the highest mean of the s-medians distribution obtained was below 3200 e^-.

Before the threshold calibration, one does a threshold scan to check if all the parameters are correct, and to document the improvement of the calibration. After the tdac calibration is finished, one needs to save the data from the scan and read it out for the tdac value in the configuration panel. One then does a new threshold scan to see improvements from the calibration. The improvements were checked by looking at the standard deviation of the s-medians distribution from the threshold scan. A decrease in this value meant that the threshold of the surface was more uniform than previously. After this, one follows the same procedure for the fdac calibration in stead of tdac. These steps are repeated until there is no further decrease in the value of the standard deviation.

When the threshold tuning was performed in Oslo, the standard deviation improved from approximately 600 to approximately 200 within two repetitions of this procedure at 0 ° C at a reverse bias voltage of 25V.

In Bergen, the threshold tuning of the SI-106 sensor has not been performed successfully. It has been attempted at several different temperatures ranging from -10 ° C to 20 ° C for voltages between 20 and 60 V. TurboDAQ always crashed after the first tdac tuning. This was most likely due to many bad fits. Shorter scans were performed to investigate exactly when TurboDAQ crashes. It was found to crash between 99 and 89 in a scan ranging from 119 to 9 in twelve steps.

Figure 6.16 shows a screen-shot of the tdac tuning at an outer scan value of 79. One can see that the distributions are far from a Gaussian, and it is all these bad fits that makes TurboDAQ crash. Figure 6.17 shows how the distributions become even more " unfit-able"(at the left), before it has crashed (to the right).

Bias scan: The IV-curve

An IV curve of the sensor was plotted at -10° in figure 6.18, to attempt to determine what could be causing the break-down of TurboDAQ.

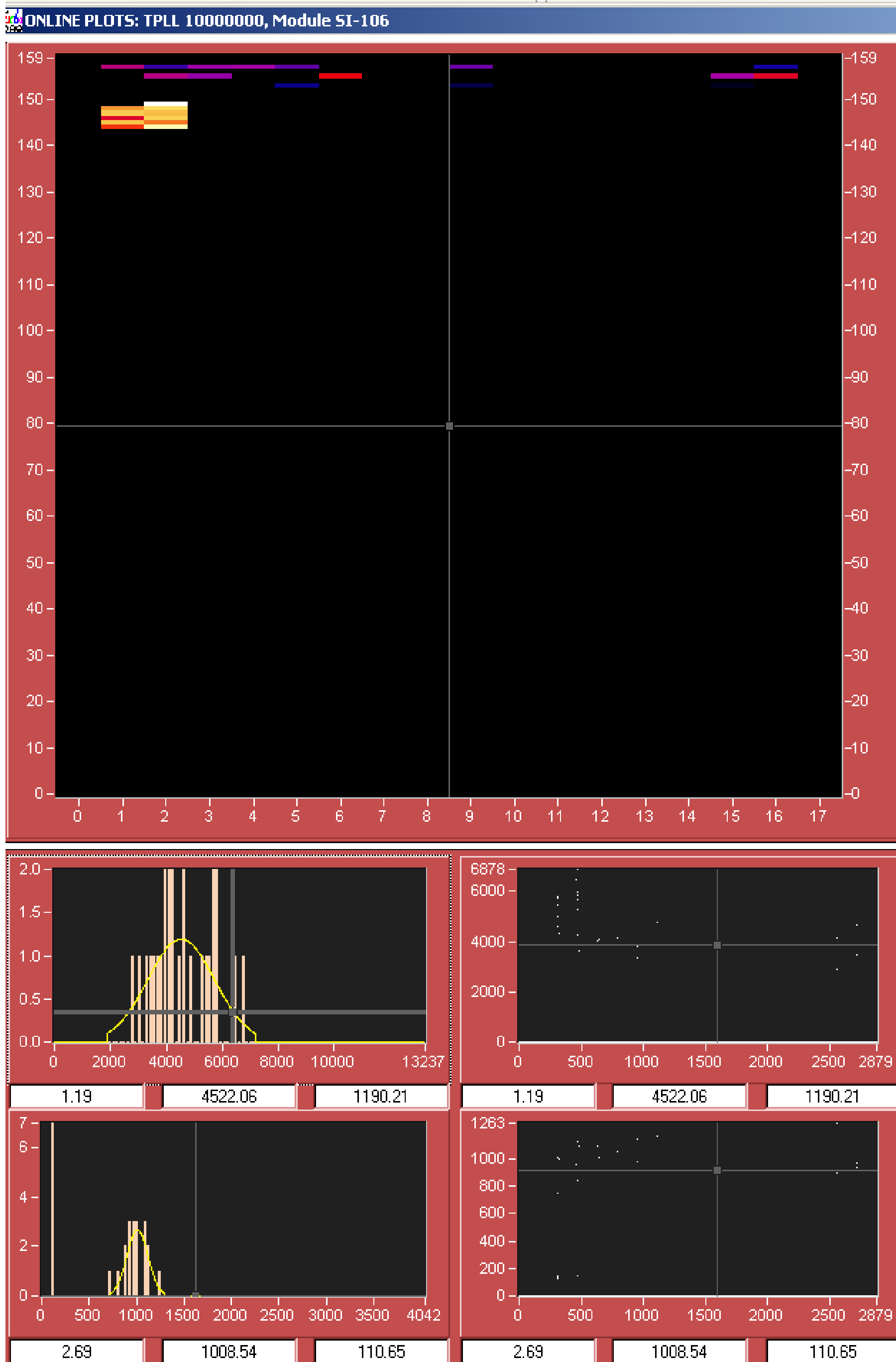

Figure 6.16: The beginning of the tdac calibration shows that very early in the scan, there are some really big deviations from a normal distribution.

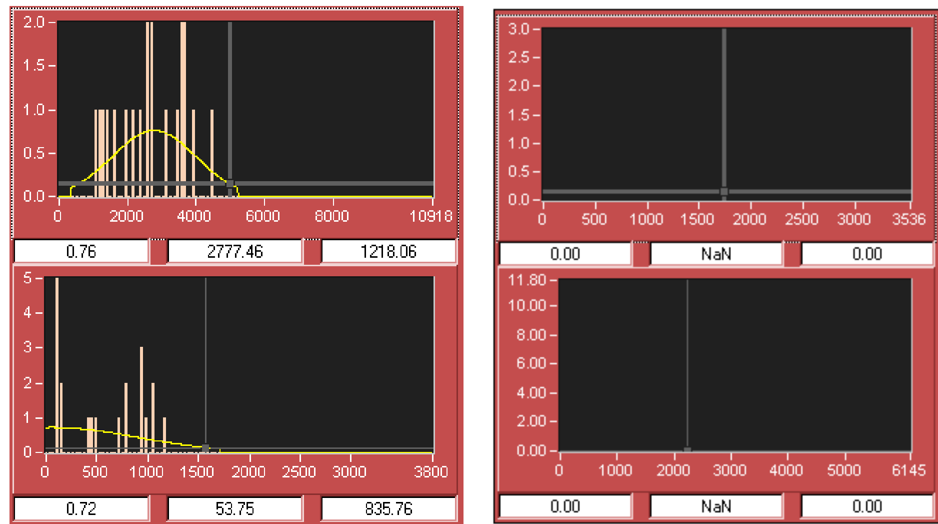

Figure 6.17: The tdac calibration fits approximately 2/3 out in the scan, and after the scan is finished.It is impossible for TurboDAQ to make a good fitting of the distribution.

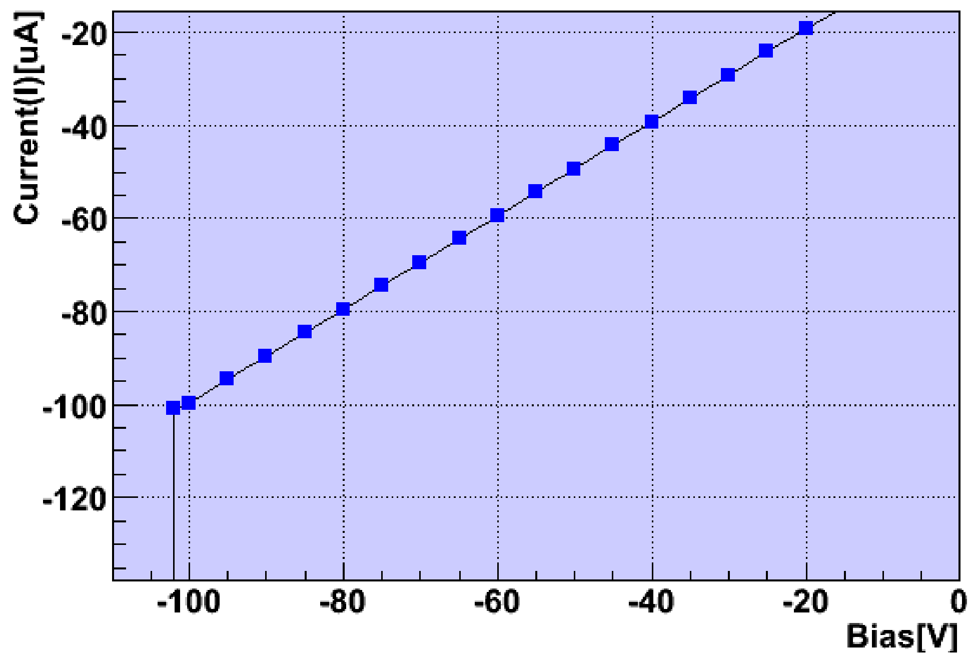

Figure 6.18: The IV curve of the SI-106 sensor

As one can see from the plot, the current in the detector is linear until break down voltage at 102 Volts. The constant slope implied that the sensor was of ohmic character. An ohmic material is a material where current is proportional to voltage to a limited area of variation in voltage, and will therefore give a linear IV-curve. A non-ohmic material's has different current voltage characteristics and for diodes one expects a plateau of constant current, and the IV-curve will therefore not be linear [43]. Consultations with the 3D group in Oslo, confirmed that the sensor had ohmic characteristics and thus, that the IV-curve should not be a surprise. The current might have other sources than going through the material of the 3D sensor.

The exact reason for the TurboDAQ crashes is still unknown, and needs to be investigated further. The sensor should be brought back to Oslo or to another test setup to check if the sensor gives the same output, or if it can be performed threshold tuning at. If this works in Oslo, then there is probably something wrong with the software in Bergen and some changes will need to be made. The Oslo group had made some changes to the TurboDAQ program themselves, so although Bergen has the newest TurboDAQ version, it can be necessary to do as in Oslo. Ole Røhne has inspected the setup and could not find any obvious faults with it. If the sensor makes TurboDAQ behave the same way in Oslo as in Bergen, one can conclude that the sensor must have become further contaminated during transport and storage. In that case one would need to test a sensor that is not so damaged to be able to say whether the setup in Bergen is working as it should.

6.4 Summary of the laboratory tests

The equipment was successfully set up at the lab at the University of Bergen and the sensor SI-106 was brought from Oslo. This sensor was contaminated, which made it necessary to cool it down to suppress noise. There was however an area of leakage current present at all time.

Several tests and scans were performed of the SI-106 sensor. A threshold scan and a noise scan was performed as function of bias voltage. These scan showed that the sensor was fully depleted at 10V.

An area of great leakage current was observed in the sensor. The IV-curve showed that the sensor had an ohmic character, which turned out to be as expected according to the team in Oslo.

The attempts of performing a threshold tuning to the sensor, all failed. The software TurboDAQ would crash when the number of bad fits became to large for it to handle. Because this threshold tuning had been previously

performed successfully in Oslo, there are still uncertainties of whether the fails in Bergen is due to further contamination and damage during transport and storage, or if the TurboDAQ version need some updates or adjustments.

The SI-106 sensor should be brought to Oslo or CERN to test if the threshold tuning can be performed on this sensor there. If so, further adjustment must be done to the setup in Bergen. Making the setup work in Bergen has been difficult as all the expertise is at CERN or elsewhere. One should go to the lab in CERN and take part in the work that is done there with the 3D sensor. This will give a unique opportunity to gain the necessary expertise and network needed in Bergen. After this the lab in Bergen will be ready to receive 3D sensors for calibration and to do measuring to radioactive sources. One can then start the construction of a test bench with object to investigate the prospects within areas of medical imaging such as positron emission tomography (PET) for monitoring radiation therapy and X-ray mammography.

Chapter 7

Conclusion and outlook

A study of 3D silicon sensors has been performed. Analyses were done from test beam data taken at CERN in 2008, and a test and calibration system for 3D sensors was set up in Bergen and taken into use.

Data from test beam 2008 were analysed for a 3D sensor with two differnt electrode configurations ; the 3E-G sensor with three electrodes in each pixel and a 3D sensor with four electrodes in each pixel; the 4E-C sensor. The runs for this analysis had voltages ranging from 10 V to 40 V for the 3E-G sensor and 10 V to 30 V for the 4E-C sensor.

An alignment study of the data was performed at an early stage of the analysis. This showed an improvement from earlier versions of the data [1]. A small negative drift was observed as a function of run number, however, the alignment can be claimed to be good as it is better than 3 μm.

The Time over Threshold (ToT) was studied as a function of bias voltage. The ToT distributions for the 3E-G sensor at bias voltage below 40V shows deviations from the expected Gauss-Landau distribution. This has not been observed for the 4E-C sensor. ToT values were observed to be stable between 10V and 40V (10V and 30V for 4E-C), and a bit lower for the 4E-C sensor than for the 3E-G sensor.

In the sensors area occupied by the electrodes, a significant efficiency loss was observed. Due to the small diameter of the electrodes, this did however not decrease the sensor efficiency significantly as was shown in the study of efficiency as a function of bias voltage. The efficiency was found to lie around 95 % for the 3E-G sensor at all the voltages between 10V and 40V.

[1] The alignment was previously studied by B. Stugu and A. Abdelsalam as a contribution to alignment of the data from the test beam. Realignment was performed by O. Røhne and H. Gjersdal

For the 4E-C sensor, the efficiency was a bit lower due to more electrodes with efficiency loss.

Both the study of ToT and efficiency as a function of bias voltage shows that the sensor is completely functional at 10V, which is a relatively low voltage. The "active edge" pixel was found to have full efficiency all the way to the outer edge as expected and with a resolution of 9.9$\pm$ 0.6 μm, compatible with the resolution of the tracker.The data from the 4E-C sensor showed some strange distributions of dx/dz and dy/dz in the reconstructed tracks, however, this did not seem to affect the efficiency.

The 3D community has developed a new framework for 3D test beam data analysis that is supposed to have better alignment. Due to the time schedule of this thesis, this has not been taken in use by us in Bergen. Before further test beam analysis, the new framework must be learned to bring us up to level with more experiment groups at the area.

The equipment was successfully set up at the lab at the University of Bergen and the sensor SI-106 was brought from Oslo. This sensor was contaminated, which made it necessary to cool it down to suppress noise. There was however an area of leakage current present at all time. Several tests and scans were performed of the SI-106 sensor. A threshold scan and a noise scan was performed as function of bias voltage. These scan showed that the sensor was fully depleted at 10V. An area of large leakage current was observed in the sensor. The IV-curve showed that the sensor had an ohmic character, which turned out to be as expected according to the team in Oslo.

The attempts of performing a threshold tuning to the sensor, all failed. The software TurboDAQ would crash when the number of bad fits became to large for it to handle. Because this threshold tuning had been previously performed successfully in Oslo, there are still uncertainties of whether the fails in Bergen is due to further contamination and damage during transport and storage, or if the TurboDAQ version need some updates or adjustments.

The SI-106 sensor should be brought to Oslo or CERN to test if the threshold tuning can be performed on this sensor there. If so, further adjustment must be done to the setup in Bergen. Making the setup work in Bergen has been difficult as all the expertise is at CERN or elsewhere. One should go to the lab in CERN and take part in the work that is done there with the 3D sensor. This will give a unique opportunity to gain the necessary expertise and network needed in Bergen. After this the lab in Bergen will be ready to receive 3D sensors for calibration and to do measuring to radioactive sources. One can then start the construction of a test bench with object to investigate the prospects within areas of medical imaging such as

positron emission tomography (PET) for monitoring radiation therapy and X-ray mammography.

Currently all the three technologies; planar silicon-, 3D silicon- and CVD diamonds detectors are considered for the IBL and are being actively prototyped. There are plans to build and test full IBL modules with each of those sensor technologies and a decision for the final sensor is expected to be made based on these test results. The assumption is that this will be around summer 2011, but this depends on how the FEI4 chip, a new front-end chip under development, works [44–46].

Bibliography

[1] F. Hartmann. *Evolution of silicon sensor technology in particle physics.* Springer Verlag, 2009.

[2] C. Amsler et al. (Particle Data Group), Physics Letters B667, 1 (2008) and 2009 partial update for the 2010 edition.

[3] W. R. Leo. The Gaussian or Normal Distribution. `http://nedwww.ipac.caltech.edu/level5/Leo/Stats2_3.html`.

[4] K. Kleinknecht. *Detectors for particle radiation.* Cambridge University Press, 1998.

[5] W.R. Leo. *Techniques for Nuclear and Particle Physics Experiments.* Springer Verlag, 1994.

[6] J. D. Cutnell & K. W.Johnson. *PHYSICS.* John Wiley & Sons, Inc, 2007.

[7] W.Storr. Electronics-Tutorials.ws. `http://www.electronics-tutorials.ws/diode/diode_7.html`, 2010.

[8] P. A. Tipler and R. A. Llewellyn. *Modern Physics, 4th edition.* W. H. Freeman and Company, 2003.

[9] CMS Outreach. CMS, The Compact Muon Solenoid Experiment: Pixels. `http://cms.web.cern.ch/cms/Detector/Tracker/Pixels.html`.

[10] C. J. Kenney S. I. Parker and J. Segal. 3D – A proposed new architecture for solid-state radiation detectors. *Nuclear Instruments and Methods in Physics Research Section A: Accelerators, Spectrometers, Detectors and Associated Equipment*, 395(3):328 – 343, 1997. Proceedings of the Third International Workshop on Semiconductor Pixel Detectors for Particles and X-rays.

[11] E. Bolle et. al. 3d pixel - recent results. *Proceeding of Science*, 2009.

[12] H. Gjersdal et al. Tracking Efficiency and Charge Sharing of Full 3D Silicon Sensors at Different Angels in a 1.4 Tesla Magnetic Field. *Nucl. Instrum. Meth. A*, 2009.

[13] C. Da Vi et al. 3d active edge silicon sensors with different electrode configurations: Radiation hardness and noise performance. *Nuclear Instruments and Methods in Physics Research Section A: Accelerators, Spectrometers, Detectors and Associated Equipment*, 604(3):505 – 511, 2009.

[14] C. J. Kenney et al. Silicon detectors with 3-D electrode arrays: fabrication and initial test results. *Nuclear Science, IEEE Transactions on*, 46(4):1224–1236, 1999.

[15] M. Mathes et al. Test Beam Characterizations of 3D Silicon Pixel Detectors. *arXiv*, June 2008.

[16] Cedric Virmontois. 3D detectors. Technical report, University of Bergen, 2008. Cedric Bergen final repport.

[17] O. Røhne. Edge Characterization of 3D Silicon Sensors after Bump-Bonding with the ATLAS Pixel Readout Chip. *IEEE*, 2008.

[18] Ivan Peric et al. The FEI3 readout chip for the ATLAS pixel detector. *Nuclear Instruments and Methods in Physics Research Section A: Accelerators, Spectrometers, Detectors and Associated Equipment*, 565(1):178 – 187, 2006. Proceedings of the International Workshop on Semiconductor Pixel Detectors for Particles and Imaging - PIXEL 2005.

[19] LHC outreach. LHC MACHINE OUTREACH. `http://lhc-machine-outreach.web.cern.ch/lhc-machine-outreach/`.

[20] Gordon Fraser et al. The History of Antimatter. `http://livefromcern.web.cern.ch/livefromcern/antimatter/history/AM-history02-b.html`.

[21] LHC Colaboration. LHC Design Report Volume I,The LHC Main Ring, Chapter3. `http://lhc.web.cern.ch/LHC/LHC-DesignReport.html`.

[22] LHC Outreach. Beam. `http://lhc-machine-outreach.web.cern.ch/lhc-machine-outreach/beam.htm`.

[23] LHC Outreach. Collisions. `http://lhc-machine-outreach.web.cern.ch/lhc-machine-outreach/collisions.htm`.

[24] E. M. Henley & A. Garcia. *SUBATOMIC PHYSICS 3rd edition*. World Scientific Publishing Co.Pte.Ltd., 2007.

[25] LHC Colaboration. The LHC experiments . `http://public.web.cern.ch/public/en/LHC/LHCExperiments-en.html`.

[26] ATLAS collaboration. What is ATLAS. `http://atlas.ch/what_is_atlas.html#2a`.

[27] D. Ward and C. Lester. Part II Particle and Nuclear Physics . http://www.hep.phy.cam.ac.uk/~drw1/particleandnuclear/welcome.html.

[28] ATLAS collaboration. Detector description. http://atlas.ch/detector.html.

[29] ATLAS Collaboration. ATLAS DETECTOR AND PHYSICS PERFORMANCE. Technical report, CERN/LHC, 1999.

[30] The HYPATIA team . Basics for simplified HYPATIA. http://hypatia.scl.rs/index.php/simplified-basics.

[31] Su Dong. ATLAS Upgrade Information. http://www.slac.stanford.edu/exp/atlas/upgrade/.

[32] Project Office. The ATLAS experiment, High luminosity upgrade. http://atlas.web.cern.ch/Atlas/GROUPS/UPGRADES/.

[33] P.Grenier C. Da Vi and O.Røhne. Proposal for Test Beam Runs at CERN SPS in October (10-20)-November (20-25) 2009, Experiment: ATLAS 3D Silicon pixels , September 2009.

[34] H. Gjersdal and O. Røhne. Test beam reconstruction and analysis. https://silicondetector.org/display/Atlas/Test+Beam+Activities?showChildren=true, September 2008. TestBeam 2008 analysis presentation Håvard.

[35] CERN collaboration. SPS the Super Proton Synchrotron. http://public.web.cern.ch/public/en/Research/SPS-en.html.

[36] J.F. Arguin on behalf of the ATLAS Pixel Collaboration. Commissioning of the ATLAS Pixel Detector. In *34th International Conference on High Energy Physics, Philadelphia*, 2008.

[37] J. R. Taylor. *An introduction to Error Analysis, The study of uncertainties in physical measurements, Second edition.* University Science Books, 1997.

[38] R. V. Hogg & E. A. Tanis. *Probability and Statistical Inference, 7e.* Pearson Education , Inc., 2006.

[39] C. Da Via. Radiation hard silicon detectors lead the way. *CERN Courier*, Jan 1, 2003.

[40] National Instruments. Getting Started with Your PCI-MXI-2 and the NI-VXI/NI-VISA Software for Linux. http://digital.ni.com/manuals.nsf/websearch/5136F47F1F62CA8386257096004D2109.

[41] J.Grosse-Knetter. Turbodaq. http://physik2.uni-goettingen.de/~jgrosse/TurboDAQ/.

[42] P. Hansson. Systematic Tests of 3D sensors for irradiation, 07 2009. Notes from Per Hansson.

[43] E. Lillestøl, O. Hunderi and J. R. Lien. *Generell fysikk for universiteter og høgskoler, Bind 2 Varmelre og elektromagnetisme.* Universitetsforlaget AS, 2001.

[44] G. Darbo et al. IBL general meeting. http://indico.cern.ch/conferenceDisplay.py?confId=73688, February 2010.

[45] H. Pernegger. Insertable B-layer. Correspondance by mail.

[46] M Marcisovsky. ATLAS Insertable B-Layer. *cdsweb.cern.ch/record/1207594/files/ATL-INDET-PROC-2009-012.pdf*, 2009. Preprint submitted to Elsevier.